University of Ferrara

Department of Physics and Earth Sciences

BERGISCHE
UNIVERSITÄT
WUPPERTAL

University of Wuppertal

Faculty of Mathematics and Natural Sciences

Lattice Boltzmann Methods for Fluid-Dynamics in Relativistic Regimes

European Joint Doctorate Program High Performance Computing in Life Sciences Engineering and Physics (HPC-LEAP)

Advisor

Prof. Raffaele Tripiccione

Student

Alessandro Gabbana

Advisor

Prof. Matthias Ehrhardt

2015-2018 – XXXI course
Coord. Prof. Vincenzo Guidi

The PhD thesis can be quoted as follows:

urn:nbn:de:hbz:468-20200729-103821-9
[http://nbn-resolving.de/urn/resolver.pl?urn=urn%3Anbn%3Ade%3Ahbz%3A468-20200729-103821-9]

DOI: 10.25926/w5v9-qf57
[https://doi.org/10.25926/w5v9-qf57]

Summary

In this thesis work we present the algorithmic derivation of a new class of Lattice Boltzmann Methods appropriate for the study of dissipative relativistic fluids. While previous models were restricted to the use of massless particles, implying ultra-relativistic equations of state, this work provides a significant step towards the formulation of a unified relativistic lattice kinetic scheme, covering ideal gases of both massive and near-massless particles, seamlessly bridging the gap between relativistic and low-speed non-relativistic fluid regimes.

In a first important application of this novel numerical tool, we present results bringing new insight in the long standing problem of understanding the pathway from relativistic kinetic theory to relativistic hydrodynamics. We conduct an accurate analysis of the relativistic transport coefficients in the relaxation time approximation, providing numerical evidence that the Chapman Enskog expansion correctly relates kinetic transport coefficients and macroscopic hydrodynamics parameters in dissipative relativistic fluid dynamics, confirming recent theoretical results.

This analysis, in turn, can be seen as an accurate calibration of this class of numerical solvers, making them suitable to deliver improved physical accuracy in the simulation of realistic systems. To give an example, we present results of simulations solving the Riemann problem for a quark-gluon plasma, showing good agreement with previous results obtained using other solvers present in the literature.

As a further application we study the transport properties of electrons in ultra-clean graphene samples, for which a hydrodynamic description is appropriate due to the predominance of electron-electron scattering over electron-phonon interactions. Using appropriate 2D formulations, enriched

to describe the effects of the external electrostatic drive, and to capture the interactions with phonons and impurities, we present simulations of laminar flows taking into consideration geometrical setups used in actual experiments. Furthermore, we also consider electronic systems where nonlinear effects start becoming relevant. Basing on extensive numerical simulations, we identify transport parameters which could be used to trigger and observe preturbulent signals in a hydrodynamic region as close as possible to those within reach of current experimental conditions.

As a closing note, we remark that the numerical methods described in this thesis work retains the main computational advantages of standard Lattice Boltzmann Methods, offering high amenability to parallelization, that can be exploited to write efficient codes. These aspects are covered in the last chapter of the thesis, in which we summarize the best practices in the development of a performance portable code targeting modern high performance computing accelerators.

Riepilogo

In questo lavoro di tesi viene presentata la derivazione algoritmica di una nuova classe di metodi reticolari di Boltzmann per lo studio di fluidi relativistici.

Se da un lato i modelli sin'ora presenti in letteratura consideravano solo particelle a massa nulla ed equazioni di stato ultra-relativistiche, questo lavoro rappresenta un significativo passo in avanti verso la formulazione di un metodo cinetico unificato, in grado di trattare gas relativistici ideali, sia massivi sia a massa trascurabile, spaziando tra regimi relavitistici e regimi classici.

Come primo esempio di applicazione viene presentato uno studio atto a chiarire la problematica connessione tra teoria cinetica e teoria idrodinamica relativistica: a seguito di un'accurata analisi dei coefficienti di trasporto relativistici, vengono presentati dati numerici che evidenziano come l'espansione di Chapman Enskog leghi correttamente i coefficienti di trasporto cinetici con i parametri macroscopici idrodinamici relativistici, andando a confermare recenti studi teorici.

D'altro canto, l'analisi in questione può essere interpretata come un' accurata calibrazione di questa nuova classe di algoritmi, il che li candida ad affidabili strumenti per l'implementazione di simulazioni numeriche di sistemi fisici reali. Come esempio viene preso in considerazione lo studio del problema di Riemann per un quark-gluon plasma. I risultati ottenuti sono validati tramite confronto con simulazioni ottenute utilizzando altri risolutori numerici presenti in letteratura.

Come ulteriore applicazione, viene condotto uno studio sulle proprietà di trasporto degli elettroni nel grafene, in cui una descrizione idrodinamica è giustificata dal fatto che il moto collettivo degli elettroni risulta dominante

rispetto a interazioni tra elettroni e fononi. Utilizzando una formulazione numerica bidimensionale, arricchita per inglobare effetti elettrostatici e interazioni con fononi e impurità, vengono presentati risultati di simulazioni di flussi laminari in cui vengono riprodotte condizioni sperimentali simili a quelle reali. Successivamente sono stati presi in considerazione sistemi in cui termini non-lineari sono rilevanti. I risultati di un estensivo lavoro numerico hanno permesso di identificare parametri di trasporto che consentano l'osservazione di segnali preturbolenti in una regione idrodinamica quanto più simile a quella accessibile nelle attuali condizioni sperimentali.

Per finire, va sottolineato che i metodi numerici descritti in questo lavoro di tesi preservano dal punto di vista computazionale gli stessi vantaggi rispetto ai classici metodi reticolari di Boltzmann. Questi metodi numerici si prestano infatti a efficienti implementazioni altamente parallele. Questi aspetti sono dettagliati nell'ultimo capitolo di questa tesi, dove vengono riassunti gli elementi più rilevanti nello sviluppo di codici in grado di offrire non solo portabilità, ma anche portabilità delle prestazioni, su varie moderne architetture altamente parallele.

Zusammenfassung

In der vorliegenden Arbeit wird die algorithmische Entwicklung einer neuen Klasse von Lattice Boltzmann Methoden dargestellt, die zur Anwendung und Untersuchung von dissipativen, relativistischen Fluiden geeignet ist. Vorangehende Arbeiten sind eingeschränkt auf masselose Teilchen und damit auf ultrarelativistische Zustandsgleichungen. Im Gegensatz dazu werden in dieser Arbeit signifikante Fortschritte zur Formulierung einer einheitlichen, kinetischen Lattice Methode gemacht, die ideale Gase aus sowohl massiven wie auch fast masselosen Teilchen abdeckt und nahtlos auf den gesamten Bereich von nicht-relativistischen zu relativistischen Fluidregimen anwendbar ist. Der Übergang von der relativistischen, kinetischen Theorie zur relativistischen Hydrodynamik ist ein altes Problem. Eine erste, wichtige Anwendung der neuartigen, numerischen Methode dieser Arbeit führt hier zu neuen Erkenntnissen. Eine präzise Analyse der relativistischen Transportkoeffizienten unter Verwendung der Zeitrelaxationsnäherung ist durchgeführt worden. Damit konnte numerisch nachgewiesen werden, dass die Chapman-Enskog-Entwicklung die kinetischen Transportkoeffizienten und die makroskopischen, hydrodynamischen Parameter in der dissipativen, relativistischen Fluiddynamik korrekt in Beziehung setzt. Dies bestätigt neuere, theoretische Resultate.

Umgekehrt kann diese Analyse als präzise Kalibrierung dieser Klasse von numerischen Lösern verstanden werden, um so die Genauigkeit für Berechnungen im relativistischen Regime zu erhöhen. Anhand des Riemann Problems für ein Quark-Gluon-Plasma vergleichen wir Simulationsergebnisse unserer Methode mit bekannten Ergebnissen von anderen Lösern aus der Literatur.

In einer weiteren Anwendung untersuchen wir die Transporteigen-

schaften von Elektronen in extrem reinen Graphen-Proben. Hierbei ist eine hydrodynamische Beschreibung geeignet, da die Elektron-Elektron-Streuung die Elektron-Phonon-Interaktion dominiert. Basierend auf 2D-Formulierungen, einem externen elektrostatischen Antrieb und der Erfassung von Wechselwirkungen von Phononen mit Verunreinigungen präsentieren wir Simulationen einer laminaren Strömung. Dabei berücksichtigen wir die Geometrie des zugrundeliegenden physikalischen Experiments. Ferner betrachten wir elektrische Systeme, in denen nichtlineare Effekte an Bedeutung gewinnen. Auf der Grundlage einer umfassenden Menge von numerischen Simulationen identifizieren wir Transportparameter, welche man verwenden könnte, um präturbulente Signale auszulösen bzw. zu beobachten. Dabei sind entsprechende hydrodynamische Regime so nah wie möglich an den aktuellen Bedingungen der Experimente.

Abschließend sei angemerkt, dass die numerischen Methoden dieser Arbeit die rechentechnischen Vorzüge der standard Lattice Boltzmann Methode erhalten. Dies schließt insbesondere ein hohes Maß an Parallelisierbarkeit ein, welche genutzt werden kann, um effiziente Löser zu programmieren. Diesen Aspekten ist das letzte Kapitel der Arbeit gewidmet. Hierbei fassen wir beste Verfahren zur Entwicklung von performanten, portablen Programmen im Kontext von modernen Hochleistungsrechenbeschleunigern zusammen.

Contents

Introduction

Relativistic fluid dynamics plays an increasingly important role in several fields of modern physics, with applications stretching over widely different scales. For a long time its phenomenological applications have mostly pertained to the study of ideal non-viscous fluids in the broad realm of astrophysics. The past decade has seen important experimental progress in the physics of high-energy heavy-ion collisions, with the first clear observational evidence of the quark gluon plasma (QGP). Experimental data coming from the Relativistic Heavy-Ion Collider (RHIC) and the Large Hadron Collider (LHC), have significantly boosted the interest in the study of viscous relativistic fluid dynamics, both at the level of theoretical formulations as well as in the development of reliable numerical simulation methods, which enable to accurately describe the collective behavior observed in QGP. Perhaps unexpectedly, relativistic hydrodynamics has recently found application also in the field of condensed matter physics, for the study of strongly correlated electronic fluids in exotic material such as graphene and Weyl semi-metals.

The definition of a consistent theory for the study of a relativistic viscous fluid is, however, problematic. Indeed, it has long been recognized that a naive relativistic extension of the Navier-Stokes equations is inconsistent with relativistic invariance, as it implies superluminal propagation, hence non-causal and unstable behavior. This can be corrected by resorting to fully-hyperbolic formulations of relativistic hydrodynamics; while various framework have been proposed, the definition of second-order relativistic viscous hydrodynamic equations is still an open problem with a lot of ongoing research.

Historically, the first second-order theory approach for viscous hydrodynamics was proposed by Israel and Stewart. Although the Israel and

Stewart formulation has been widely considered as the reference frame for several decades, recent developments have highlighted theoretical shortcomings and, at least for some special problems, poor agreement with numerical solutions of the Boltzmann equation. Incidentally, but relevant for what follows, the work of Israel and Stewards stems from a relativistic extension of Grad's method of moments, a mathematical formalism commonly employed to establish a link between the classic Navier-Stokes equations and the Boltzmann equation. Another pathway often used to derive macroscopic equations from the kinetic layer is the Chapman-Enskog expansion. It is well known that in non-relativistic regimes both the Grad's moments method and the Chapman-Enskog approach connect kinetic theory and hydrodynamics in a consistent way, providing the same expressions for the transport coefficients. However, when applied to relativistic regimes the two methods lead to slightly different results. While many theoretical works, as well as numerical investigations, seem to converge towards the results provided by the CE approach, the question is still object of debate.

In recent years, numerical schemes based on the Lattice Boltzmann Method (LBM) have emerged as a promising tool for the study of dissipative hydrodynamics in relativistic regimes. The strength of this approach is that, by working at a mesoscopic level, viscous effects are naturally included, with relativistic invariance and causality preserved by construction. However, this field needs further developments: for instance, relativistic extensions of the LBM have so far been derived only for an ideal gas of massless particles.

The work described in this thesis starts from this background and further works in the development of relativistic LBMs and their potential applications. In fact, we significantly widen the application range, introducing a new relativistic lattice Boltzmann method (RLBM) based on finite-mass (pseudo-)particles, which allows to accurately and efficiently describe relativistic fluid dynamics in a broad range of kinematic regimes and temperatures, conceptually bridging the gap between the ultra-relativistic regime all the way down to the non-relativistic one. These numerical schemes are derived in flat space-time coordinates in $(3+1)$, $(2+1)$ as well as $(1+1)$ dimensions. The relativistic Boltzmann equation is discretized using Gauss-type quadratures on space-filling Cartesian lattices, preserving the computational advantages of the classic LBM.

One first important result, obtained as an application of this novel RLBM, is an accurate analysis of the relativistic transport coefficients in the relaxation time approximation (RTA). This work reflects the importance of numerical simulations in physical contexts in which a controlled

experimental setup is not a viable option. We present results bringing new insight in the long standing problem of understanding the pathway from relativistic kinetic theory to relativistic hydrodynamics. We provide for the first time, to the best of our knowledge, clear-cut numerical evidence that the Chapman Enskog expansion accurately relates kinetic transport coefficients and macroscopic hydrodynamic parameters in dissipative relativistic fluid dynamics, confirming recent theoretical results. At the same time, our methodology provides for the first time an accurate calibration procedure to simulate realistic physics systems using RLBM. Furthermore, we present results of simulations solving the Riemann problem for a quark-gluon plasma, showing good agreement with previous results obtained using other solvers present in the literature.

Another important result presented in this thesis introduces Lattice Boltzmann methods to a new application area in the broad context of exotic materials in condensed matter physics. We apply suitable RLBM formulations to the study of the electronic properties of graphene, where recent experimental studies have shown that certain features of the flow of electrons may be explained through a pseudo-relativistic hydrodynamic approach. We present simulations of laminar flows in ultra-clean graphene samples; we reproduce the geometrical setups used in actual experiments, and give numerical evidence of the formation of electron back-flows (whirlpools) in the proximity of current injectors.

Taking a further step, we then move towards regimes where nonlinear effects start becoming relevant. We present realistic simulations, accounting for electrostatic interactions and dissipative electron-phonon scattering, and propose experimentally realizable geometries capable of sustaining electronic preturbulence in graphene samples. We identify transport parameters for which preturbulent signals occur at experimentally achievable values of the Reynolds number and manifest through temporal fluctuations of the electrochemical potential. These results determine for the first time in a controlled way a range of transport coefficients and experimental geometries that experimentalist may target in order to observe preturbulence in electronic fluids: this parameter space is not experimentally viable today but it is reasonable to expect that it can be explored in the near future using improved experimental techniques and device fabrication processes.

We now outline the structure of the following chapters of this thesis work. In Chapter 1 we introduce the basic principles of relativistic kinetic theory. The relativistic Boltzmann equation is presented in the relaxation time approximation and we discuss the problem associated to the macroscopic

description of a relativistic fluid, as well as in the definition of the correct link between the kinetic and the macroscopic layers.

Chapter 2 is the first containing original results of our work; we describe the algorithmic derivation of a *unified* model which allows to cover a wide range of relativistic regimes, in principle all the way from fluids of ultra-relativistic massless particles down to non-relativistic fluids. Crucial in the derivation of the method is the polynomial expansion of the equilibrium distribution. The relativistic Boltzmann equation is then discretized in flat space-time coordinates in $(3+1)$, $(2+1)$ and $(1+1)$ dimensions by means of Gauss-type quadratures on space-filling Cartesian lattices. We finally detail the calibration procedure used to define the transport coefficients of the model, linking their physical values to those used on the Lattice. The numerical method is then validated using a well known instance of the Riemann problem, namely the Sod's shock tube.

Chapter 3 describes our original results in the application of LBM to describe the properties of exotic materials. We consider the study of electron flows in graphene samples. We perform simulations in both laminar and unsteady regimes; our most important result is the elucidation of the geometrical and transport properties of graphene samples that make it possible to experimentally detect preturbulent behavior in ultra-clean graphene sheets.

This work has relied on extensive numerical simulations on GPU clusters. In Chapter 4 we describe the large implementation and optimization effort that has gone to develop computer codes for our algorithm that run efficiently on recent high performance computing architectures.

Finally, in the last chapter we summarize all our results and take-away lessons, and give an outlook on future perspectives.

The notation used throughout this thesis work is defined in Appendix A. Appendices B-E contains the relevant mathematical details for the derivation of the RLBM.

1

Relativistic Boltzmann Equation

Abstract

The beginning of the relativistic kinetic theory dates back to 1911 when Jüttner [1] derived the equilibrium distribution function for a non-degenerate relativistic gas, later extended by Jüttner himself to account for systems of bosons and fermions [2]. The covariant formulation of the Boltzmann equation came in 1940 thanks to the work of Lichnerowicz and Marrot [3], followed two decades later by the determination of the transport coefficients using the Chapman-Enskog expansion by Israel [4] and Kelly [5]. This chapter introduces the basic principles of relativistic kinetic theory which will serve as the starting point for the derivation of the numerical schemes presented in the following chapters. A few fundamental references on formulation of relativistic kinetic theory are the books by Stewart [6], De Groot [7], Cercignani and Kremer [8], alongside the recent monograph of Rezzolla and Zanotti [9] and the review by Paul and Ulrike Romatschke [10].

In kinetic theory the system of microscopic particles forming a gas is based on a statistical description in terms of the one-particle distribution function. For an ideal non-degenerate relativistic fluid, consisting at the kinetic level of a system of interacting particles of rest mass m, the particle distribution function $f((x^\alpha),(p^\alpha))$, depending on space-time coordinates $(x^\alpha) = (ct, \boldsymbol{x})$ and momenta $(p^\alpha) = \left(p^0, \boldsymbol{p}\right) = \left(\sqrt{\boldsymbol{p}^2 + m^2c^2}, \boldsymbol{p}\right)$, with $\alpha = 0, 1, 2, 3$, is

defined such that the quantity

$$f((x^\alpha),(p^\alpha))\,\mathrm{d}^3x\,\mathrm{d}^3p = f((x^\alpha),(p^\alpha))\,\mathrm{d}x^1\,\mathrm{d}x^2\,\mathrm{d}x^3\,\mathrm{d}p^1\,\mathrm{d}p^2\,\mathrm{d}p^3 \quad , \tag{1.1}$$

gives the number of particles in a volume element in phase-space $\mathrm{d}^3x\,\mathrm{d}^3p$. It is clear that the number of particles is a scalar invariant, since all the observer will count the same number of particles. Furthermore, while d^3x and d^3p alone are not Lorentz invariant, it can be shown that both d^3p/p_0 and the volume element $\mathrm{d}^3x\,\mathrm{d}^3p$ are Lorentz invariants. It follows that $f((x^\alpha),(p^\alpha))$ is itself a scalar invariant. The time evolution of the particle distribution is ruled by the relativistic Boltzmann equation

$$p^\alpha \frac{\partial f}{\partial x^\alpha} + m\frac{\partial f K^\alpha}{\partial p^\alpha} = \Omega \quad , \tag{1.2}$$

where K^α represents the external forces acting on the system, and Ω is the collisional operator, which can be expressed as a integral of the product of one-particle distribution functions in the momentum-space. Much like in the classical case, the analytical derivation of Ω is built on a set of assumptions, refereed to by Boltzmann as Stoßzahlansatz (molecular chaos):

- Only scattering processes between pairs of particles are taken into account. We use the abbreviation $f = f((x^\alpha),(p^\alpha))$ and $f' = f((x^\alpha),(p'^\alpha))$ to distinguish between the distribution function of two pairing particles.

- There is no correlation between particles entering a collision. We use the abbreviation $f = f((x^\alpha),(p^\alpha))$ and $f_* = f((x^\alpha),(p^\alpha_*))$ to distinguish between the distribution function of a particle before and after collision.

Using these assumptions Lichnerowicz and Marrot [3] were the first in 1940 to introduce the covariant formulation of the Boltzmann equation, with the analytical expression for Ω

$$\Omega = \int_{\mathbb{R}^3} \left(f'_* f' - f_* f\right) \sigma\,\mathrm{d}\Psi \frac{\mathrm{d}^3p_*}{p^0_*} \quad , \tag{1.3}$$

where σ and $\mathrm{d}\Psi$ denote respectively the differential cross-section and the element of solid angle that characterizes a binary collision. Two important properties of the collisional term are the following:

- For any collisional invariant quantity ψ (examples are $\psi \in \{c, cp^\alpha\}$):

$$\int_{\mathbb{R}^3} \Omega \psi \frac{\mathrm{d}^3 p}{p^0} = 0 \quad . \tag{1.4}$$

- The H-theorem holds:

$$\int_{\mathbb{R}^3} \Omega H(f) \frac{\mathrm{d}^3 p}{p^0} = 0 \quad , \tag{1.5}$$

  where $H(f)$ is a convex function in f, e.g. $f \ln(f)$.

As in the non-relativistic case, the equilibrium is characterized by the condition $f'_* f' = f_* f$ implying a vanishing collisional term. It is well known that the equilibrium distribution function for the non-relativistic case is given by the Maxwell-Boltzmann distribution. Its relativistic counterpart was derived at the beginning of the past century by Jüttner [1] and takes the name of Maxwell-Jüttner distribution:

$$f^{\mathrm{eq}} = A(n,T) e^{-\frac{U^\alpha p_\alpha}{k_\mathrm{B} T}} \quad , \tag{1.6}$$

with the normalization factor

$$A(n,T) = \frac{n}{4\pi m^2 c k_\mathrm{B} T K_2(\zeta)} \quad , \tag{1.7}$$

where n is the particle density, T the temperature, (U^α) is the four-velocity vector, k_B is the Boltzmann constant, $\zeta = mc^2/k_\mathrm{B}T$, and K_2 is the modified Bessel function of second kind. The definition of the normalization factor for f^{eq} will be discussed in the coming sections.

It has to be mentioned that in recent years several authors [11–13] have argued that Eq. 1.6 might not represent the correct relativistic equilibrium distribution, and a few possible alternatives have been suggested [13, 14]. However, several works [15–17] have later confirmed that the Maxwell-Jüttner distribution is the correct generalization of Maxwell's velocity distribution in special relativity.

1.1 Macroscopic Description

The macroscopic description of a relativistic fluid can be characterized by the moments of the distribution function [8]. Of particular interest are the

first two moments of the distribution, which alone fully describe a fluid at equilibrium. They are respectively the particle four flow:

$$N^\alpha = c \int_{\mathbb{R}^3} f p^\alpha \frac{\mathrm{d}^3 p}{p_0} \quad , \tag{1.8}$$

and the energy-momentum tensor:

$$T^{\alpha\beta} = c \int_{\mathbb{R}^3} f p^\alpha p^\beta \frac{\mathrm{d}^3 p}{p_0} \quad . \tag{1.9}$$

Higher order moments do not have names; we introduce the third order moment which will be relevant, as we will see in the later chapters, for the study of dissipative effects:

$$T^{\alpha\beta\gamma} = c \int_{\mathbb{R}^3} f p^\alpha p^\beta p^\gamma \frac{\mathrm{d}^3 p}{p_0} \quad . \tag{1.10}$$

The balance equations of the particle four-flow and of the energy-momentum tensor give origin to the conservation equations:

$$\begin{aligned} \partial_\alpha N^\alpha &= 0 \quad , \\ \partial_\alpha T^{\alpha\beta} &= 0 \quad . \end{aligned} \tag{1.11}$$

Eqs. 1.11 are purely formal until a specific decomposition for N^α and $T^{\alpha\beta}$ in terms of quantities that appear in non-relativistic fluid dynamics is introduced. It can be shown (see e.g. [9]) that the decomposition for an ideal fluid at the equilibrium is given by:

$$N_E^\alpha = n U^\alpha \quad , \tag{1.12}$$

$$T_E^{\alpha\beta} = \frac{1}{c^2}(P + \epsilon) U^\alpha U^\beta - P \eta^{\alpha\beta} \quad , \tag{1.13}$$

where n is the particle density, P the hydrostatic pressure and ϵ the energy density. The subscript E indicates that the tensors are evaluated at the equilibrium.

In order to capture dissipative properties in the dynamics of the fluid, extra higher order terms need to be taken into account in Eq. 1.13. These terms can be defined with the help of the hydrodynamic four-velocity U^α. The two most common decompositions used in the literature are respectively known as the Eckart [18] and the Landau-Lifshitz [19] decomposition. The difference between the two approaches lies in the choice made in the definition of the macroscopic four-velocity: in Eckart's formulation, the four-

velocity is directly related to the particle flux, while in Landau-Lifshitz's approach it is directly related to the energy flux.

1.1.1 Eckart decomposition

In the Eckart decomposition the hydrodynamic velocity is directly linked to the particle four-flow N^α through:

$$U^\alpha = \frac{cN^\alpha}{\sqrt{N^\beta N_\beta}} \quad , \tag{1.14}$$

where the normalization is in agreement with Eq. A.21. As a consequence of this definition, the continuity equation retains the same expression as for a perfect fluid, with extra terms appearing only in the energy-momentum tensor:

$$N^\alpha = N_E^\alpha \quad , \tag{1.15}$$

$$T^{\alpha\beta} = T_E^{\alpha\beta} + \pi^{<\alpha\beta>} - \varpi\Delta^{\alpha\beta} + \frac{1}{c^2}\left(U^\alpha q^\beta + U^\beta q^\alpha\right) \quad , \tag{1.16}$$

with the following definition for the particle number density n, the pressure deviator $\pi^{<\alpha\beta>}$, the static (dynamic) pressure P (ϖ), the energy density ϵ and the heat flux q^α:

$$n = \frac{1}{c^2}N^\alpha U_\alpha \quad , \tag{1.17}$$

$$\pi^{<\alpha\beta>} = \left(\Delta_\gamma^\alpha\Delta_\delta^\beta - \frac{1}{3}\Delta^{\alpha\beta}\Delta_{\gamma\delta}\right)T^{\gamma\delta} \quad , \tag{1.18}$$

$$P + \varpi = -\frac{1}{3}\Delta_{\alpha\beta}T^{\alpha\beta} \quad , \tag{1.19}$$

$$\epsilon = \frac{1}{c^2}U_\alpha T^{\alpha\beta}U_\beta \quad , \tag{1.20}$$

$$q^\alpha = \Delta_\gamma^\alpha U_\beta T^{\beta\gamma} \quad , \tag{1.21}$$

where

$$\begin{aligned} \Delta^{\alpha\beta} &= \eta^{\alpha\beta} - \tfrac{1}{c^2}U^\alpha U^\beta \quad , \\ \Delta_\beta^\alpha &= \Delta^{\alpha\gamma}\Delta_{\gamma\beta} \quad . \end{aligned} \tag{1.22}$$

1.1.2 Landau-Lifshitz decomposition

In the Landau-Lifshitz decomposition the hydrodynamic velocity is, instead, taken to be proportional to the energy flux, according to the following

implicit definition:

$$U^\alpha = \frac{cT^{\alpha\beta}U_\beta}{\sqrt{U_\gamma T^{\gamma\delta}T_{\gamma\delta}U^\delta}} \quad , \tag{1.23}$$

again with the normalization in agreement with Eq. A.21. This choice for the hydrodynamic velocity leads to the following decomposition for N^α and $T^{\alpha\beta}$:

$$N^\alpha = N_E^\alpha + \chi^\alpha \quad , \tag{1.24}$$

$$T^{\alpha\beta} = T_E^{\alpha\beta} + \pi^{<\alpha\beta>} - \varpi\Delta^{\alpha\beta} \quad , \tag{1.25}$$

with χ^α the non-equilibrium part of the particle four flow. It can be shown that for processes close to the equilibrium all the definitions in Eq. 1.17 hold in this case as well, with the exception of the heat flux which can instead be related to χ^α through

$$\chi^\alpha = -\frac{n}{P+\epsilon}q^\alpha \quad . \tag{1.26}$$

To conclude it can be interesting to put in relation the two definition of the four velocity given respectively by Eckart, here U^α_{EK}, and Landau-Lifshitz, U^α_{LL}. Assuming a process close to equilibrium it can be shown [8] that

$$U^\alpha_{\text{EK}} = U^\alpha_{\text{LL}} - \frac{1}{P+\epsilon}q^\alpha \quad . \tag{1.27}$$

1.2 The laws of Navier-Stokes and Fourier

Starting from the conservation equations (Eq. 1.11) and combining them, for example, with the Eckart decomposition (Eq. 1.15) one can derive (see [8] or [9] for full details) the most straightforward relativistic formulation of the laws of Navier-Stokes and Fourier:

$$\begin{aligned} \varpi &= -\mu \ \nabla_\alpha U^\alpha \quad , \\ \pi^{<\alpha\beta>} &= \eta \ \left(\Delta^\alpha_\gamma\Delta^\beta_\delta + \Delta^\alpha_\delta\Delta^\beta_\gamma - \tfrac{2}{3}\Delta^{\alpha\beta}\Delta_{\gamma\delta}\right)\nabla^\gamma U^\delta \quad , \\ q^\alpha &= \lambda \ \left(\nabla^\alpha T - \tfrac{T}{c^2}U^\alpha\partial_\beta U^\beta\right) \quad , \end{aligned} \tag{1.28}$$

where ϖ is the dynamic pressure and the coefficients η, μ, λ are respectively the shear viscosity, bulk viscosity and thermal conductivity, with

$$\nabla^\alpha = \Delta^{\alpha\beta}\partial_\beta \quad . \tag{1.29}$$

This formulation represents the simplest covariant generalizations of the Navier–Stokes and Fourier equations and it can indeed be shown that in the non-relativistic limit ($v \ll c$) one recovers

$$\begin{aligned} \varpi &= -\mu \quad \boldsymbol{\nabla u} \quad , \\ \pi^{<0\alpha>} = \pi^{<\alpha 0>} &= 0 \quad , \\ \pi^{<ij>} &= \eta \quad \left(\boldsymbol{\nabla}^i u^j + \boldsymbol{\nabla}^j u^i - \tfrac{2}{3}\boldsymbol{\nabla}^k u^k \delta^{ij}\right) \quad , \\ q^0 &= 0 \quad , \\ q^i &= \lambda \quad \nabla^i T \quad , \end{aligned} \tag{1.30}$$

A few comments are in place: to start, one can see from Eq. 1.28 that a first significant difference between the relativistic case and the non-relativistic one is that even for iso-thermal fluids there could be a non-zero heat-flux due to a pressure gradient. The most important comment however is that although building on solid physical justification, both from thermodynamics [20] and kinetic theory [8], Eq. 1.28 are not causal: thermodynamic fluxes $(\varpi, \pi^{<\alpha\beta>}, q^\alpha)$ react instantaneously to the corresponding thermodynamic forces (RHS in Eq. 1.28), implying the propagation of signals at infinite speeds. Over the years several approaches have been proposed to restore causality in the description of dissipative relativistic hydrodynamics with the Israel and Stewart (IS) framework [21–23] having emerged as one of the best dynamic tools to reproduce experimental observables. However, recent developments have highlighted theoretical shortcomings in the derivation of the IS equations [24], as well as poor agreement with numerical solutions of the Boltzmann equation [25, 26]. In this context, as will be discussed thoroughly in the next chapter, approaches based on the mesoscopic layer have emerged as valuable and promising alternatives, circumventing the problematics related to the direct study of the macroscopic relativistic hydrodynamics laws. Before going into further details, we introduce in the next section a few simplified models for the collisional operator of the Boltzmann equation.

1.3 Relaxation Time Approximation

Because of the complex nature of the collisional operator, which depends on the product of distribution functions, it is customary to replace Ω in Eq. 1.2 with collisional models, typically linearized version of Ω, capable of preserving some of the basic properties or the full collisional. In non-

relativistic theory the arguably best known collisional model is the BGK model [27], which describes the evolution of the system as a time relaxation to the equilibrium.

In this section we describe two widely used relaxation time collision models for the relativistic Boltzmann equation, the model of Marle and the model of Anderson-Witting. Both models fulfill the properties of the true collisional term described by Eq. 1.4 and Eq. 1.5.

1.3.1 Model of Marle

The model of Marle [28, 29] is a relativistic extension of the BGK model. It is compatible with the Eckart decomposition, and it is given by

$$\Omega = \frac{m}{\tau_M}\left(f^{\mathrm{eq}} - f\right) \quad , \tag{1.31}$$

where τ_M is the characteristic (proper)-time between subsequent collisions. The model of Marle is appropriate only for the study of mildly relativistic fluids, since it implies an infinite relaxation time in the limit where the mass of the particles becomes zero. Attempts to cure these limitation have been described by Takamoto and Inutsuka [30] who proposed a modified Marle model.

1.3.2 Model of Anderson-Witting

With the idea of establishing a relaxation time approximation model capable of dealing with both mildly and ultra-relativistic gas of particles, Anderson and Witting [31, 32] proposed the following model:

$$\Omega = \frac{U^{\alpha}p_{\alpha}}{c^2\tau_{AW}}\left(f^{\mathrm{eq}} - f\right) \quad . \tag{1.32}$$

The model is compatible with the Landau-Lifshitz decomposition.

1.4 Transport Coefficients

The transport coefficients encountered in the previous sections, namely the heat-flux, bulk and shear viscosity, provide the connection between the kinetic and the macroscopic description of a dissipative fluid. In non-relativistic regimes, the derivation of appropriate transport coefficients is typically obtained with either Grad's method of moments [33] or the

Chapman-Enskog (CE) expansion [34], with both techniques allowing a consistent connection between kinetic theory and hydrodynamics, i.e. they provide the same expressions for the transport coefficients. When taking into consideration relativistic regimes the picture becomes rather controversial: not only the definition of the hydrodynamic layer is problematic (as discussed in Section *1.2*), also the correct ladder to be taken when climbing from the kinetic to the hydrodynamic layer is object of debate, with Grad and CE giving slightly different results in the expressions of the transport coefficients.

In recent times, the problem has been object of several studies. While many theoretical works, as well as numerical investigations, seem to converge towards the results provided by the CE approach, the question is still object of debate. Conceptual shortcomings of the moments method, which have recently been highlighted also in the non-relativistic framework [35–38], revolve around the use of second-order spatial derivatives in constitutive hydrodynamical equations [39]. On the other hand, objections to the relativistic Chapman-Enskog expansion point to its link to relativistic Navier-Stokes equations, which suffer of basic problems, such as broken causality and resulting instabilities [24, 40].

The derivation of the IS equations is itself highly based on Grad's method, it is therefore not obtained as a controlled expansion in some small parameter. Denicol et al. [24, 40, 41] have proposed an extension of the moments methods in which the resulting equations of motion are derived directly from the Boltzmann equation and truncated by a systematic power-counting scheme in Knudsen number. Remarkably, is has been shown that the expression for the transport coefficients provided by the CE expansion is approached when a larger number of moments (with respect to the 14 used in the IS formulation) is taken into account. Similar conclusions can be found in the work of Jaiswal et. al [42], where by including entropic arguments within Grad's method, they derived relativistic dissipative hydrodynamics equations in the same form as those given by IS, although with different expressions for the transport coefficients, which are again in good agreement with those calculated via the Chapman-Enskog expansion. A rather different approach was introduced in a series of works by Tsumura et al [39, 43–45], where renormalization group techniques are applied to the Boltzmann equation. Once again, the expressions for bulk (shear) viscosity and heat conductivity derived using this methodology, coincide with those provided by the Chapman-Enskog method.

These analytic works are mostly restricted to the ultra-relativistic

limit. Nevertheless, the appropriateness and accuracy of the CE method is confirmed by a series of numerical investigations [46–48].

1.5 Equation of State

The closure for the conservation equations is given by the Equation of State (EOS). The general EOS for a perfect gas in $(3+1)$ dimensions, valid for any value of the relativistic parameter $\zeta = \frac{mc^2}{k_B T}$, was first derived by Karsch et al. [49]:

$$\begin{aligned} \epsilon &= P\left(3 + \zeta \tfrac{K_1(\zeta)}{K_2(\zeta)}\right) \quad . \\ P &= nk_B T \quad . \end{aligned} \tag{1.33}$$

In the next chapter we will derive a numerical method which will be specialized also in $(2+1)$ and $(1+1)$ dimensions; since these two cases are rarely fully discussed in the literature, the derivation of their general equation of state is presented in this section. To this aim, it is instructive to briefly summarize a possible approach for the derivation of Eq. 1.33.

In what follows one needs to handle integrals in the form of

$$\int_{\mathbb{R}^D} f^{\mathrm{eq}} p^\alpha \dots p^\omega \frac{\mathrm{d}\boldsymbol{p}}{p_0} = \int_{\mathbb{R}^D} A \exp\left(-\frac{p^\nu U_\nu}{k_B T}\right) p^\alpha \dots p^\omega \frac{\mathrm{d}\boldsymbol{p}}{p_0} = A Z^{\alpha \dots \omega} \quad . \tag{1.34}$$

details on their calculation are given in Appendix B. The normalization factor A needs to be chosen such to satisfy Eq. 1.12. This constraint, together with the analytical expression for Z^α, translates in the following condition:

$$\int_{\mathbb{R}^3} f^{\mathrm{eq}} p^\alpha \frac{\mathrm{d}p^3}{p_0} = A\ Z^\alpha = A\ 4\pi m^2 k_B T K_2(\zeta) U^\alpha = n U^\alpha \quad , \tag{1.35}$$

from which we can determine the correct normalization factor for the equilibrium distribution function

$$A = \frac{n}{4\pi m^2 k_B T K_2(\zeta)} \quad , \tag{1.36}$$

previously introduced in Eq. 1.6. Next, we plug the normalization factor A in $Z^{\alpha\beta}$ giving

$$Z^{\alpha\beta} = \frac{n k_B T}{K_2(\zeta)} \left(\frac{m}{k_B T} K_3(\zeta)\ U^\alpha U^\beta - K_2(\zeta)\ \eta^{\alpha\beta}\right) \quad . \tag{1.37}$$

In order to identify the equation of state it is sufficient to compare the above expression with $T_E^{\alpha\beta}$ in Eq. 1.12 and observe that, by matching the terms with the same tensorial structure in these two expressions, it is possible to derive the following system of equations:

$$\begin{aligned} \epsilon + P &= n\, mc^2 \frac{K_3(\zeta)}{K_2(\zeta)} \quad , \\ P &= nk_{\rm B}T \quad . \end{aligned} \tag{1.38}$$

Recalling that $K_{\alpha+1}(x) = K_{\alpha-1}(x) + (2\alpha/x)K_\alpha(x)$ it is straightforward to show that the above coincides with Eq. 1.33.

By following the same procedure one can extend the EOS to the general $(D+1)$ dimensional case. In the following we provide a couple of examples reporting only the relation linking the energy density to the pressure, since the expression linking pressure temperature and particle density does not depend on D. Using the results provided in Appendix B it is simple to derive the EOS for $D < 3$. In particular in $(2+1)$ dimensions one gets:

$$\epsilon = P\left(1 + \zeta + \frac{1}{1+\zeta}\right) \quad . \tag{1.39}$$

Likewise in $(1+1)$ dimensions we obtain:

$$\epsilon = P\left(1 + \zeta\frac{K_0(\zeta)}{K_1(\zeta)}\right) \quad . \tag{1.40}$$

Clearly one can extend to higher dimensions as well, for example in $(4+1)$ dimensions one would get:

$$\epsilon = P\left(4 + \frac{\zeta^2(1+\zeta)}{3+3\zeta+\zeta^2}\right) \quad . \tag{1.41}$$

1.5.1 Ultra-relativistic limit

The ultra-relativistic EOS can be obtained taking the limit for $\zeta \to 0$ of respectively Eq. 1.33, 1.39, 1.40, 1.41. Noting that $xK_n(x)/K_{n+1}(x) \to 0$ as $x \to 0$ it is simple to obtain the well known result

$$\epsilon_{\rm ur} = DP \quad . \tag{1.42}$$

It is interesting to compare Eq. 1.42 with the correspondent general EOS to appreciate the difference in the various intermediate regimes. To this aim in Fig. 1.1 we plot the ratio between the general EOS and the ultra-relativistic one in several dimensions as a function of the temperature

T normalized in terms of a unit mass. We can appreciate the fact that in higher dimensions less energy is required to enter the ultra-relativistic limit.

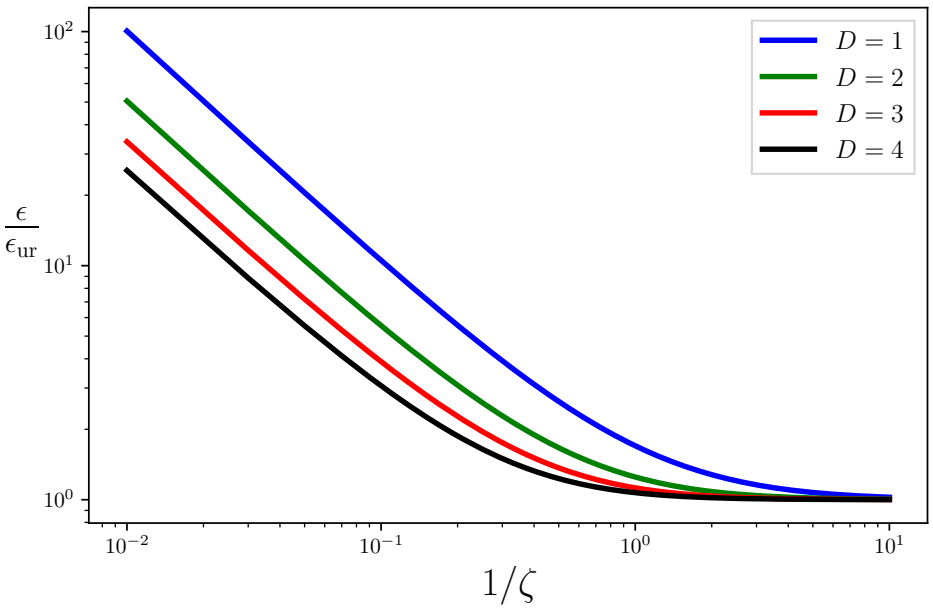

Figure 1.1: *Ratio between the energy density and its correspondent ultra-relativistic limit in several dimensions, as a function of temperature T, with T rescaled in units of m.*

1.5.2 Non-relativistic limit

For the non-relativistic limit we introduce the non-relativistic kinetic energy density $\epsilon_c = \epsilon - n\ m$ and take the limit for $\zeta \to \infty$ of Eq. 1.33,1.39,1.40,1.41. Using the fact that $(x\ K_\alpha(x)/K_{\alpha+1}(x) - x) \to -\alpha - 1/2$ as $x \to \infty$ one can recover the well known non-relativistic expression for the EOS of an ideal gas:

$$\epsilon_c = \frac{D}{2} P \quad . \tag{1.43}$$

2

Relativistic Lattice Boltzmann Method

Abstract

Relativistic kinetic theory and relativistic fluid dynamics play an increasingly important role in several areas of modern physics. In the past, many relativistic fluid dynamic studies have been performed in astrophysical contexts, however mostly confined to ideal non-viscous fluids. Dissipative effects, with aggregated problematics described in the previous chapter, play a major role in the realm of high-energy physics, especially in connection with quark-gluon plasma experiments in heavy-ion colliders, as well as in condensed matter physics for the study of electronic transport in exotic semi-metals such as graphene. Recently, numerical schemes based on the Lattice Boltzmann Method (LBM) have emerged as a promising tool for the study of dissipative relativistic hydrodynamics. The strength of this approach is that by working at a mesoscopic level viscous effects are naturally included, with relativistic invariance and causality preserved by construction. In this chapter we describe the extension of the LBM for the study of relativistic fluids, focusing in particular in the algorithmic derivation of a model which allows to cover a wide range of relativistic regimes, in principle all the way from fluids of ultra-relativistic massless particles down to non-relativistic fluids.

With Lattice Boltzmann Method [50] we refer to a class of numerical fluid-dynamics solvers which in the past decades have found application in several relevant physics problems including, for example, transport in porous media, high Reynolds turbulent flows, multi-phase flows and many more.

At variance with methods that discretize the Navies-Stokes equations, LBM stems from the mesoscopic layer, making use of a minimal version of the Boltzmann equation to provide a correct macroscopic description of a fluid system. The advection-collision scheme upon which it is based makes the method particularly suitable for implementation on highly parallel computer architectures, and indeed computational efficiency is one of the main reasons behind the success of LBM. In 2010 Mendoza et al. [51, 52] provided a first attempt to extend the method to the case of relativistic fluids. From the previous chapter one could appreciate how a lattice formulation is possibly even more appropriate, if not desirable, in the relativistic framework: the parabolic nature of the relativistic Navier-Stokes equations leads to the loss of causality altogether with intrinsic numerical instabilities. In this context a Relativistic Lattice Boltzmann Method (RLBM) emerges as a promising tool for the study of dissipative relativistic hydrodynamics, with its inherent finite-speed propagation restoring causality by construction. In this chapter, which is the first describing original results of this work, we start by providing a brief review of RLBM schemes already present in the literature to then describe in all details the algorithmic structure and the implementation of our improved models, based on massive (pseudo-)particles. This chapter also describes some important validation steps and calibration methods for our algorithm, presenting (for the first time to the best of our knowledge) convincing numerical evidence that the Chapman-Enskog procedure is the correct one to connect the meso-scale to the macro-scale layer in relativistic fluid dynamics.

2.1 Relativistic Lattice Boltzmann Method: a survey of early developments

The last decade has witnessed several attempts to develop LBM capable of handling the relativistic regime. The first model was developed by Mendoza et al. [51, 52], based on Grad's moment matching technique. Romatschke et al. [53] developed a scheme for an ultra-relativistic gas of particles based on the expansion with Laguerre polynomials of the Maxwell-Jüttner distribution, following a procedure similar to the one used for non-relativistic LBM. However, this model is not compatible with a Cartesian lattice, thus requiring interpolation to implement the streaming phase. Li et al. [54] have extended the work of Mendoza et al.

using a multi relaxation-time collisional operator, which, by independently tuning shear and bulk viscosity, has allowed the use of a Cartesian lattice. However, this model is not able to recover the third order moment of the distribution. Mohseni et al. [55] have shown that it is possible to avoid multi-time relaxation schemes, still using a Cartesian lattice and properly tuning the bulk viscosity for ultra-relativistic flows, so as to recover only the conservation of the momentum-energy tensor. This is a reasonable approximation in the ultra-relativistic regime, where the first order moment plays a minor role, but leaves open the problem of recovering higher order moments. A further step was taken in [56], with a RLBM formulation capable of recovering up to the third order of the Maxwell-Jüttner distribution on a Cartesian lattice. The model considers massless particles all traveling at the speed of light: as a consequence the quadrature is established on a grid identified by the intersection of a sphere of radius R and a Cartesian grid. This model could be in principle extended to recover arbitrarily high order moments, although this would require very large and impracticable values of R, hampering the efficiency and the resolution of the model. Blaga and Ambrus [57, 58] have developed a class of off-lattice quadrature-based models capable of including arbitrarily high order moments, thus supporting simulations well beyond the hydrodynamic regime, spanning in principle between the inviscid regime all the way to the ballistic regime. Several authors have attempted to adapt the various models above described to the study of $(2 + 1)$-dimensional relativistic hydrodynamics with the aim of applying the RLBM to the study of the electrons flow in graphene [59–63].

All these developments use pseudo-particles of zero proper mass m (or, more accurately, pseudo-particles for which the ratio particle of mass and temperature, $\zeta = mc^2/Tk_{\mathrm{B}}$, goes to zero). In the coming sections we will describe the algorithmic development of a model allowing to extend the range of physical applications by supporting mildly relativistic flows, conceptually bridging the gap between the ultra-relativistic regime all the way down to the non-relativistic one [64, 65].

Before going into details, it is first instructive to briefly revise the derivation of the classical LBM.

2.2 Detour: Derivation of classical Lattice Boltzmann models

The development of the LBM takes root in 1988 with the work of McNamara and Zanetti [66], with the intent of overcoming the limitations of the Lattice Gas Cellular Automaton approach [67, 68]. Soon after it evolved into a self-standing research topic [69–72] emerging as an efficient tool to simulate the dynamic behavior of fluid flows using a minimal form of the Boltzmann equation. Perhaps surprisingly, it was not until a decade later when it was realized that LBM can be formally derived using a Gauss-Hermite quadrature [73–75]. This elegant derivation, giving the method a solid mathematical foundation, will be summarized in this section; for a more exhaustive introduction the refer is invited to refer to e.g. [76].

Let us start from the classic Boltzmann equation based on the BGK collisional model [27] and in the absence of external forces:

$$\frac{\partial f}{\partial t} + \boldsymbol{\xi}\nabla f = \frac{1}{\tau}\left(f^{\mathrm{eq}} - f\right) \quad , \tag{2.1}$$

with the local equilibrium distribution f^{eq} corresponding to the Maxwell-Boltzmann distribution:

$$f^{\mathrm{eq}} = \rho\left(\frac{1}{2\pi T}\right)^{D/2} \exp\left(-\frac{1}{2T}(\boldsymbol{\xi} - \boldsymbol{u})^2\right) \quad . \tag{2.2}$$

In both Eq. 2.1 and Eq. 2.2 all quantities are made non-dimensional, in particular the microscopic $\boldsymbol{\xi}$ and the macroscopic velocities $\boldsymbol{u}$ ($\boldsymbol{\xi}, \boldsymbol{u} \in \mathbb{R}^D$), are implicitly scaled by the speed of sound $c_s = \sqrt{k_{\mathrm{B}} T_0 / m_0}$, where T_0 and m_0 are the characteristic temperature and molecular mass of a single component fluid. All the other quantities are made non-dimensional by means of a characteristic lenght scale Δx and a time scale Δt, chosen such that $\Delta x = c_s \Delta t$ holds.

The starting point for the discretization of Eq. 2.1 is a projection of the equilibrium distribution function onto a Hilbert sub-space spanned by orthogonal Hermite polynomials in the velocity space:

$$f^{\mathrm{eq}}(\boldsymbol{x}, \boldsymbol{\xi}, t) = \omega(\boldsymbol{\xi}) \sum_{k=0}^{\infty} \frac{1}{k!} \boldsymbol{a}^{(k)}(\boldsymbol{x}, t) \boldsymbol{H}^{(k)}(\boldsymbol{\xi}) \quad , \tag{2.3}$$

where $\omega(\boldsymbol{\xi})$ is a weighting function and $\boldsymbol{a}^{(k)}, \boldsymbol{H}^{(k)}$ are tensors of rank k, respectively the expansion projection coefficients and the Hermite polyno-

mials [77]. The weighting function is given by

$$\omega(\boldsymbol{\xi}) = \frac{1}{(2\pi)^{D/2}} \exp\left(-\frac{1}{2}\boldsymbol{\xi}^2\right) \quad , \tag{2.4}$$

while the projection coefficients are by definition

$$\boldsymbol{a}^{(k)}(\boldsymbol{x},t) = \int_{\mathbb{R}^D} f^{\mathrm{eq}}(\boldsymbol{x},\boldsymbol{\xi},t) H^{(k)}(\boldsymbol{\xi})\,\mathrm{d}\boldsymbol{\xi} \quad . \tag{2.5}$$

The reason for using the Hermite polynomials as an expansion basis for the Maxwell-Boltzmann distribution is that, as first observed by Grad in 1949 [33, 77], the expansion coefficients correspond exactly to the hydrodynamic moments of the distribution:

$$\begin{aligned}
\boldsymbol{a}^{(0)} &= \int_{\mathbb{R}^D} f^{\mathrm{eq}}\,\mathrm{d}\boldsymbol{\xi} && = \rho \quad , \\
\boldsymbol{a}^{(1)} &= \int_{\mathbb{R}^D} f^{\mathrm{eq}} \cdot \boldsymbol{\xi}\,\mathrm{d}\boldsymbol{\xi} && = \rho\boldsymbol{u} \quad , \\
\boldsymbol{a}^{(2)} &= \int_{\mathbb{R}^D} f^{\mathrm{eq}} \cdot (\boldsymbol{\xi}\boldsymbol{\xi} - \boldsymbol{I})\,\mathrm{d}\boldsymbol{\xi} && = \rho\boldsymbol{u}\boldsymbol{u} + \rho(T-1)\boldsymbol{I} \quad ,
\end{aligned} \tag{2.6}$$

where $\boldsymbol{I}$ is the identity matrix. We have here adopted the shorthand notation of Grad [77], for which the product of two tensors, e.g. $\boldsymbol{u}\boldsymbol{v}^{(k)}$, stands for $u_i v^{(k)}_{jk} + u_j v^{(k)}_{ik} + u_k v^{(k)}_{ji}$. Since only the low orders of the distribution are of interest for a hydrodynamic description, it is possible to consider a finite truncation of Eq. 2.3 to a certain order N,

$$f^{\mathrm{eq}}_N(\boldsymbol{x},\boldsymbol{\xi},t) = \omega(\boldsymbol{\xi}) \sum_{k=0}^{N} \frac{1}{k!} \boldsymbol{a}^{(k)}(\boldsymbol{x},t) \boldsymbol{H}^{(k)}(\boldsymbol{\xi}) \quad , \tag{2.7}$$

which by construction preserves exactly the moments of the original distribution function up to order N. With this knowledge the velocity discretization of Eq. 2.1 can be turned into a quadrature problem.

We are interested in approximating integrals in the form of Eq. 2.5, where the equilibrium distribution is replaced with its N-th order truncation. In order to employ a Gauss-Hermite quadrature the integrand needs to be expressed in the form

$$\omega(\boldsymbol{\xi}) p(\boldsymbol{x},\boldsymbol{\xi},t) = f^{\mathrm{eq}}_N(\boldsymbol{x},\boldsymbol{\xi},t)\ \boldsymbol{H}^{(k)}(\boldsymbol{\xi}) \quad . \tag{2.8}$$

Since both $f^{\mathrm{eq}}_N(\boldsymbol{x},\boldsymbol{\xi},t)/\omega(\boldsymbol{\xi})$ and $\boldsymbol{H}^{(k)}(\boldsymbol{\xi})$ are polynomials in ξ of degree N at most, the polynomial $p(\boldsymbol{x},\boldsymbol{\xi},t)$ has degree $2N$ at most. Assume now

that a given set of weights w_i and abscissas $\boldsymbol{e}_i$, $\{(w_i, \boldsymbol{e}_i), i = 0, \ldots, l\}$, provide a quadrature of algebraic degree of precision $> 2N$. It follows that the coefficients $\boldsymbol{a}^{(k)}$ can be expressed as a weighted sum of the values of $p(\boldsymbol{x}, \boldsymbol{\xi}, t)$ at the respective abscissas of the employed quadrature:

$$\begin{aligned} \boldsymbol{a}^{(k)}(\boldsymbol{x}, t) &= \int_{\mathbb{R}^D} \omega(\boldsymbol{\xi}) p(\boldsymbol{x}, \boldsymbol{\xi}, t)\, \mathrm{d}\boldsymbol{\xi} \quad , \\ &= \sum_{i=0}^{l} w_i p(\boldsymbol{x}, \boldsymbol{e}_i, t) \quad , \\ &= \sum_{i=0}^{l} \frac{w_i}{\omega(\boldsymbol{e}_i)} f_N^{\mathrm{eq}}(\boldsymbol{x}, \boldsymbol{e}_i, t) \boldsymbol{H}^{(k)}(\boldsymbol{e}_i) \quad . \end{aligned} \tag{2.9}$$

Moreover, the discrete distribution $f_{iN}^{\mathrm{eq}}(\boldsymbol{x}, \boldsymbol{e}_i, t)$ completely determine $f_N^{\mathrm{eq}}(\boldsymbol{x}, \boldsymbol{\xi}, t)$ and its first N moments.

To give an example, we start working in one dimension, $D = 1$, and derive a quadrature which ensures the conservation of the first two moments of the equilibrium distribution. For an l-point Gauss-Hermite quadrature with algebraic precision $Q = 2l - 1$, the abscissas x_i are given by the roots of $H^{(l)}$, with corresponding weights

$$w_i = \frac{l!}{\left(l\ H^{(l-1)}(x_i)\right)^2} \quad . \tag{2.10}$$

In our example we have $Q = 5$ and $l = 3$, it follows that the abscissas of the quadrature correspond to the zeros of $H^{(3)}$: $e_1 = 0, e_2 = -\sqrt{3}, e_3 = \sqrt{3}$. The corresponding weights obtained through Eq. 2.10 read: $w_1 = \frac{2}{3}, w_2 = w_3 = \frac{1}{6}$. To ensure perfect streaming it is convenient to scale the abscissas to ensure they fall on grid points of a Cartesian grid. This can be done with a particular choice of the lattice constant c_s. By taking $c_s = 1/\sqrt{3}$ we can redefine the quadrature poles as: $e_1 = 0, e_2 = -1, e_3 = 1$. To conclude, this quadrature allows getting a numerical expression for the zero-th and first moment of the distribution:

$$\begin{aligned} \rho &= \sum_{i=1}^{l} f_i \quad , \\ \rho \boldsymbol{u} &= \sum_{i=1}^{l} f_i \boldsymbol{e}_i \quad . \end{aligned} \tag{2.11}$$

Clearly, to ensure the preservation of energy one would need to recover

also the second moment of the distribution which would simply require to derive the quadrature for $Q = 7$.

Having defined the quadrature it is then possible to derive the discrete expression for the LB equation:

$$f_i(\boldsymbol{x} + \boldsymbol{e}_i\Delta t, \boldsymbol{e}_i, t + \Delta t) - f_i(\boldsymbol{x}, \boldsymbol{e}_i, t) = \frac{\Delta t}{\tau}\left(f_{iN}^{\mathrm{eq}}(\boldsymbol{x}, \boldsymbol{e}_i, t) - f_i(\boldsymbol{x}, \boldsymbol{e}_i, t)\right) \quad , \tag{2.12}$$

where f_{iN}^{eq} represents the discrete truncated Maxwell-Boltzmann distribution function:

$$f_{iN}^{\mathrm{eq}} = w_i\rho\{\underbrace{1 + e_i\boldsymbol{u}}_{\text{1st order}} + \underbrace{\frac{1}{2}\left[(e_i\boldsymbol{u})^2 - \boldsymbol{u}\boldsymbol{u} + (T-1)(e_i^2 - 2)\right]}_{\text{2st order}} + \cdots + \mathcal{O}(N{+}1)\} \tag{2.13}$$

As a final remark it has to be noticed that while the derivation of the quadrature is straightforward in one dimension, it becomes slightly more complicate in two and three dimensions, since there is not a generalized fundamental theorem of Gaussian quadrature for higher dimensions (except for a few rare exceptions). In order to derive quadratures in higher dimensions one possible approach is to rely on the preservation of norm and orthogonality of Hermite polynomial tensors:

$$\int_{\mathbb{R}^D} \omega(\boldsymbol{\xi}) \cdot H^{(j)}(\boldsymbol{\xi}) \cdot H^{(k)}(\boldsymbol{\xi})\, \mathrm{d}\boldsymbol{\xi} = \sum_i w_i \cdot H^{(j)}(\boldsymbol{e}_i) \cdot H^{(k)}(\boldsymbol{e}_i) = \delta_{jk} \quad \forall j, k \quad . \tag{2.14}$$

Given such a system of equations what one operatively does is to follow the so called quadrature with prescribed abscissas [78], where following a combinatorial approach different stencils $\mathcal{V} = \{e_i \in \mathbb{Z}^D : i = 0, \ldots, i_{\max}\}$ are tested and plugged into Eq. 2.14 in an attempt to determine positive-valued weights. The minimal stencil implementing quadratures with a degree of precision up to $Q = 9$ in 1,2 and 3 dimensions have been derived and collected in a series of works by Shan [79, 80].

2.3 Towards a unified lattice kinetic scheme

In this section we detail the derivation of the Relativistic Lattice Boltzmann Method. While the procedure is conceptually the same as the one used in the classical case it will become immediately apparent that achieving Lorentz invariance introduces several complications.

2.3.1 Derivation in D+1 dimensions

In a general $D+1$ formulation the particle distribution function $f(x^\alpha, p^\beta)$ depends on space-time coordinates $(x^\alpha) = (ct, \boldsymbol{x})$ and momenta $(p^\alpha) = (p^0, \boldsymbol{p}) = \left(\sqrt{\boldsymbol{p}^2 + m^2}, \boldsymbol{p}\right)$ with $\boldsymbol{x}$ and $\boldsymbol{p} \in \mathbb{R}^D$. The metric tensor naturally extends to $\eta^{\alpha\beta} = diag(1, -\mathbb{1})$, with $\mathbb{1} = (1, \ldots, 1) \in \mathbb{N}^D$. Here and in what follows we will work in natural units, for which $k_\mathrm{B} = c = 1$.

We start by writing an explicit form of Eq. 1.2, taken in the Anderson-Witting [31, 32] relaxation time approximation (Eq. 1.32):

$$p^0 \partial_t f + p^i \nabla_i f + mK^\alpha \frac{\partial f}{\partial p^\alpha} = \frac{U^\alpha p_\alpha}{\tau}(f^\mathrm{eq} - f) \quad , \tag{2.15}$$

where the external forces acting on the system, K^α, are for simplicity assumed not to depend on the momentum $(D+1)$-vector. The local equilibrium f^eq is given by the Maxwell-Jüttner distribution, already introduced in Chapter 1:

$$f^\mathrm{eq} = A(n, T) \exp\left(-\frac{U^\alpha p_\alpha}{T}\right) \quad , \tag{2.16}$$

where the for derivation of the normalization factor $A(n, T)$, which depends on the dimension D, we follow the procedure described in Section 1.5.

By dividing the left and right hand sides of Eq. 2.15 by p^0, it is possible to cast the relativistic Boltzmann equation in terms of quantities that can be discretized on a regular lattice:

$$\partial_t f + v^i \nabla_i f = \frac{U^\alpha p_\alpha}{\tau p^0}(f^\mathrm{eq} - f) - \frac{mK^\alpha}{p^0}\frac{\partial f}{\partial p^\alpha} \quad , \tag{2.17}$$

with $v^i = p^i/p^0$ the components of the microscopic velocity. In Eq. 2.17 the time-derivative and the propagation term are the same as in the non-relativistic regime; the price to pay is an additional dependence on p^0 of the relaxation (and forcing) term.

The discretization on a lattice of Eq. 2.17 starts from the definition of an expansion of the equilibrium distribution function f^eq in basis of polynomials orthogonal with respect to a weighting function ω, corresponding to f^eq in the fluid rest frame (where $U^i = 0$). It is simple to verify that in the rest frame Eq. 2.16 reduces to

$$\omega(p^0) = \frac{1}{N_R} \exp\left(-p^0/T\right) \quad , \tag{2.18}$$

where N_R is a normalization factor, which deserves a further remark: while

the normalization factor $A(n,T)$ in Eq. 2.16 carries an important physical meaning (as was discussed in Section 1.5), N_R is purely numerical and can be arbitrarily chosen. In most cases we will find it convenient to take the normalization factor N_R such to satisfy the condition $\int \omega(p^0)\,\mathrm{d}\boldsymbol{p}/p^0 = 1$.

Following a Gram-Schmidt procedure one can then derive a set of polynomials $\{J^{(i)}, i = 1, 2\dots\}$, which are used to build the expansion:

$$f^{\mathrm{eq}}((p^\mu),(U^\mu),T) = \omega(p^0)\sum_{k=0}^{\infty} a^{(k)}((U^\mu),T)J^{(k)}((p^\mu)) \quad , \tag{2.19}$$

where $a^{(k)}$ are the projection coefficients defined as

$$a^{(k)}((U^\mu),T) = \int_{\mathbb{R}^D} f^{\mathrm{eq}}((p^\mu),(U^\mu),T)J^{(k)}((p^\mu))\frac{\mathrm{d}\boldsymbol{p}}{p^0} \quad . \tag{2.20}$$

At this stage one can appreciate that the polynomials have been derived such that the coefficients $a^{(k)}$ coincide by construction with the moments of the distribution function, exactly like in the classical case; it follows that we retain the property that $f_N^{\mathrm{eq}}((p^\mu),(U^\mu),T)$, obtained truncating the summation in Eq. 2.19 to N, correctly preserves the moments of the distribution up to the N-th order.

Observe that until now the discussion holds its validity on the continuum. Before going further in details, we introduce non-dimensional quantities defined with respect to a reference temperature T_0: $\bar{T} = T/T_0$, $\bar{m} = m/T_0$, $\bar{p}^\alpha = p^\alpha/T_0$. The role of T_0 should become more clear in Section 2.7, where we discuss the conversion between physics and lattice units.

The discrete formulation is based on a Gauss-type quadrature on a Cartesian grid. In order to ensure that all quadrature points lie on lattice sites and to preserve the moments of a distribution up to a desired order N we need to determine the weights and the abscissas of a quadrature such to satisfy the orthonormal conditions [78]:

$$\int_{\mathbb{R}^D} \omega(\bar{p}^0)J_l((\bar{p}^\mu))J_k((\bar{p}^\mu))\frac{\mathrm{d}\bar{\boldsymbol{p}}}{\bar{p}^0} = \sum_i w_i J_l((\bar{p}_i^\mu))J_k((\bar{p}_i^\mu)) = \delta_{lk} \quad , \tag{2.21}$$

with $(\bar{p}_i^\mu)$ the discrete $(D+1)$ momentum vectors. A convenient parametrization of $(\bar{p}_i^\mu)$ writes as follows:

$$(\bar{p}_i^\mu) = p_i^0(1, v_0 n_i) \quad , \tag{2.22}$$

where $n_i \in \mathbb{Z}^D$ are the vectors forming the stencil $G = \{n_i \mid i =$

$1, 2, \ldots, i_{max}\}$ defined by the (on-lattice) quadrature points, v_0 is a free parameter that can be freely chosen such that $v_i = v_0||n_i|| < 1, \forall i$, and $\bar{p}_i^0$ is defined as

$$\bar{p}_i^0 = \bar{m}\gamma_i = \bar{m}\frac{1}{\sqrt{1-v_i^2}} \quad . \tag{2.23}$$

In order to determine a quadrature we proceed as follows: i) select a numerical value for $\bar{m}$, ii) choose a set of velocity vectors G, formed by a sufficient number of elements such that the left hand side of Eq. 2.21 is a full ranked matrix, iii) look for a solution of Eq. 2.21 formed by non-negative weights ($w_i \geq 0, \forall i$).

Observe that while the parametrization in Eq. 2.22 is general and can be used to determine quadratures for wide ranges of values of $\bar{m}$, the limit case of massless particles requires a slightly different approach. Indeed, for $\bar{m} = 0$ Eq. 2.21 is not well defined; in this case we let $\bar{p}_i^0$ be free parameters (as already suggested in [56]) to be determined such as to satisfy Eq. 2.21. We can have several energy shells associated to each vector and therefore we add a second index to Eq. 2.22:

$$(\bar{p}_{i,j}^{\mu}) = \bar{p}_j^0(1, \frac{n_i}{||n_i||}) \quad , \tag{2.24}$$

where the index j labels different energy shells, and it is clear that $||n_i||$ has to be the same for all the stencil vectors since all the particles travel at the same speed $v_i = c = 1, \forall i$.

Once a quadrature is defined it is possible to write the discretized version of the equilibrium distribution as follows:

$$f_{iN}^{\text{eq}}((\bar{p}^{\mu}), (U^{\mu}), \bar{T}) = w_i \sum_{k=0}^{N} a^{(k)}((U^{\mu}), \bar{T}) J^{(k)}((\bar{p}_i^{\mu})) \quad . \tag{2.25}$$

To conclude, we can finally write down the discrete relativistic Boltzmann equation:

$$f_i(\boldsymbol{x} + v^i\Delta t, t + \Delta t) - f_i(\boldsymbol{x}, t) = \Delta t \, \frac{\bar{p}_i^{\alpha} U_{\alpha}}{\bar{p}^0 \tau}(f_i^{\text{eq}} - f_i) + F_i^{\text{ext}} \quad , \tag{2.26}$$

where F_i^{ext} is the discretization of the total external forces acting on the system, more details will be given in Section 2.5.

Observe that in Eq. 2.26 we ensure that $\boldsymbol{x} + v^i\Delta t$ always lies on lattice sites by asking:

$$v_0 n_i \Delta t = N_i \Delta x \quad , \tag{2.27}$$

where Δx is the lattice spacing and $N_i \in \mathbb{Z}^D$. This in turn gives the following relation between time and space units on the lattice:

$$v_0 = \frac{\Delta x}{\Delta t} \quad , \tag{2.28}$$

which will be useful in Section 2.7 where we detail the conversion from physics to lattice units.

In the next sections we give details on the two most relevant steps in the derivation of the method, the polynomial expansion of the equilibrium distribution and the Gaussian quadrature.

2.3.2 Polynomial expansion of the distribution function at equilibrium

In this section we detail the polynomial expansion of the Maxwell-Jüttner distribution (Eq. 2.19) in $(D+1)$-dimensions, with $D = 3, 2, 1$. We start by taking into consideration the $(2+1)$ dimensional case, since it is simpler to handle analytically with respect to the other two cases.

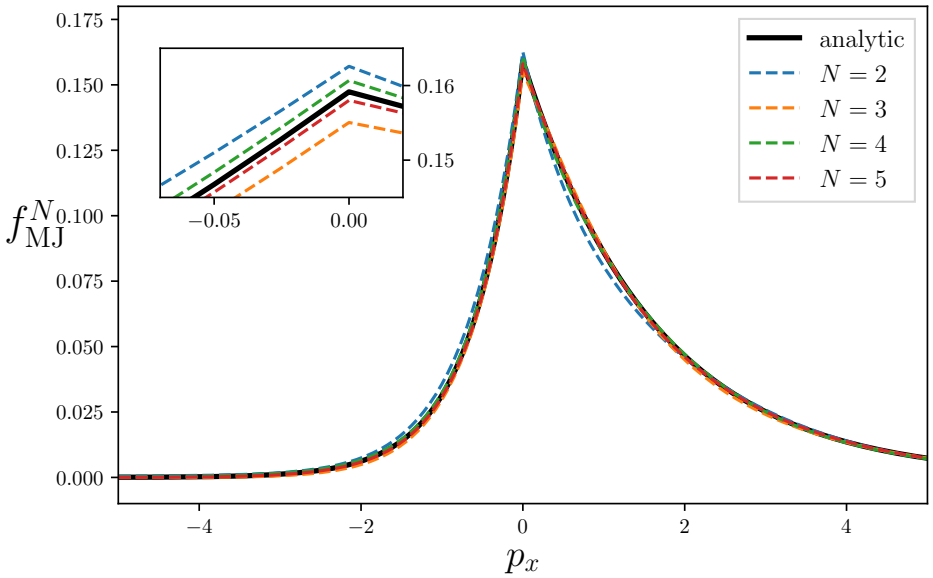

Figure 2.1: *Comparison of the analytic Maxwell Jüttner distribution in $(2+1)$ dimensions against approximations at various orders N, computed using an orthogonal polynomial basis. The distributions are shown as functions of $\boldsymbol{p} = (p_x, 0)$, having fixed all the other parameters to $m = 0$, $T = 1$, $n = 1$ and $\beta = |U^i|/U^0 = 0.5$.*

Starting from the weighting function

$$\omega(\bar{p}^0) = \frac{1}{1+\bar{m}} \exp\left(-\bar{p}^0\right) \quad , \tag{2.29}$$

we use a Gram-Schmidt procedure to derive the polynomials, and consequently the corresponding projections, required to define the expansion of the equilibrium distribution up to a desired order. In Appendix B and D we list all polynomials and projections required to derive the second order approximation of the equilibrium distribution:

$$\begin{aligned}
f^{\mathrm{eq}} = n\omega(\bar{p}^0)\Big(&\frac{1}{4(\bar{m}(\bar{m}+3)+3)(\bar{m}+\bar{T})}\left((U^x)^2(\bar{m}^2+3\bar{m}\bar{T}+3\bar{T}^2)\right.\\
&\times((\bar{m}+1)(\bar{m}+2)(\bar{p}^0)^2 - 2\bar{m}(\bar{m}(\bar{m}+5)+9)\bar{p}^0 + \bar{m}(\bar{m}+3)(\bar{m}(\bar{m}+4)\\
&\left.+6)+2(-6\bar{p}^0+(\bar{p}^x)^2+3))\right) + U^0\Big(-\frac{1}{2}(\bar{m}+2)(\bar{m}^2-2(\bar{m}+2)\bar{p}^0\\
&+4\bar{m}+(\bar{p}^0)^2+2) - \frac{1}{(2\bar{m}(\bar{m}+3)+3)(\bar{m}+\bar{T})}\\
&\times(\bar{p}^xU^x+\bar{p}^yU^y)(\bar{m}^2-(\bar{m}+1)\bar{p}^0+3\bar{m}+3)(\bar{m}^2+3\bar{m}\bar{T}+3\bar{T}^2)\\
&-\bar{m}+\bar{p}^0-1) + \frac{1}{\bar{m}+\bar{T}}\left(\frac{1}{2}(\bar{m}^2-2(\bar{m}+2)\bar{p}^0+4\bar{m}+(\bar{p}^0)^2+2)\right.\\
&\left.\times(\bar{m}\bar{T}+(\bar{m}+1)^2+\bar{T}^2)+(\bar{m}+1)(\bar{m}-\bar{p}^0+1)+1\right)\\
&+U^x\Big(\frac{\bar{p}^x\bar{p}^yU^y(\bar{m}^2+3\bar{m}\bar{T}+3\bar{T}^2)}{(\bar{m}(\bar{m}+3)+3)(\bar{m}+\bar{T})} + \frac{\bar{p}^x}{2\bar{m}(\bar{m}+3)+3}\left((\bar{m}^3+5\bar{m}^2\right.\\
&\left.-(\bar{m}(\bar{m}+3)+3)\bar{p}^0+12\bar{m}+12)\right)\Big) + \frac{\bar{p}^yU^y}{2\bar{m}(\bar{m}+3)+3}\left((\bar{m}^3+5\bar{m}^2\right.\\
&\left.-(\bar{m}(\bar{m}+3)+3)\bar{p}^0+12\bar{m}+12)\right) + \frac{(U^y)^2(\bar{m}^2+3\bar{m}\bar{T}+3\bar{T}^2)}{4(\bar{m}(\bar{m}+3)+3)(\bar{m}+\bar{T})}\\
&\times(\bar{m}^4+\bar{m}^3(7-2\bar{p}^0)+\bar{m}^2(\bar{p}^0-8)(\bar{p}^0-2)+3\bar{m}((\bar{p}^0-6)\bar{p}^0+6)\\
&+4(\bar{p}^0-3)\bar{p}^0-2(\bar{p}^x)^2+6)) \quad .
\end{aligned}$$

The expression in the ultra-relativistic limit is slightly simpler:

$$\begin{aligned}
f^{\mathrm{eq}} = n\omega(\bar{p}^0)\Big(&\frac{1}{2}\bar{T}(U^x)^2((\bar{p}^0-6)\bar{p}^0+(\bar{p}^x)^2+3) + \frac{1}{2}\bar{T}(U^y)^2(2(\bar{p}^0-3)\bar{p}^0\\
&-(\bar{p}^x)^2+3) + U^0((\bar{p}^0-3)\bar{p}^x\bar{T}U^x + (\bar{p}^0-3)\bar{p}^y\bar{T}U^y - (\bar{p}^0-5)\bar{p}^0-3)\\
&+U^x(\bar{p}^x\bar{p}^y\bar{T}U^y - (\bar{p}^0-4)\bar{p}^x) - (\bar{p}^0-4)\bar{p}^yU^y\\
&+\frac{1}{2\bar{T}}(\bar{p}^0((\bar{p}^0-4)\bar{T}^2+\bar{p}^0-6)+\bar{T}^2+3)) \quad .
\end{aligned}$$

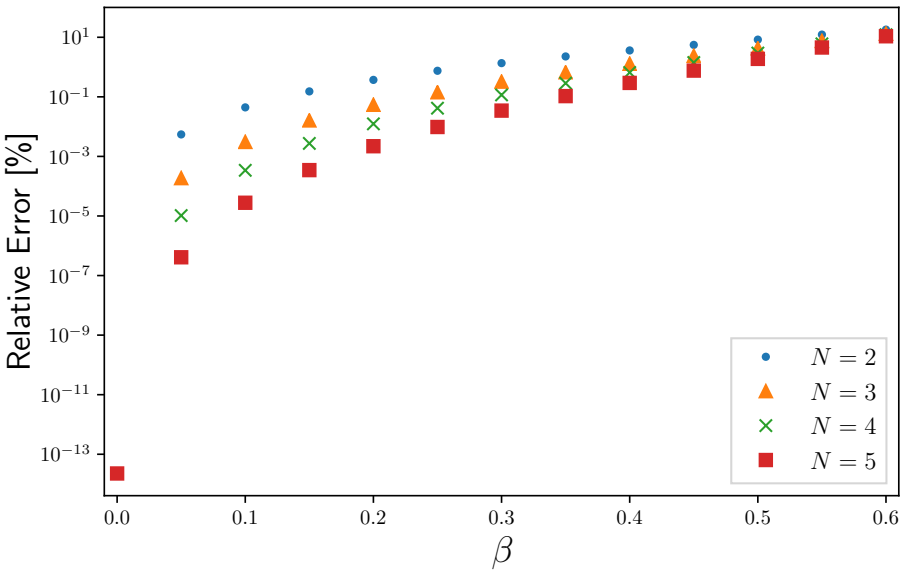

Figure 2.2: *Relative error between the analytic Maxwell Jüttner distribution in (2+1) dimensions and approximations at various orders N, computed using an orthogonal polynomial basis. The error is computed using the L2-norm evaluating the distributions at $\boldsymbol{p} = (p_x, 0)$, $-10 < p_x < 10$, with $m = 0$, $T = 1$, $n = 1$ and for several values of $\beta = |U^i|/U^0$.*

Expressions at higher orders are rather bulky and are therefore given as supplementary material [81]. In Fig. 2.1 we compare the expressions for the ultra-relativistic limit up to the fifth-order against the analytical form of the distribution function. The distributions are shown as functions of $\boldsymbol{p} = (p_x, 0)$, having fixed the (numerical) values for the particle number n and temperature T to unity, and with $\beta = |U^i|/U^0 = 0.5$. In order to give a more quantitative comparison between the different order of the expansions of the equilibrium distribution, in Fig. 2.2 we show the relative error as a function of β. It is clear that one expects better accuracy in the proximity of the expansion origin ($\beta = 0$), and on the other hand larger deviations as β is increased. This trend is shown in Fig. 2.2, where it can be seen that in the massless limit, and with a fifth-order expansion, the relative percentage error stays within 1% up until $\beta \sim 0.4$. Differences in the accuracy of the various expansion orders are more pronounced at small values of β.

An interesting feature of the expansions of the equilibrium distribution is that the quality of the approximation does not depend just on the proximity to the expansion origin (with respect to β), but also on the

numerical value of $\bar{m}$. To highlight this aspect in Fig. 2.3 we show a heat-map of the relative error using a third order expansion as a function of both ζ and β. Here one can appreciate that for a fixed value of β, the error tends to increase as we increase ζ. In a sense, the expansion naturally embeds the fact that at low temperatures ($\zeta \gg 1$) the observation of fluids at very large values of β would be rather unphysical.

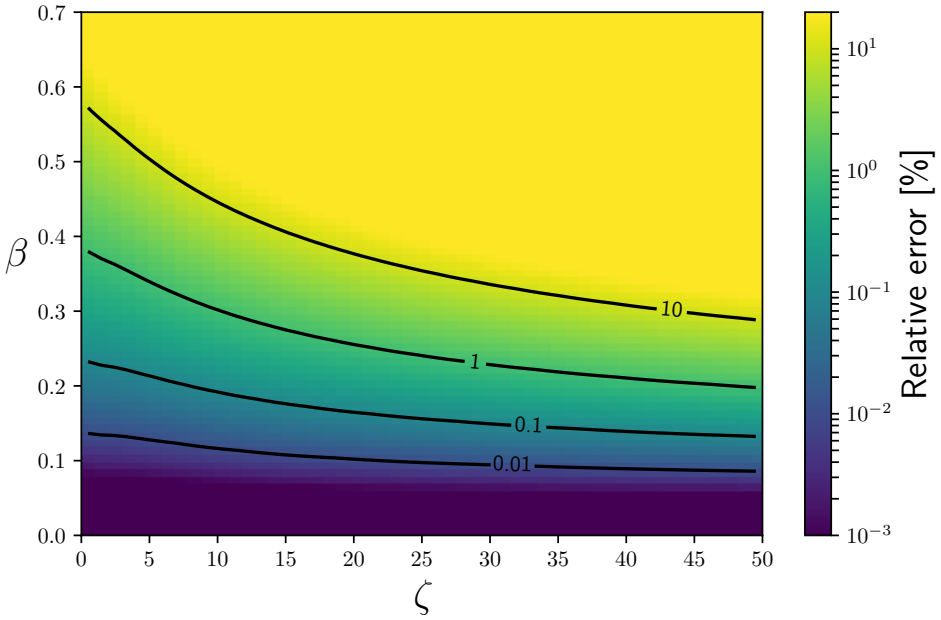

Figure 2.3: *Relative error between the analytic Maxwell Jüttner distribution in (2+1) dimensions and approximations at various orders N, computed using an orthogonal polynomial basis. The error is computed using the L2-norm evaluating the distributions at $\boldsymbol{p} = (p_x, 0)$, $-10 < p_x < 10$, with $n = 1$, $\beta = |U^i|/U^0 = 0.4$ and for several values of ζ.*

The analysis presented in Fig. 2.1, 2.2 and 2.3, can be repeated in (3+1) and (1+1) dimensions, giving results qualitatively similar to those reported above. The expressions of the second order polynomial expansion of the equilibrium distribution in $(3+1)$ and $(1+1)$ dimensions are reported in the supplementary material [81]. Note that the massless limit in $(1+1)$ dimensions need special care. While in $(3+1)$ and $(2+1)$ dimensions one can derive the massless limit by calculating separately the limit for $\bar{m} \to 0$ of the polynomials and of the projections, to then use Eq. 2.19 to derive the result, this is not possible in the $(1+1)$ dimensional case. Indeed one can verify that the massless limit of polynomials and projections is divergent. On the other hand the limit of the product of each polynomial with its

correspondent projection is convergent. By using:

$$f_N^{\mathrm{eq}}((\bar{p}^\mu),(U^\mu),\bar{T}) = \omega(\bar{p}^0)\sum_{k=0}^{N}\lim_{\bar{m}\to 0}\left(a^{(k)}((U^\mu),\bar{T})J^{(k)}((\bar{p}_i^\mu))\right) \quad , \quad (2.30)$$

one can derive the expression, here reported up to second order:

$$\begin{aligned}
f^{\mathrm{eq}} &= \frac{\omega(\bar{p}_0)}{2\bar{T}}\left[1+\bar{p}_0(U_0-1)+\bar{p}_xU_x\right.\\
&+(\bar{p}_0-2)\bar{p}_x\bar{T}U_x(\bar{T}U_0-1)-\frac{1}{2}\left(2\bar{p}_0-\bar{p}_x^2\right)\left(\bar{T}^2\left(2U_x^2+1\right)-2\bar{T}U_0+1\right)\\
&+\left(\frac{1}{6}\bar{p}_x\bar{T}U_x\left(-6\bar{p}_0+\bar{p}_x^2+6\right)\left(\bar{T}^2\left(4U_x^2+3\right)-6\bar{T}U_0+3\right)\right)\\
&\left.+\frac{1}{6}\left(\bar{p}_0\left(\bar{p}_x^2+6\right)-6\bar{p}_x^2\right)\left(\bar{T}^3\left(4U_0U_x^2+U_0\right)-3\bar{T}^2\left(2U_x^2+1\right)+3\bar{T}U_0-1\right)\right]
\end{aligned}$$

As we will see in the next section, the fact that polynomials and projections do not have a finite limit in the massless case have implications on the definition of Gaussian quadratures.

2.3.3 Gauss-type quadratures with prescribed abscissa

In this section we provide details on the definition of Gauss-type quadratures used for the discretization of the relativistic Boltzmann equation. We start once again from the $(2+1)$ dimensional case. In order to implement a RLBM on a Cartesian space-filling lattice we need to find the weights and the abscissas of a quadrature satisfying the following orthonormal condition:

$$\int_{\mathbb{R}^2}\omega(\bar{p}^0)J^{(l)}((\bar{p}^\mu))J^{(k)}((\bar{p}^\mu))\frac{d^2\bar{p}}{\bar{p}^0} = \sum_{i=1}^{K} w_i\ J^{(l)}((\bar{p}_i^\mu))J^{(k)}((\bar{p}_i^\mu)) = \delta_{lk} \quad , \quad (2.31)$$

with $\{J^{(i)}, i=1,2\ldots K\}$ the orthogonal polynomials (see Appendix B), $(\bar{p}_i^\mu)$ the three-momentum vectors following the parametrization in Eq. 2.22 and w_i suitable weights.

We follow the procedure described in [79], building a stencil by adding as many symmetric groups as necessary to match the number of linearly independent components of Eq. 2.31. For example, considering quadratures giving a second-order approximation, the system of Eqs. 2.31 has 6 linearly independent components, so one needs to build a stencil with (at least) 6 different symmetric groups. Likewise, at third order there are 10 indepen-

dent components, so we need 10 groups. Yet higher order approximations would require stencils with even larger numbers of groups.

Recall that the discrete momentum vectors ($\bar{p}_i^{\mu}$) depend on the stencil vector n_i and a common arbitrary value for v_0. Therefore, having selected a numerical value for the rest mass $\bar{m}$, and a stencil $G = \{n_i \mid i = 1, 2, \ldots, i_{max}\}$, Eq. 2.31 leads to a linear system of equations, parametric on v_0:

$$A(v_0)\boldsymbol{w} = \boldsymbol{b} \quad . \tag{2.32}$$

Here A is a $l \times k$ matrix (l being the number of possible combinations of the orthogonal polynomials, k the number of groups forming the stencil), $\boldsymbol{b}$ is a known binary vector, and $\boldsymbol{w}$ is the vector of unknowns. Since the Gaussian quadrature requires strictly positive weights in order to guarantee numerical stability, we need to select values of v_0 (if they exist) such that $w_i > 0 \ \forall i$. For low-order approximations it is possible to compute an analytic solution, writing each weight w_i as an explicit function of the free parameter v_0, but this become quickly very hard and, already at the second-order, numerical solutions are necessary. A possible formulation of the problem writes as follows:

$$\begin{aligned} \min \begin{bmatrix} -\boldsymbol{c}_1 \\ \boldsymbol{c}_2 \end{bmatrix}^T \begin{bmatrix} \boldsymbol{w}^- \\ \boldsymbol{w}^+ \end{bmatrix} \quad & , \\ s.t.\ A(v_0)\boldsymbol{w} = \boldsymbol{b} \quad & , \\ 0 < v_0 \leq v_{\max} \quad & . \end{aligned} \tag{2.33}$$

where the vector of unknowns $\boldsymbol{w}$ has been split into two sub vectors, respectively $\boldsymbol{w}^+$ formed by its nonnegative components, and $\boldsymbol{w}^-$ accounting the negative components. Vectors $\boldsymbol{c}_1$ and $\boldsymbol{c}_2$ are all-ones vectors matching the dimensions of $\boldsymbol{w}^-$ and $\boldsymbol{w}^+$. We also assume that $A(v_0)$ is a fully-ranked matrix. This can be achieved applying a pre-processing phase where redundant rows are removed, for example by applying a QR or LU factorization. Note that an implicit constrain on $\boldsymbol{w}$ is given by normalization factor chosen for the weighting function $\omega(\bar{p}^0)$. For example, having normalized $\omega(\bar{p}^0)$ under the condition $\int \omega(\bar{p}^0)\, \mathrm{d}^2\bar{\boldsymbol{p}}/\bar{p}^0 = 1$, it follows directly from Eq. 2.31 that:

$$\sum_i w_i = 1 \quad . \tag{2.34}$$

Observe that in Eq. 2.33 we have not constrained $\boldsymbol{w}$ to be nonnegative. By allowing nonnegative values for $\boldsymbol{w}$, it is simpler to find solutions for

Eq. 2.33 using, for example, a line search method to scan the feasible region spanned by the admissible values for v_0. Each solution of the minimization procedure is then accepted only in the case $w_i \geq 0 \ \forall i$, as this requirement improves numerical stability and is consistent with a (pseudo-)particle interpretation of the RLBM.

In general, many different solutions to the quadrature problem exist. We have performed a detailed exploration of the available phase-space, implementing a solver for Eq. 2.33 based on the *LAPACK* library with several instances running in parallel on a cluster of CPUs. The solver takes as input a stencil G and tries to find a solution for Eq. 2.33 by scanning several values of v_0 with a simple line search strategy. This fast method allows to scan several stencils at different values of $\bar{m}$; on the other hand, more robust techniques are desirable in order to perform a more systematic exploration of the phase-space.

To give an example, we look for a second order quadrature at $\bar{m} = 5$ using the stencil $G = \{(0,0) \bigcup (\pm 1, 0)_{\mathtt{FS}} \bigcup (\pm 1, \pm 1)_{\mathtt{FS}} \bigcup (\pm 2, 0)_{\mathtt{FS}} \bigcup (\pm 2, \pm 1)_{\mathtt{FS}} \bigcup (\pm 2, \pm 2)_{\mathtt{FS}}\}$, where FS stands for full-symmetric. With this stencil, the longest displacement is given by the set of vectors with lenght $2\sqrt{2}$, and therefore the range of validity of the parameter v_0 is $0 < v_0 < 1/(2\sqrt{2})$ (this is due to the requirement $v_0 ||n_i|| \leq 1, \forall i$, used in the definition of discrete momentum vectors in Eq. 2.22). A visual representation of the solution for Eq. 2.33 is given in Fig. 2.4a, with the minimum found at $v_0 \sim 0.3005$; in this case we cannot determine a solution for which all the weights of the quadrature are positive. We then consider a different stencil $G = \{(0,0) \bigcup (\pm 1, 0)_{\mathtt{FS}} \bigcup (\pm 1, \pm 1)_{\mathtt{FS}} \bigcup (\pm 2, \pm 1)_{\mathtt{FS}} \bigcup (\pm 2, \pm 2)_{\mathtt{FS}} \bigcup (\pm 3, \pm 1)_{\mathtt{FS}}\}$. This time, the range of validity of the parameter v_0 is $0 < v_0 < 1/\sqrt{10}$). From Fig. 2.4b we can observe that there is a small range of values of v_0 where all the weights take nonnegative values. Taking for example $v_0 = 0.2726$ the corresponding weights for the quadrature are:

$$
\begin{aligned}
w_1 &= 0.2938928682119484 \ , \quad & w_2 &= 0.00136644441345044 \ , \\
w_3 &= 0.0212650236700010 \ , \quad & w_4 &= 0.07032872215612153 \ , \\
w_5 &= 0.0036974948602444 \ , \quad & w_6 &= 0.00477018784553696 \ .
\end{aligned}
$$

Particularly convenient values of v_0 are those located at the boundaries of the orange colored interval in Fig. 2.4b, since some weights become zero thus allowing the pruning of certain lattice velocities. In our example one can reduce the full set of 29 velocities to 25 by setting either w_2 to zero (with $v_0 = 0.27259285465\ldots$), or w_3 to zero ($v_0 = 0.27278322823\ldots$).

Figure 2.4: *Parametric solution of the system of equations given by Eq. 2.31, having chosen $\bar{m} = 5$. The left panel makes use of the stencil $G = \{(0,0) \bigcup (\pm 1, 0)_{FS} \bigcup (\pm 1, \pm 1)_{FS} \bigcup (\pm 2, 0)_{FS} \bigcup (\pm 2, \pm 1)_{FS} \bigcup (\pm 2, \pm 2)_{FS}\}$. The panel on the right was obtained using the stencil $G = \{(0,0) \bigcup (\pm 1, 0)_{FS} \bigcup (\pm 1, \pm 1)_{FS} \bigcup (\pm 2, \pm 1)_{FS} \bigcup (\pm 2, \pm 2)_{FS} \bigcup (\pm 3, \pm 1)_{FS}\}$. In this second case we can identify a region for which $w_i(v_0) \geq 0 \; \forall i$ (orange colored interval), giving a set of solutions that can be used to build a numerically stable quadrature.*

Typically, for a given value of $\bar{m}$ several different stencils are possible; however, each stencil works correctly only in a certain range of $\bar{m}$. Still, a reasonably small set of stencils allows to treat $\bar{m} \geq 0.5$ at the second order and $\bar{m} \geq 1.2$ at the third order, offering the possibility to cover a very large kinematic regime, from almost ultra-relativistic to non-relativistic. A graphical view of (a subset) of all stencils that we have identified is reported in Appendix E, for both 2-nd and 3-rd order.

In general, the process of finding quadratures becomes harder and harder as the order is increased and as $\bar{m}$ takes smaller and smaller values. The reason for this, from a strictly mathematical point of view, is that for small values of $\bar{m}$ the condition number of the system matrix in Eq. 2.33 takes large values, therefore requiring more advanced linear algebra techniques. From a physical point of view the reason why this is a difficult problem, is that for $\bar{m} \to 0$ the pseudo-particles tends to move all with similar velocity close to the speed of lights, making it difficult to satisfy the constraint that all particles travel in one time step at different distances, hopping from a point of the grid to another point of the grid.

For the limiting case where $\bar{m} \to 0$ this translates in restricting to

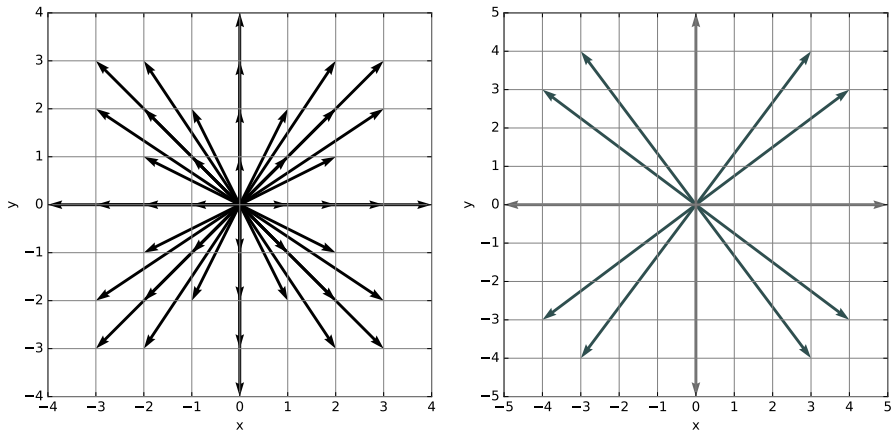

Figure 2.5: *Two examples of stencil compatible with a third order quadrature, respectively for $\bar{m} = 5$ (left) and $\bar{m} = 0$ (right). The points forming the stencil for $\bar{m} = 0$ lie on the intersection between the Cartesian grid and a circle of radius 5.*

stencils whose elements sit at the intersection between a Cartesian grid and a circle of given radius. Incidentally this turns out to be the simplest case, since we can introduce the parametrization presented in Eq. 2.24, where following [56] we associate several energy shells to each momentum vector. We remark that this is possible in the ultra-relativistic regime as velocity does not depend on energy, and cannot be used if $\bar{m} \neq 0$. To give an example, we consider a second order quadrature rule for $\bar{m} = 0$ and solve Eq. 2.31 by taking the stencil $G = \{(\pm 3, \pm 4)_{\mathtt{FS}}, (\pm 5, 0)_{\mathtt{FS}}\}$ (Fig. 2.5b) and the parametrization in Eq. 2.24 where three different energy shells get associated to each momentum vector. The solution reads as follows:

$$\begin{aligned}
&\bar{p}_1^0 = 0.41577455678\ldots \; w_{11} = 0 && w_{21} = 0.08888662624\ldots \\
&\bar{p}_2^0 = 2.29428036027\ldots \; w_{12} = 0 && w_{22} = 0.03481471669\ldots \\
&\bar{p}_3^0 = 6.28994508293\ldots \; w_{13} = 0.00175356541\ldots && w_{23} = 0.00042187435\ldots
\end{aligned}$$

The procedure can be iterated at higher orders, although already at order 4 one needs to employ stencils with vectors of length $5\sqrt{13}$, which is impractical from a computational point of view since implies using very large grids to achieve an adequate spacial resolution; things become even more problematic in $(3+1)$ dimensions. It is apparent that higher orders necessarily require off-lattice schemes, which drastically improve the spacial resolution of the grid, but have as drawbacks the need for interpolation and

the introduction of artificial dissipation effects [57, 62]. In Appendix E we provide quadratures up to order 5 in $(3+1), (2+1)$ and $(1+1)$ dimensions space.

Although it can be most likely regarded just as a mere academic exercise, the $(1+1)$ dimensional case is nevertheless worth mentioning. Indeed, as already remarked in the previous section, in this case the massless limit of both polynomials and projections diverges. It follows that we cannot derive the quadrature through Eq. 2.31. However, we can exploit the fact that it is still possible to obtain an expression for the expansion of the equilibrium distribution using Eq. 2.30. We can then express the quadrature problem via the following system of equations:

$$\int_{\mathbb{R}} f^{\mathrm{eq}}((\bar{p}^{\alpha}), (U^{\alpha}), \bar{T}) \bar{p}^{\alpha} \dots \bar{p}^{\omega} \frac{\mathrm{d}\bar{p}}{\bar{p}^{0}} = \sum_{i} \sum_{j} w_{ij} f_{N}^{\mathrm{eq}}((\bar{p}_{ij}^{\alpha}), (U^{\alpha}), \bar{T}) \bar{p}_{ij}^{\alpha} \dots \bar{p}_{ij}^{\omega}, \tag{2.35}$$

where we explicitly require the preservation of all the moments of the distribution up to a desired order N. Quadratures up to fifth order are reported in Appendix E.

2.4 Transport coefficients

The transport coefficients of the model, i.e. shear and bulk viscosities and thermal conductivity, are defined from the non-equilibrium contributions of the energy-momentum tensor [8]. The shear viscosity can be obtained by using the following expression,

$$2\eta \, \partial^{<\alpha} U^{\beta>} = \left(\Delta_{\gamma}^{\alpha} \Delta_{\delta}^{\beta} - \frac{1}{3} \Delta^{\alpha\beta} \Delta_{\gamma\delta} \right) T^{\gamma\delta} \quad , \tag{2.36}$$

where $\Delta^{\alpha\beta} \equiv \eta^{\alpha\beta} - U^{\alpha} U^{\beta}$, and the expression $\partial^{<\alpha} U^{\beta>}$ stands for

$$\partial^{<\alpha} U^{\beta>} = \left[\frac{1}{2} \left(\Delta_{\gamma}^{\alpha} \Delta_{\delta}^{\beta} + \Delta_{\delta}^{\alpha} \Delta_{\gamma}^{\beta} \right) - \frac{1}{3} \Delta^{\alpha\beta} \Delta_{\gamma\delta} \right] \partial^{\gamma} U^{\delta} \quad . \tag{2.37}$$

The bulk viscosity μ, on the other hand, can be calculated by using

$$-\mu \, \partial_{\alpha} U^{\alpha} = -P - \frac{1}{3} \Delta_{\alpha\beta} T^{\alpha\beta} \quad , \tag{2.38}$$

and finally, the thermal conductivity λ, with the expression

$$\lambda \left(\partial^\alpha T - T U^\beta \partial_\beta U^\alpha \right) = \Delta^\alpha_\gamma U_\beta T^{\beta\gamma} \quad . \tag{2.39}$$

However, as already introduced in Section 1.4, and unlike the non-relativistic case, there is no straightforward way to compute the transport coefficients directly from the model parameters. In non-relativistic regimes, both Grad's moments method [33] and the Chapman-Enskog (CE) [34] approach, manage to connect kinetic theory and hydrodynamics in a consistent way, i.e. they provide the same transport coefficients. The two procedure however deliver (slightly) different results when working in relativistic regime [8].

Recent works [24, 39–45, 82, 83], based on different, if not conflicting assumptions, seem to converge towards the results provided by the CE approach. Conceptual shortcomings of the moments method, which have recently been highlighted also in the non-relativistic framework [35–38], revolve around the use of second-order spatial derivatives in constitutive hydrodynamical equations [39]. On the other hand, objections to the relativistic Chapman-Enskog expansion point to its link to relativistic Navier-Stokes equations, which suffer of basic problems, such as broken causality and resulting instabilities [24, 40].

In this section we describe the procedure that we have devised to measure the transport coefficient from simulations. We consider Taylor-Green vortex [84], a well known example of a non-relativistic decaying flow featuring an exact solution of the Navier-Stokes equations, and derive an approximate solution in the mildly relativistic regime. In the non-relativistic case, from the following initial conditions in a 2D periodic domain:

$$\begin{aligned} u_x(x, y, 0) = &\quad u_0 \cos(x) \sin(y), \\ u_y(x, y, 0) = &-u_0 \cos(y) \sin(x), \quad x, y \in [0, 2\pi] \end{aligned} \tag{2.40}$$

the solution is given by

$$\begin{aligned} u_x(x, y, t) = &\quad u_0 \cos(x) \sin(y) F(t), \\ u_y(x, y, t) = &-u_0 \cos(y) \sin(x) F(t), \quad x, y \in [0, 2\pi] \end{aligned} \tag{2.41}$$

with

$$F(t) = \exp(-2\nu\, t) \quad , \tag{2.42}$$

where ν is the kinematic viscosity of the fluid.

In the relativistic case, we need to solve the conservation equations

(Eq. 1.11). We consider a system with a constant initial particle density, and assume that density remains constant. We will verify later this assumption with our numerical results showing that, even though particle density fluctuates in time, the variation is very small. In this case the first equation in Eq. 1.11 is directly satisfied and the expression of the second order tensor slightly simplifies, since $\nabla_\alpha U^\alpha = 0$, and therefore $\varpi = 0$. Consequently, we drop the term depending on the bulk viscosity and rewrite the second order tensor as:

$$T^{\alpha\beta} = -Pg^{\alpha\beta} + (\epsilon + P)U^\alpha U^\beta + \pi^{<\alpha\beta>} \quad . \tag{2.43}$$

We consider the same initial conditions as in Eq. 2.40, and look for a solution in the form of Eq. 2.41, with an appropriate function $F_R(t)$ replacing $F(t)$. We plug Eq. 2.41 in Eq. 2.43 and derive bulky analytic expressions for the derivatives of the second order tensor.

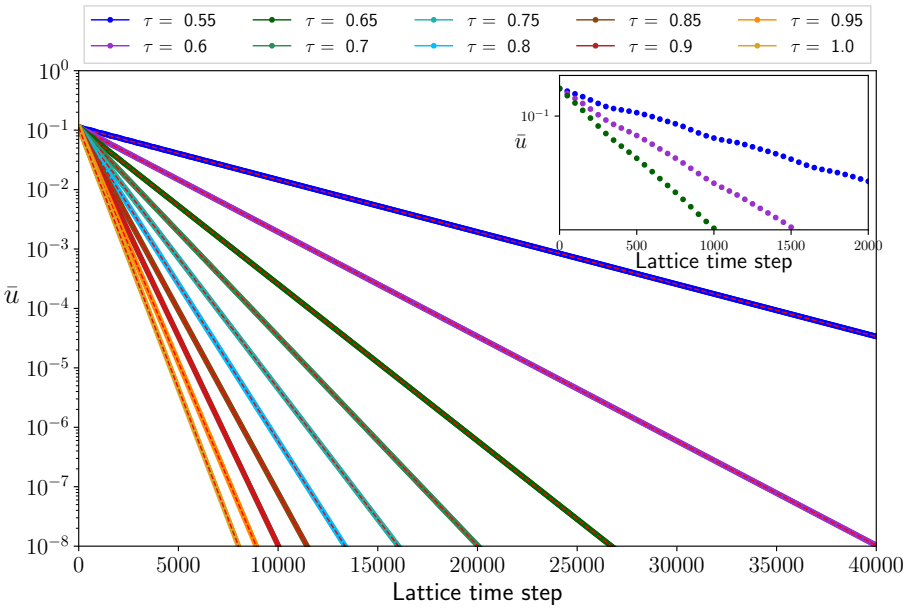

Figure 2.6: *Simulated time evolution of $\bar{u}$ for selected τ values on a $L = 400$ square lattice ($\zeta = 0$, $u_0 = 0.2$, $n = 1$, $T = 1$). Dashed lines are fits to the exponential decay predicted by Eq. 2.45. The inset shows non-linear effects in the early phases of the flow.*

A linear expansion of these expressions in terms of u_0 yields a much simpler expression for $\partial_\beta T^{\alpha\beta}$, leading to the differential equation

$$2\eta F_R(t) + (P + \epsilon)F_R^{'}(t) = 0 \quad . \tag{2.44}$$

	$k\ f(\zeta)$						
τ	$\zeta = 0$	$\zeta = 1.6$	$\zeta = 2$	$\zeta = 3$	$\zeta = 4$	$\zeta = 5$	$\zeta = 10$
0.600	0.8003	0.8319	0.8448	0.8587	0.8892	0.8994	0.9311
0.700	0.8002	0.8318	0.8447	0.8584	0.8888	0.8990	0.9302
0.800	0.8002	0.8318	0.8447	0.8583	0.8887	0.8989	0.9300
0.900	0.8002	0.8318	0.8447	0.8583	0.8887	0.8988	0.9299
1.000	0.8002	0.8317	0.8446	0.8582	0.8887	0.8988	0.9299

Table 2.1: *Selected sample values for the estimate of the parameter $k\ f(\zeta)$ for several values of τ and ζ. Statistical errors for all entries are smaller than 1 in the last displayed digit.*

Assuming $P + \epsilon$ constant, for a fixed value of ζ, we derive an explicit solution:

$$F_R(t) = \exp\left(-\frac{2\eta}{P+\epsilon}t\right)F_R(0) \quad , \tag{2.45}$$

depending on just one transport coefficient, the shear viscosity η. Observe that while the quantity $P + \epsilon$ exhibits some time variation (as found in the simulations) due to the evolution of the local temperature, such fluctuations were found to be negligible.

Next, we compare this analytical solution with data obtained via RLBM numerical simulations, aiming at linking η to the relaxation time τ. We perform several simulations of the Taylor-Green vortex, with different values of the initial speed u_0 and the mesoscopic parameters, τ and ζ.

We consider small (yet, not negligible) values of u_0 and a very broad range of ζ values, smoothly bridging between ultra-relativistic to near non-relativistic regimes. To this end, it is expedient to introduce the observable $\bar{u}$, defined as:

$$\bar{u}^2 = \int_0^{2\pi}\int_0^{2\pi} \left(u_x^2 + u_y^2\right) \mathrm{d}x\, \mathrm{d}y \quad , \tag{2.46}$$

which is directly proportional to $F_R(t)$. Fig. 2.6 is an example of our numerical results, for several values of the mesoscopic parameters, showing the time evolution of $\bar{u}$, and clearly exhibiting an exponential decay.

For each set of mesoscopic values, we perform a linear fit of $\log(\bar{u})$ extracting a corresponding value for η via Eq. 2.45. We next assume a dependence of η on the mesoscopic parameters, which, on dimensional grounds, reads as

$$\eta = k\ f\left(\zeta\right)\ P\ \left(\tau - \frac{1}{2}\right) \quad , \tag{2.47}$$

where $f(\zeta)$ is normalized such that $f(0) = 1$, and the $1/2$ shift in the relaxation time is a lattice correction. The numerical value of k and the

specific functional form of $f(\zeta)$ contain the physical information on the relation between kinetic and hydrodynamics coefficients. For instance, CE predicts $k = 4/5$ and an expression for $f(\zeta)$ to which we shall return shortly; for comparison, Grad's method predicts $k = 2/3$ and a different functional dependence on ζ. We are now able to test that Eq. 2.47 holds correctly, checking that all measurements of $\eta(\tau)$ at a fixed value of ζ yield a constant value for k $f(\zeta)$. One immediately sees from the second column

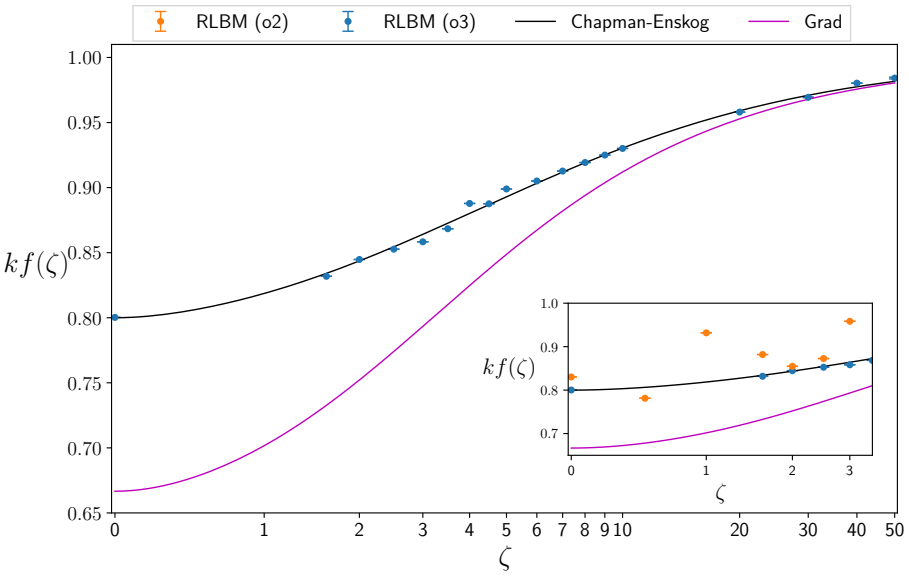

Figure 2.7: *Measured value k $f(\zeta)$ as a function of ζ. The black (magenta) lines are analytic results of the Chapman Enskog (Grad's) methods for the relativistic Boltzmann equation. To improve resolution at small ζ values, we map $\zeta \to \log\left(\zeta + \sqrt{1+\zeta^2}\right)$ on the x-axis. The inset shows clearly that second order quadratures are not sufficient to provide accurate measurements of the shear viscosity.*

of Tab. 2.1 that $k = 4/5$ to very high accuracy, consistently with previous results [24, 39, 47, 85]. More interesting is the assessment of the functional behavior of $f(\zeta)$. The CE expansion predicts [8]

$$f(\zeta) = \frac{\zeta^3}{12}\left(\frac{3}{\zeta^2}\frac{K_3(\zeta)}{K_2(\zeta)} - \frac{1}{\zeta} + \frac{K_1(\zeta)}{K_2(\zeta)} - \frac{Ki_1(\zeta)}{K_2(\zeta)}\right) \quad , \tag{2.48}$$

with $Ki_1(\zeta) = \int_0^\infty e^{-\zeta\cosh(t)}/\cosh(t)\,\mathrm{d}t$.

Our numerical findings for k $f(\zeta)$ are shown in Fig. 2.7. For some ζ values we have used RLBM with several different quadratures, the corresponding results differing from each other by approximately 1%; we

consider this an estimate of our systematic errors. Fig. 2.7 also shows the CE prediction (Eq. 2.48) that almost perfectly matches our results (we remark that *no* free parameters are involved in this comparison) and nicely goes over to the well-known non-relativistic limit for large values of ζ. In order to provide a more quantitative appreciation of the significance of our result, we also plot the predictions of Grad's method, which obey the following equation:

$$f(\zeta) = \frac{3}{2}\frac{K_3^2(\zeta)}{K_2(\zeta)\ K_4(\zeta)} \quad . \tag{2.49}$$

Comparison of the two curves allows to conclude that our level of resolution is fully adequate to discriminate between the two options. We can conclude that the correct transport coefficients for our model are provided by the Chapman Enskog expansion.

2.5 Forcing Scheme

The definition of force in relativity is subject to a certain degree of arbitrariness due to the lack of certain general properties such as, for example, Newton's third law [86]. In the following we will use the definition of the Minkowski force:

$$K^\alpha = m\frac{\mathrm{d}U^\alpha}{\mathrm{d}\tau} \quad , \tag{2.50}$$

subject to the condition

$$K^\alpha p_\alpha = K^0 p^0 - \boldsymbol{K}\cdot\boldsymbol{p} = 0 \quad , \tag{2.51}$$

and

$$\boldsymbol{K} = \gamma\ \boldsymbol{F} \quad . \tag{2.52}$$

To introduce a forcing term in our numerical scheme we make the following two assumptions: i) the force does not depend on the momentum vector ($\frac{\partial K^\alpha}{\partial p^\alpha} = 0$) ii) the distribution function in not far from the equilibrium, such that we can approximate the term $K^\alpha \frac{\partial f}{\partial p^\alpha}$ in Eq. 2.15 with an expansion that uses the same polynomials used for the equilibrium distribution function:

$$\frac{\partial f}{\partial p^\alpha} \approx \frac{\partial f^{\mathrm{eq}}}{\partial p^\alpha} = \omega(p^0)\sum_{k=0}^{\infty} b^{(k)}((U^\mu),T)J^{(k)}((p^\mu)) \quad , \tag{2.53}$$

with the projection coefficients defined as

$$b^{(k)}((U^\mu),T) = \int_{\mathbb{R}^D} \frac{\partial}{\partial p^\alpha} f^{\mathrm{eq}}((p^\mu),(U^\mu),T) J^{(k)}((p^\mu)) \frac{\mathrm{d}\boldsymbol{p}}{p^0} \quad . \tag{2.54}$$

2.6 Relativistic Lattice Boltzmann Algorithm

The initial conditions for the RLBM algorithm consist in providing the values of $f_i(\boldsymbol{x}, t_0)$ at a initial time t_0. A typical choice is to prescribe the equilibrium distribution function with a given initial profile for temperature, density and velocity, thus setting $f_i(\boldsymbol{x}, t_0) = f_i^{eq}$.

For each time step the following operations needs to be performed to evolve each single grid point:

1. We start by computing the first and second moment of the distribution:

$$N^\alpha = \sum_i f_i \bar{p}_i^\alpha \quad ,$$

$$T^{\alpha\beta} = \sum_i f_i \bar{p}_i^\alpha \bar{p}_i^\beta \quad .$$

2. The energy density ϵ and the four velocity U^α are obtained solving the eigenvalue problem:

$$\epsilon U^\alpha = T^{\alpha\beta} U_\beta \quad ,$$

with ϵ corresponding to the largest eigenvalue of $T^{\alpha\beta}$, and U^α being the correspondent eigenvector.

3. Next, we can get the particle density

$$n = U_\alpha N^\alpha \quad .$$

4. We then compute the temperature from the equation of state (see Section 1.5).

5. We now have all the fields required to compute the equilibrium distribution function:

$$f_{iN}^{\mathrm{eq}}((\bar{p}^\mu),(U^\mu),\bar{T}) = w_i \sum_{k=0}^{N} a^{(k)}((U^\mu),\bar{T}) J^{(k)}((\bar{p}_i^\mu)) \quad .$$

6. If present, we compute the Minkowski forcing term (see Section 2.5).

7. We now determine the local value for τ (typically by requiring a constant value for the ratio η/s, with s the entropy density).

8. Finally, we can evolve the system via the discrete Boltzmann equation:

$$f_i(\boldsymbol{x} + v^i \Delta t, t + \Delta t) - f_i(\boldsymbol{x}, t) = \Delta t \, \frac{p_i^\mu U_\mu}{p^0 \tau} (f_i^{\mathrm{eq}} - f_i) + F_i^{\mathrm{ext}}$$

We have here implicitly made use of the Anderson-Witting collisional operator (Section 1.3.2), which is compatible with the Landau-Lifshitz decomposition. Because of this, computing the energy density ϵ requires solving an eigenvalue problem. If we were to make use instead of the Marle collisional operator (Section 1.3.1), which is compatible with the Eckart decomposition, the computation of n, U^α, ϵ would significantly simplify:

$$\begin{aligned} &1. \quad n = \sqrt{N^\alpha N_\alpha} \quad , \\ &2. \quad U^\alpha = N^\alpha / n \quad , \\ &3. \quad \epsilon = T^{\alpha\beta} U_\alpha U_\beta \quad . \end{aligned}$$

2.7 Conversion between physics and lattice units

In this section we discuss the conversion between physics and lattice units. To relate physical space and time units with the corresponding lattice units, one starts by assigning the physical length δx, corresponding to one lattice spacing. Suppose we use N grid points to represent the lenght scale l, having physical units, this corresponds choosing the lattice spacing δx as:

$$\delta x = \frac{l}{N} \quad . \tag{2.55}$$

Time and space units are linked via Eq. 2.28, and we therefore write:

$$\delta t = \frac{\delta x}{v_0 \; c} \quad . \tag{2.56}$$

The translation of lengths and time units between physics and lattice units is then straightforward, and likewise for derivate quantities. In the following we give a few examples, where we distinguish between physics and lattice units indicating quantities with a f or L subscript respectively. Assuming

$D = 3$, the conversion of the particle number density reads then

$$n_f = n_L \frac{1}{(\delta x)^3} \quad . \tag{2.57}$$

Similarly, a generic velocity can be converted using

$$v_f = v_L \frac{\delta x}{\delta t} \quad . \tag{2.58}$$

The conversion of all energy related quantities is performed by choosing a value for the reference temperature T_0, introduced in the previous sections for defining non-dimensional quantities on the lattice. While the choice of T_0 is in principle arbitrary, a sensible choice can have a major impact on the accuracy of the results. In fact one can expect better results when T_0 is chosen such that the numerical values of T_L are ~ 1, since such value was used as expansion origin for the equilibrium distribution function. As a final example we translate in lattice units the shear viscosity, for which we take the expression given by the Chapman Enskog expansion in the massless limit:

$$\eta_f = \frac{4}{5} P \tau = \frac{4}{5} n T \tau \quad . \tag{2.59}$$

It follows:

$$\eta_f = \eta_L T_0 \frac{\delta t}{(\delta x)^3} \quad . \tag{2.60}$$

2.8 Numerical validation: The Riemann problem

In this section we present a validation of the RLBM algorithm solving a well known instance of the 1D Riemann problem, the Sod's shock tube, for a quark-gluon plasma. The 1D Riemann problem is a widely adopted benchmark for the validation of numerical hydrodynamics methods which has an exact solution in both the classic case [87] and in the relativistic regime [9,87]. From a physical point of view the problem consists of a tube filled with a gas, with two chambers separated by thin a membrane placed at $x = 0$ at time $t = 0$. The two parts of the fluid are set at different initial state, such that the macroscopic quantities describing the fluid present a discontinuity at the membrane. Once the membrane is removed the discontinuities decay producing shock/rarefaction waves, depending on the initial configuration chosen for the two different chambers. For the relativistic case, an exact solution exists only in the inviscid limit. Starting

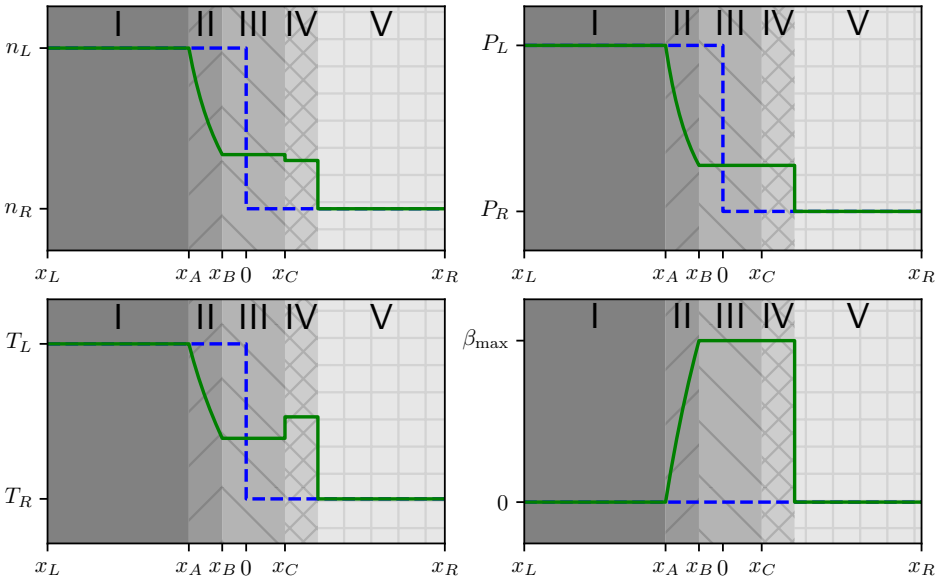

Figure 2.8: *Example of analytic solution of the Sod's shock tube problem in the inviscid limit, using a ultra-relativistic equation of state in* $(3+1)$ *dimensions. The blue dotted lines represent the initial conditions while the green lines represent the solution at a certain time* $t > 0$*. Refer to [57] for a detailed definition of the macroscopic quantities in the five different regions shown in the plot.*

from the following initial conditions:

$$\begin{aligned} n = n_L, \quad T = T_L, \quad \beta = 0, \quad \text{if } x < 0 \\ n = n_R, \quad T = T_R, \quad \beta = 0, \quad \text{if } x > 0 \end{aligned} \tag{2.61}$$

the evolution of the system can be characterized, at a generic time $t > 0$, by defining the different macroscopic quantities in the five regions shown in the example in Fig. 2.8. For the ultra-relativistic case in $(3+1)$ dimensions the full form of the solution is described, e.g., in [57]. When a non-zero viscosity is introduced, dissipation smooths the interfaces between the different regions. Since in the viscous regime it is not possible to formulate an exact solution to the problem, we will compare with the solution provided by other numerical solvers such as the Boltzmann approach multi-parton scattering program (BAMPS) [88, 89].

2.8.1 Numerical setup

The initial conditions, that follow a benchmark performed by BAMPS, are defined by a pressure step having, in physical units, $P_L = 5.43$ GeV/fm^3

and $P_R = 0.339$ GeV/fm^3, with corresponding initial temperatures $T_L =$ 400 MeV and $T_R = 200$ MeV. In these kind of simulations one usually keeps fixed the ratio between the shear viscosity and the entropy density (η/s) to a constant.

To make contact with real-life physics, it is necessary to convert from physical units to lattice units. Following the discussion in the previous section, we start by setting our reference temperature T_0 equal to T_L, thus $T_0 = T_L = 400$ MeV, which translates the initial temperatures on the lattice to $T_L = 1$ and $T_R = 0.5$. We also choose the initial values for the particle number density to be $n_L = 1$ and $n_R = 0.124$, which correctly reproduce the ratio P_L/P_R. We perform our tests on a grid of size $L_x \times 1 \times 1$, half of which represents the physical domain defined in the interval $(-3.2 \text{ fm}, 3.2 \text{ fm})$, while the other half forms a mirror image that allows using periodic boundary conditions. Taking for example $L_x = 6400$, it follows that on our grid 6.4 fm corresponds to 3200 grid points, that is $\delta x = 0.002$ fm. The corresponding value of Δt is quadrature dependent; considering for example the third order quadrature for $\zeta = 0$ described in Appendix E having $v_0 = 1/\sqrt{41}$, we obtain $\Delta t \approx 0.013$ fm/c.

Another important quantity that needs to be properly taken into account is the relaxation time τ, which is used to control the transport coefficients in the simulations. In the numerical setup τ is expressed in lattice time units, so it naturally follows that $\tau = \tau_f \Delta t$, where the physical value τ_f is related to the transport coefficients of the system that one wants to study. As mentioned above, to perform realistic simulations of a quark-gluon plasma one needs to keep fixed the ratio η/s, where the link between τ_f and η was given in Eq. 2.48. The entropy density can be calculated following the relation $s = 4n - n \ln (n/n^{\text{eq}})$, where n^{eq} comes from the equilibrium function, $n^{\text{eq}} = d_G T^3/\pi^2$, with $d_G = 16$ the degeneracy of the gluons [90]. Since s is implicitly given in terms of $\hbar$ one needs some extra care when converting the ratio η/s on the lattice:

$$\hbar s_f = \left(\hbar c \frac{v_0}{c} \frac{1}{\Delta x T_0}\right) s \quad , \tag{2.62}$$

where in parenthesis we have given the dimensionally correct conversion factor from lattice to physics units for the entropy density (in terms of $\hbar$). Therefore, wanting to keep the ratio η/s fixed to a constant value k, we

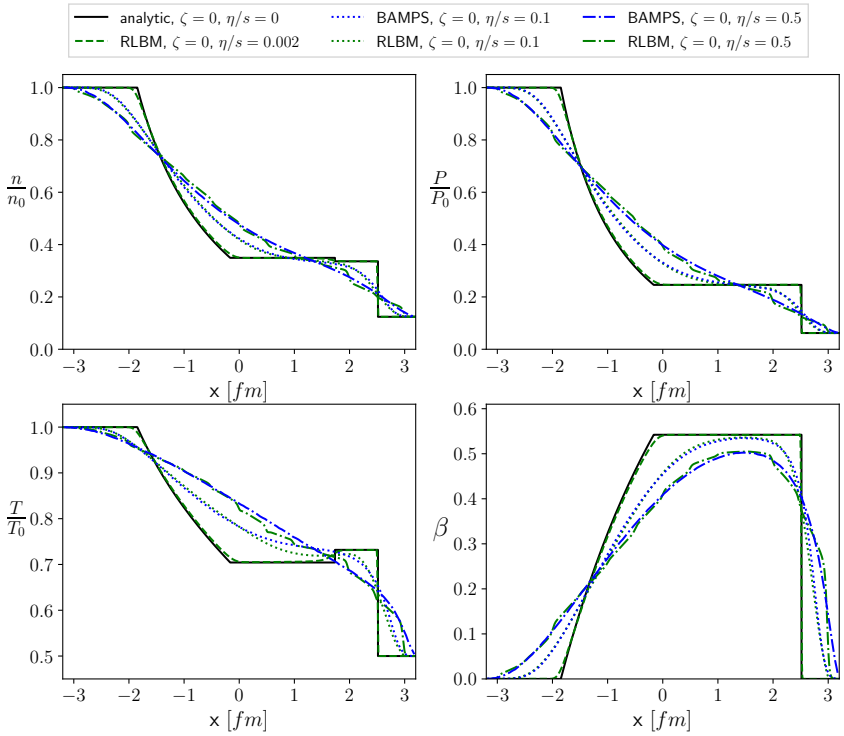

Figure 2.9: *Sod's shock tube for a gas of massless particles at* $t =$ 3.2 fm/c, *for several values of* η/s. *The results of simulations of the RLBM (green lines) at* $\eta/s = 0.1$ *and* $\eta/s = 0.5$ *are compared against the results provided by BAMPS (blue lines). It is evident that decreasing the value for* η/s *the results of RLBM tends to those given by the analytic solution (black line) in the inviscid limit. Top: left) density profile right) pressure profile. Bottom: left) temperature profile right)* $\beta = |U^i|/U^0$. *All macroscopic quantities are plotted in non-dimensional units by dividing for their correspondent initial values at* $x = -3.2$ fm.

obtain the following expression for the relaxation time:

$$\tau = \frac{1}{2} + k \frac{4n - nlog(n\frac{\pi^2}{16T^3})}{\frac{4}{5}nT} \frac{\hbar}{T_0} \frac{v_0}{\Delta x} \quad . \tag{2.63}$$

2.8.2 Ultra-relativistic regime

In Fig. 2.9 we present the results of simulations using a RLBM model with $\zeta = 0$, for a few selected values of η/s, corresponding to different viscous regimes: $\eta/s = 0.002$ which describes a nearly inviscid hydrodynamic regime, $\eta/s = 0.1$ characterized by a large viscosity and where an

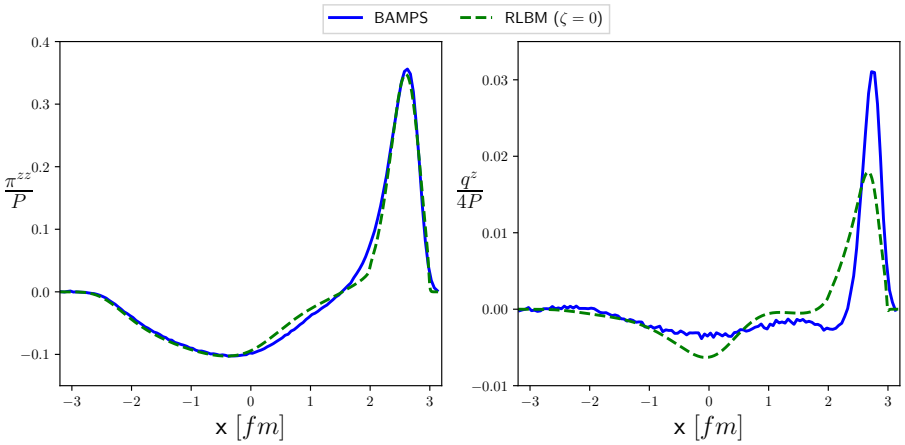

Figure 2.10: *Comparison of BAMPS and our RLBM for the Riemann problem at $t = 3.2$ fm/c ($\zeta = 0, \eta/s = 0.1$). Left) viscous pressure tensor; Right) heat flux profile.*

hydrodynamic approach is still justified, and $\eta/s = 0.5$ where we enter a transition towards a ballistic regime (thus going beyond hydrodynamics). One can appreciate that for $\eta/s = 0.002$ the macroscopic profiles well compares with the analytic solution in the inviscid limit, and indeed we can clearly recognize the five different regions previously defined in the example in Fig. 2.8. The case $\eta/s = 0.1$, instead, is in excellent agreement with the results provided by BAMPS. Here we can observe that as the viscosity is increased, the interfaces between the different regions becomes more smooth, and eventually cannot be distinguished anymore when we move to $\eta/s = 0.5$: in this case we are transitioning towards a ballistic regime, where our hydrodynamic approach shows its limitations.

In Fig. 2.10 we also present the profile of the π^{zz} component of the pressure viscous tensor and of the q^z component of the heat flux, showing good agreement with the results produced by BAMPS for the first, while non-negligible differences arise for the latter. Since the Anderson Witting model provides only one free parameter τ, a fine description of several transport coefficients would require extensions to a multi relaxation time collisional operator.

2.8.3 Mildly-relativistic regime

Using the same numerical setup introduced in the previous section, we now perform simulations by varying ζ, and the equation of state accordingly. In Fig. 2.11 we show the profiles for the pressure and for β, with two

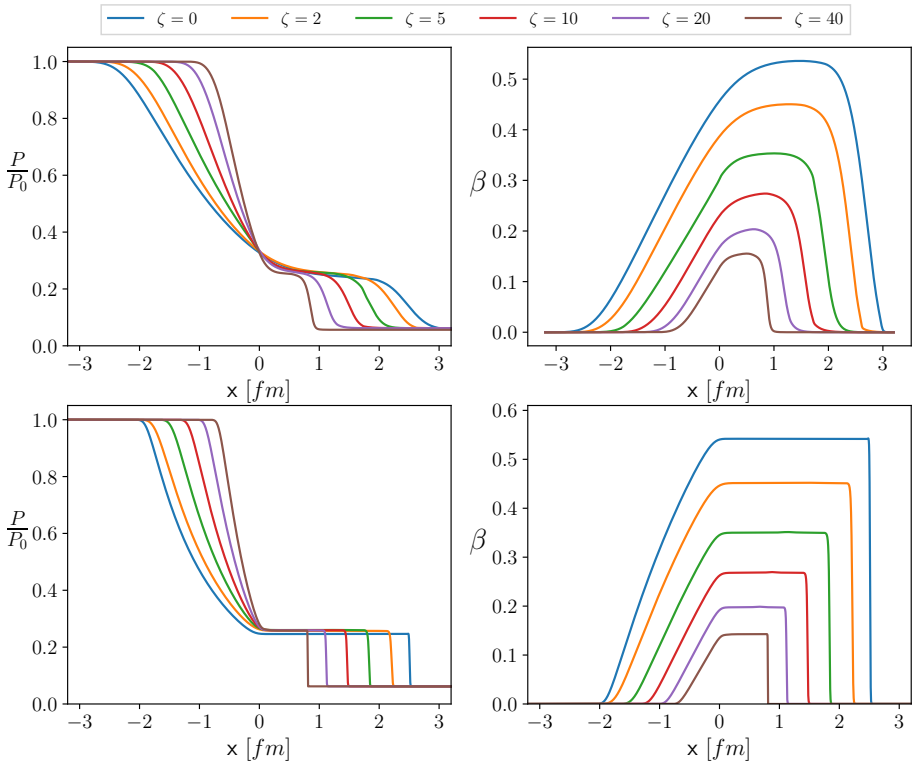

Figure 2.11: *Sod's shock tube using the same parameters used in the previous test case (Fig. 2.9) at $t = 3.2$ fm/c, varying ζ. The profiles for the pressure and for $\beta = |U^i|/U^0$ are shown in two different hydrodynamic regimes: Top: $\eta/s = 0.1$. Bottom = $\eta/s = 0.002$. All macroscopic quantities are plotted in non-dimensional units by dividing for their correspondent initial values at $x = -3.2$ fm.*

different values of η/s, respectively $\eta/s = 0.1$ for a highly viscous flow, and $\eta/s = 0.002$ for a closely inviscid one. While we do not have here reference data to compare against, one can appreciate the fact that as we reduce ζ the results becomes closer and closer to the ultra-relativistic ones; this shows that the present algorithm is a good candidate to bridge the gap between ultra-relativistic and non-relativistic regimes.

To conclude, we provide a comparison between the Anderson-Witting and the Marle collisional model. Since the model of Marle is appropriate only for mildly relativistic regimes, we consider $\zeta = 5$ for a fair comparison, and fix the numerical value of the relaxation time to $\tau = 5$. In Fig. 2.12 we compare the profiles for the pressure and for β given by the two collisional operators. As we can see, both yield very similar results, with a very good agreement when comparing the results for the pressure profile, and only

small discrepancies in the velocity profile.

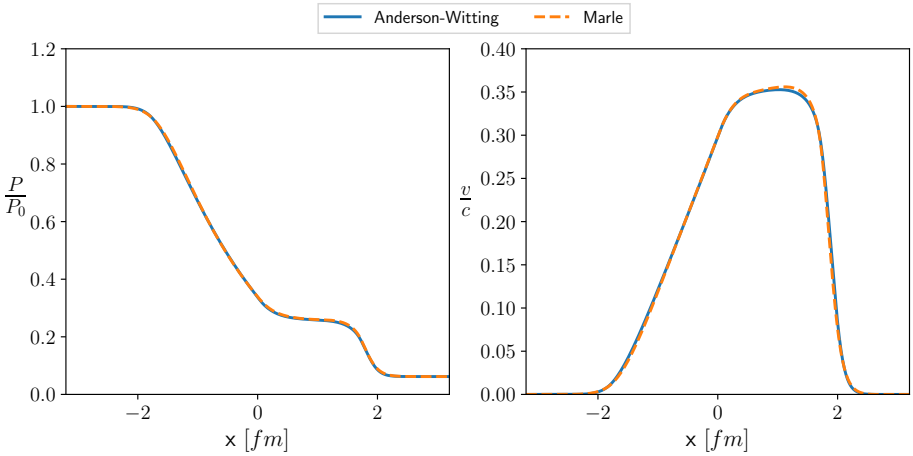

Figure 2.12: *Comparison between the Anderson-Witting and the Marle collisional operators, simulating a Sod's shock tube problem with $\zeta = 5$ and having fixed in both cases the relaxation time to $\tau = 5$. The snapshots are taken at $t = 3.2$ fm/c. Left: Pressure profile. Right: Profile of $\beta = |U^i|/U^0$. All macroscopic quantities are plotted in non-dimensional units by dividing for their correspondent initial values at $x = -3.2$ fm.*

3

Hydrodynamics of electrons in graphene

Abstract

Recent experimental studies have shown that certain features of the flow of electrons in graphene can be explained through a pseudo-relativistic hydrodynamic approach [91], confirming earlier theoretical predictions [92, 93]. The main aspect limiting the observation of hydrodynamic regimes in graphene, and in metals in general, is the scattering of electrons with impurities and phonons which has a destructive effect on the collective motion of electrons. Consequently, the observation of electronic hydrodynamics in graphene has required significant advances in the production of ultra-clean samples. Still, the contribution of phonons and impurities cannot be neglected in realistic simulations as they strongly contribute in increasing the effective viscosity of the system, which according to recent measurements [94, 95] is found to be an order of magnitude larger than that of honey. This chapter describe original result of this work, based on extensive numerical simulations of the electron flow in graphene for different hydrodynamical regimes. We start in Section *3.1* with linear steady-state flows in geometrical setups used in actual experiments, for which we give numerical evidence of the formation of electron back-flows (whirlpools) in the proximity of current injectors. In Section *3.2* we consider, instead, regimes where nonlinear effects start becoming relevant. By considering suitable geometries, we identify transport parameters for which preturbulence occurs at experimentally achievable values of the Reynolds number, and could be detected by analyzing the temporal fluctuations of the electric potential, which are found to span a spectrum of frequencies between 10 and 100 GHz.

The dynamic of electrons in condensed matter physics is normally studied in the ballistic-regime, due to the fact that electron-electron collisions can typically be neglected. Conversely, a hydrodynamic description is appropriate when the collective behavior of electrons becomes relevant. While the possibility of investigating electrons flow using the laws of hydrodynamics was realized already in the 1960s [96], this approach has not been taken into consideration until very recent times, as it was not feasible from an experimental point of view. Indeed, the observation of a electronic fluid in metals is particularly challenging due to the presence of impurities and phonons, which destroys the collective hydrodynamic flow of electrons. Recently, with the discovery of new materials exhibiting weak electron-phonon interactions, alongside technological advances which have allowed the production of ultra-clean samples, several experiments have provided evidence for electronic hydrodynamics in GaAs [97], graphene [94,95,98,99] PdCoO2 [100] and WP2 [101].

Of particular interest for this thesis work is the case of graphene, a 2D material consisting of a single layer of carbon atoms where due to the special symmetries of its honeycomb lattice electrons follow an "ultra-relativistic" dispersion relation [102]. As a consequence, electrons in graphene can be considered as a fluid of massless (quasi-)particles whose energy depends on the momentum as $E = v_{\mathrm{F}} p$, with $v_{\mathrm{F}} \sim 10^6$ m/s the Fermi speed, mimicking the role of the speed of light in true relativistic systems.

From a theoretical point of view one of the most interesting features of graphene is its capability of reaching very small viscosity to entropy ratios [93], close to the conjectured lower bound $\eta/s = 1/4\pi$ [103, 104]. Given this context, it is natural to investigate if nonlinear terms of the Navier-Stokes equations, which have proven unnecessary so far to explain experimental results [91, 94, 95, 97–100], may become relevant. A first study investigating preturbulent regimes in graphene was presented at the beginning of the decade, basing on numerical simulations making use of a RLBM solver [105]. Although it was suggested that preturbulent phenomena could be observed with experimental setup that could be assembled at the time, still, almost ten years later, electronic turbulence has not been disclosed experimentally. The reason is that the numerical setup used in [105] was overly-idealized and in particular did not take into account electron-phonon interactions. On the other hand both phonons an impurities significantly limit the mobility properties of the electrons, drastically reducing the possibility of observing chaotic behaviors [106].

The electronic properties of graphene, and likewise for any other material, are strongly affected by phonons and impurities which are always present in any experimentally realized system. Being graphene de-facto a 2D material, the dominant source of impurities are to be found out of the carbon atoms plane, in the substrates on the top of which the graphene layer is inevitably located. While the electronic properties are limited by impurities at low temperatures, phonons constrain the electronic mobility at higher temperatures [107, 108].

The interest towards the numerical study of electrons flow in graphene has motivated the development of two-dimensional RLBM solvers [59–61, 105]. Most of these numerical methods are based on a second order expansion of the equilibrium distribution function following the Fermi-Dirac statistics, and they have been applied to study, for example, low-viscosity preturbulent regimes [105]. In Section *1.4*, working in three dimensions, we have shown that models based on the third order expansion of the equilibrium distribution are the minimum requirement to correctly handle dissipative effects in simulations of the relativistic regime. For this reason, in this chapter we use a $(2+1)$ RLBM formulation based on the third order expansion of the Maxwell-Jüttner distribution. As a consequence quantum effects will be neglected, a choice which simplifies the algorithmic derivation allowing us to retain one of the main LBM features, namely perfect streaming. In Section *3.1* we provide a first validation of our approach simulating a laminar flow in the so-called "vicinity-geometry", which was considered in a series of papers [94,109,110] to outline phenomena such as negative nonlocal resistance and current whirlpools. The numerical method is tested in a steady-state regime, for which semi-analytical solutions are available, showing satisfactory agreement with previous works [63]. In Section *3.2* we take into consideration time-dependent nonlinear flows, where we investigate the impact of phonon-electron scattering on the possible experimental detection of preturbulent signals in electronic flows in graphene [111].

3.1 Current whirlpools in the vicinity-geometry

In this section we provide a benchmark for the simulation of a single layer graphene sheet in the so-called "vicinity-geometry", using the RLBM in $(2+1)$ dimensions presented in the previous chapter. As already remarked, in this case the Fermi velocity v_{F} of the simulated system plays the role of

the speed of light. We consider an experimental setup consisting of an ultra-clean single layer graphene encapsulated between boron nitride crystals (hBN), a dielectric material which helps enhancing the hydrodynamic behavior of electrons in the graphene layer [94, 109, 110].

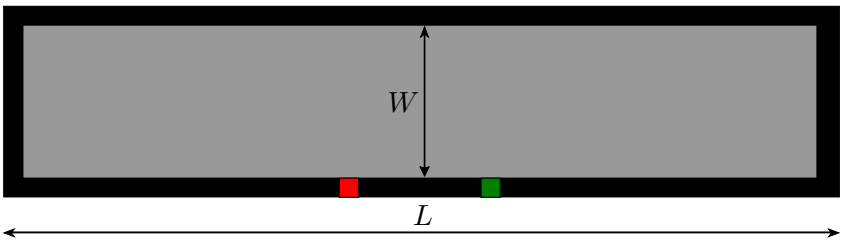

Figure 3.1: *Sketch of the geometry used for the validation of the code. Two contacts are used to inject (red area) and drain (green area) a current from a graphene sheet of width W. The current is zero at the boundaries of the sample (black areas). In real experiments, measurements of voltage drops in the proximity of the injectors are found to be dependent on the viscosity of the electronic fluid [109].*

The geometry is sketched in Fig. 3.1; two contacts are used to inject (red points) and drain (green points) a constant current from a graphene sheet of width W. Experimental measurements have shown voltage drops in the proximity of the injectors, which are found to be dependent on the viscosity of the electronic fluid [109]. In order to explain the experimental results, the authors in [109] have derived an analytic approximation for the electrochemical potential in the proximity of the injectors, which we rewrite as follows:

$$\Phi(r,\theta) \approx \frac{2I\eta}{\pi\bar{n}^2e^2}\frac{cos(2\theta)}{r^2} \quad , \tag{3.1}$$

where I is the driving current at the contact, η is the shear viscosity, $\bar{n}$ is the equilibrium density, e is the electron charge, r and θ are used to parametrize in polar coordinates the space in the proximity of the injector.

The expression in Eq. 3.1 has been obtained assuming an infinitely long channel. In our simulations we will use a lattice with an aspect ratio $L/W = 4$. Regarding boundary conditions, current is set to be zero at the boundaries of the sample (black areas of Fig. 3.1), while the equilibrium value of the distribution is imposed at the grid points used to represent the contacts [50].

The total force acting on the system is given by the vector sum of the force due to the electric field F_E and the force due to the pressure gradient F_P. While F_P is naturally described by the RLBM solver, F_E is included

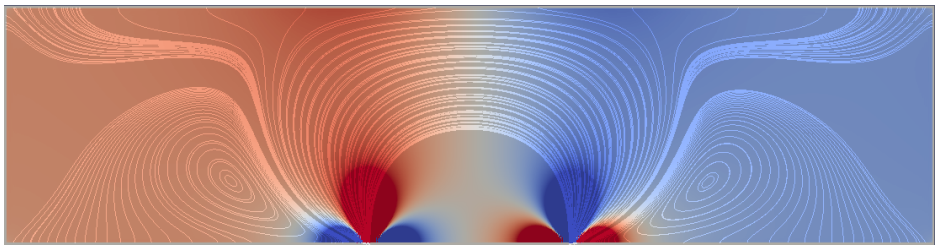

Figure 3.2: *Snapshot of a simulation on a* 2000×500 *lattice, taken after 100000 time steps, with an initial uniform density* $n = 1.5$*, initial* $T = 1.0$*, a fixed velocity at inlet* $v^{in} = 10^{-5}$*,* $\tau = 1.0$*,* $C_g = 10$*. All quantities are given in numerical units. The color map describes the electrochemical potential (red colors positive potential, blue colors negative potential). Thick lines represent the electrons velocity streamlines.*

in the form of an external force and corresponds to a self-consistent electric field:

$$F_E = -ne\nabla\varphi \quad . \tag{3.2}$$

For simplicity, we do not solve explicitly the Poisson equation in the calculation of the electric potential, we follow instead [112] and use the local capacitance approximation:

$$\varphi(\boldsymbol{x}) = -\frac{e\delta n(\boldsymbol{x})}{C_g} \quad , \tag{3.3}$$

where $\delta n(\boldsymbol{x}) = n(\boldsymbol{x}, t) - \bar{n}$, with $\bar{n}$ the uniform value of the background electron density, and C_g the geometrical capacitance per unit area, depending on both the geometrical and permittivity properties of the dielectric layer. In this first test case we also neglect for simplicity the contribution due to electron-phonon scattering.

In Fig. 3.2 we show a snapshot of a simulation in a highly viscous regime, where it can be observed that results are qualitatively comparable with those presented in [94, 109]. In particular one appreciates the (symmetric) formation of electron back-flows in the proximity of the gates, so called current whirlpools. For a more quantitative comparison, we take into consideration the electrochemical potential and the expression given in Eq. 3.1. Since this quantity is not a direct observable of the lattice formulation, we need to perform a matching procedure of the parameters.

By assuming a *quasi-incompressible* regime simple mathematical calcu-

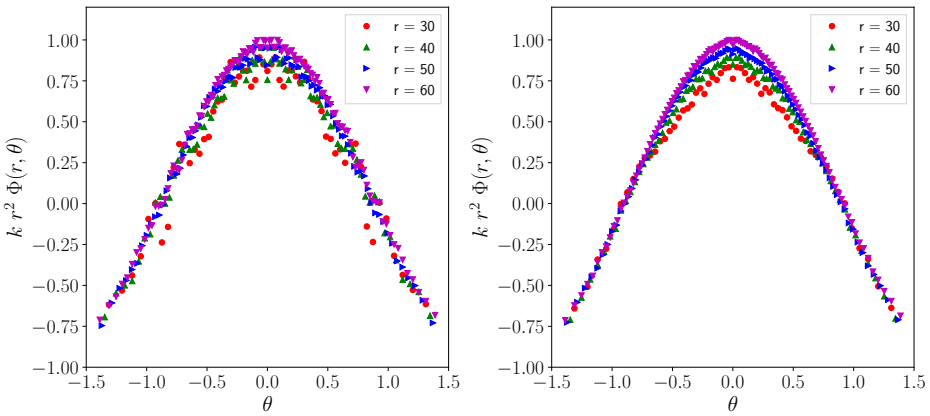

Figure 3.3: *Electric potential measured at several fixed distances r from the current injector. Plots present the quantity $r^2\ \Phi(r,\theta)$ normalized to $\Phi(60,0)$, showing that simulated data points collapse onto a single line, as predicted by Eq. 3.1. Results taken from a simulation on a 2000×500 lattice, with an initial uniform density $n = 1.5$, $T = 1.25$, $C_g = 10$ and a fixed velocity at inlet $v^{in} = 10^{-5}$ (all quantities in non-dimensional units). Left: $\tau = 0.8$. Right: $\tau = 1.2$.*

lation lead to the following approximation for the electrochemical potential:

$$\Phi(\boldsymbol{x}) = \varphi(\boldsymbol{x}) - \frac{\delta P(\boldsymbol{x})}{e\bar{n}} \ , \tag{3.4}$$

where we have used the local approximation [113]:

$$\delta P(\boldsymbol{x}) = P(\boldsymbol{x}) - \bar{P} \approx \frac{E_F}{2}\delta n(\boldsymbol{x}) = \frac{E_F}{2}\left(n(\boldsymbol{x},t) - \bar{n}\right) \quad , \tag{3.5}$$

with $E_F = \hbar v_F \sqrt{\pi \bar{n}}$ the Fermi energy in single-layer graphene. By coupling Eq. 3.4 together with the local capacitance approximation in Eq. 3.3 we can get another useful expression for Φ:

$$\Phi(\boldsymbol{x}) = -e\delta n(\boldsymbol{x}) \left(\frac{1}{C_g} + \frac{1}{C_Q}\right) \quad , \tag{3.6}$$

where $1/C_Q = E_F/(2\bar{n}e^2)$. In Fig. 3.3 we plot the electrochemical potential as a function of the polar angle θ for several lattice points at several distances r from the center of the injector. We show that for different setups, the quantity $r^2\ \phi(r,\theta)$ does not depend on r, as predicted by Eq. 3.1: to a good approximation, all curves collapse on the top of each other, as expected. As a further benchmark we evaluate how the steady state solution

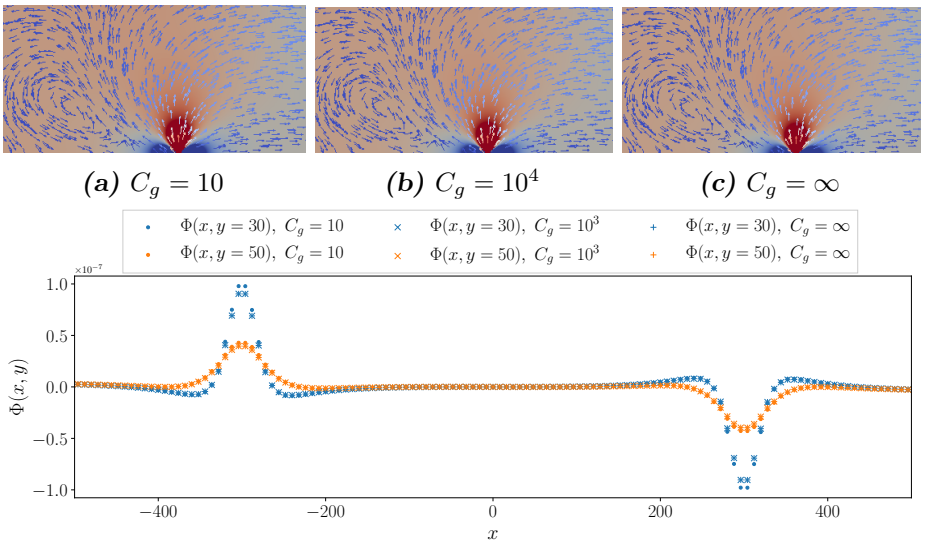

Figure 3.4: *Qualitative (top) and quantitative (bottom) comparison of the electrochemical potential Φ obtained by varying the intensity of the electric field F_E. Results taken from a simulation on a 2000×500 lattice, with an initial uniform density $n = 1.5$, $T = 1.25$, $\tau = 1.0$ and a fixed velocity at inlet $v^{in} = 10^{-5}$ (all quantities in non-dimensional units).*

reported in Fig. 3.2 varies when tuning the magnitude of the driving forces F_E and F_P. To this purpose, we perform simulations with different values of the parameter C_g to evaluate the role of the electric potential. In such linear flows Coulomb interactions are not expected to play a role [114]. In Fig. 3.4 we show that this is indeed the case; varying C_g over several different orders of magnitude does not yield any appreciable effect on the solution. Moreover the results are the same even in the case when F_E is neglected ($C_G = \infty$), proving that the model gives a self-consistent description of hydrodynamic theory on long length scales. On the other hand, the electric potential is expected to play a major role on the dynamic of non-linear, time-dependent flows. These type of flows are threated in full details in the next section.

3.2 Nonlinearities and detection of preturbulent signals

In this section we investigate preturbulent regimes in ultra-clean graphene samples. We considerably expand the scope of the early results presented in [105] by taking into consideration electron-phonon interactions as well as the effect of a self consistent electric field. We consider geometries

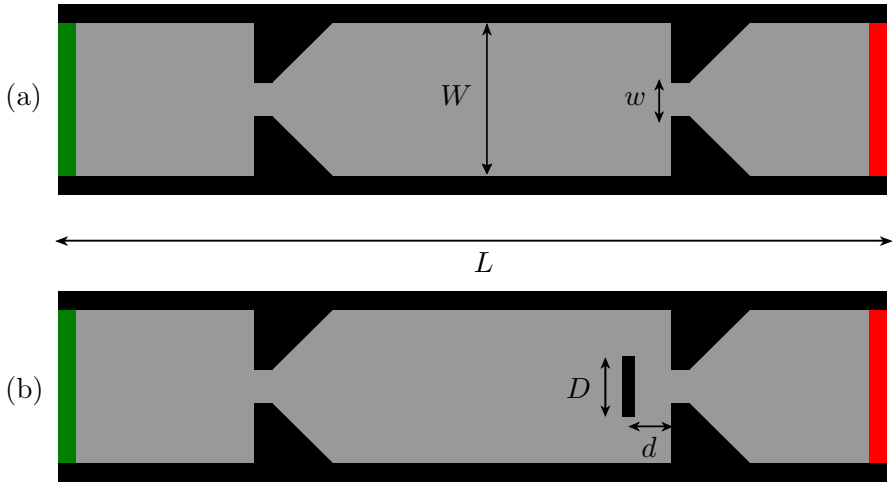

Figure 3.5: *Geometrical details of the setup analyzed in this work. Two graphene leads of width $W = 1$ μm are attached via "funnels" to a central area. Current is injected through an orifice of width $w = 0.32$ μm with an obstacle of length $D = 0.3$ μm placed at a lateral distance $d = 0.1$ μm from the orifice.*

close to the one used in recent experimental work [95], which made use of a constriction to emphasize a clear crossover from the ballistic to the hydrodynamic regime as a function of temperature. In Fig. 3.5 we show two geometries that will be used in simulations. The two cases differ by the presence of a thin linear obstacle, placed in front of the constriction, with the intent of triggering preturbulent flows at low Reynolds numbers. Both setups can be realized experimentally with current technology.

We also take into consideration a large set of values of the relevant physical parameters which we report in Tab. 3.1. All cases considered in this work fall in a regime of very small Mach number Ma, in which compressibility effects can safely be neglected. In this framework the Mach number is defined as the ratio between the plasma-wave velocity v_{PW} and

the fluid velocity of the electron fluid

$$v_{\mathrm{PW}} = \sqrt{\frac{e^2 \bar{n} v_{\mathrm{F}}^2}{C E_{\mathrm{F}}}} \quad , \tag{3.7}$$

where the quantity $C^{-1} = C_{\mathrm{g}}^{-1} + C_{\mathrm{Q}}^{-1}$ has been introduced in Eq. 3.6. We have verified both a priori and a posteriori that indeed $\mathrm{Ma} \ll 1$. Moreover, for values of the injected current sustained in state-of-the-art experiments, flows are characterized by velocities $v \ll v_{\mathrm{F}}$, and therefore it is generally safe to approximate the flow as non-relativistic [106]. For this reason the results reported in this section will be based on extensive numerical simulations making use of a classical LB solver. Since a careful development of accurate boundary conditions for the RLBM is still lacking, we use a isothermal version of the D2Q37 model [115, 116]. The development of accurate boundary conditions for the RLBM will allow in future works to evaluate the signature of the relativistic dispersion relation in the results here presented.

Table 3.1: *Typical values of physical parameters of state of the art experiments compared with those used in our simulations.*

	Typical experiments	This work
L	$5 \sim 30$ [μm]	10 [μm]
W	$1 \sim 5$ [μm]	1 [μm]
$\bar{n}$	$0.5 \sim 4 \cdot 10^{12}$ [cm^{-2}]	$2 \cdot 10^{12}$ [cm^{-2}]
I	$10^{-3} \sim 1$ [mA]	$10^{-3} \sim 1$ [mA]
ν	$0.01 \sim 0.1$ [m^2/s]	$10^{-4} \sim 10^{-3}$ [m^2/s]
τ_{D}	$1 \sim 5$ [ps]	$1 \sim 400$ [ps]
C_g/e^2	$3.03 \cdot 10^{34}$ [J^{-1}m^{-2}]	$3.03 \cdot 10^{35}$ [J^{-1}m^{-2}]

Within the LBM formulation we make use of a Maxwell-Boltzmann distribution, it follows that the hydrostatic contribution to the electrochemical potential in Eq. 3.6 gives an effective quantum capacitance that can be written as

$$\frac{1}{C_{\mathrm{Q,MB}}} = \frac{T}{\bar{n} e^2} \quad . \tag{3.8}$$

Observe that having assumed a iso-thermal dynamic, the temperature appears only in this term; this allows using the temperature as an effective parameter that we use to get the correct expression for the electrochemical potential:

$$T = \frac{E_{\mathrm{F}}}{2} = m \frac{v_{\mathrm{D}}^2}{2} \quad , \tag{3.9}$$

with $m = E_F/v_D^2$ for single-layer graphene.

In order to account for interactions with phonons and impurities we add a term to the external forces acting on the system (Eq. 3.2):

$$\boldsymbol{F} = e\nabla\varphi(\boldsymbol{r},t) - \frac{n(\boldsymbol{r},t)\boldsymbol{v}(\boldsymbol{r},t)}{\tau_D} \quad . \tag{3.10}$$

Once again, the first term on the right-hand side describes electric forces acting on a fluid element, with $\varphi(\boldsymbol{r},t)$ the electric potential in the 2D plane where electrons move. The second term describes forces that dissipate electrons momentum, due to impurities and acoustic phonons. These are parametrized as a friction term, with a single scattering time τ_D. Albeit very simple, this parametrization has proven successful in describing experiments in the linear-response regime [94, 95, 97–99].

In Fig. 3.6 we provide a few examples which qualitatively summarize the results of the simulations. We present three different cases differing by the magnitude of the injected current, and for each case we show color maps of the fluid velocity and of the electrochemical potential. For appropriate values of the transport parameters, that is to say low enough kinematic viscosity ν and large enough τ_D, a laminar behavior is found for low values of the current (10^{-3} mA, Fig. 3.6a) injected in the sample. As the current is increased ($0.5 - 1.0$ mA, Fig. 3.6b/c), the symmetry starts breaking and the flow exhibits a preturbulent behavior.

In current experiments it is not possible to map the fluid velocity everywhere in the sample, and measurements of the electrochemical potential can only be conducted at selected sites on the boundaries. In Fig. 3.7a we present a realistic quantitative analysis, which can be realized with current technologies, displaying the time evolution of electrochemical potential difference between locations corresponding to the black square and triangle in Fig. 3.6; once again we can appreciate a clear change from a constant to a periodic, to a more irregular evolution, which is best analyzed in the frequency domain, as shown in Fig. 3.7b.

It is clear that one can vary several parameters and yet obtain results qualitatively similar to those shown in Fig. 3.6. For example in Fig. 3.8 we show examples of simulations where the injected current and the kinematic viscosity are kept fixed while varying τ_D, the typical interaction time with phonons. As the electron-electron interactions start becoming dominant over phonon-electron scattering we observe the crossover from a laminar to a preturbulent flow. We should remark that here and throughout this chapter, we refer to "crossover" as a generic term, since the investigating

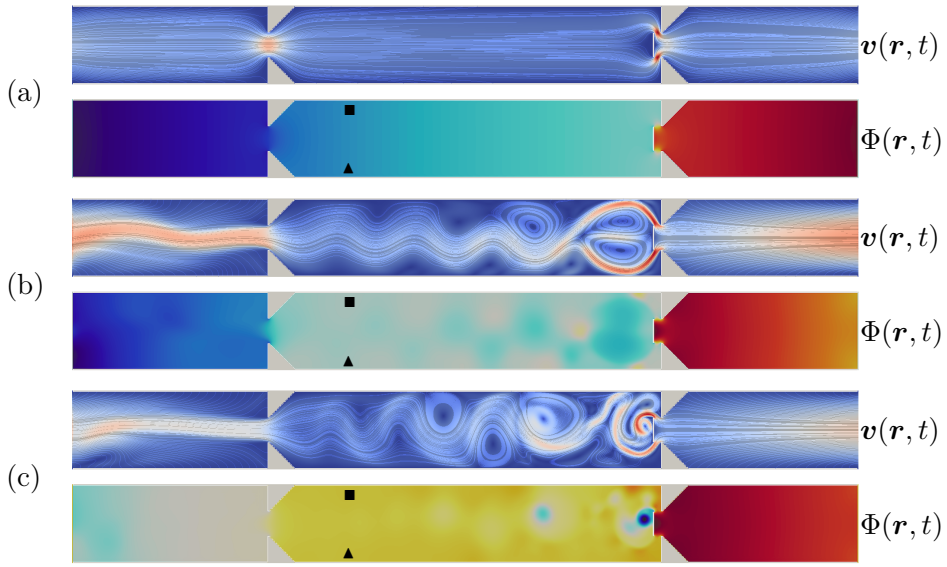

Figure 3.6: *Preturbulence in high-quality graphene. The different panels show snapshots of simulations for several values of the injected current. All the simulations make use of the following parameters:* $\nu = 4 \times 10^{-4}$ m^2/s, $\tau_{\rm D} = 50$ ps, *and* $C_{\rm g}/e^2 = 1.52 \cdot 10^{35}$ J^{-1}m^{-2}. *a) Velocity field* $\boldsymbol{v}(\boldsymbol{r},t)$ *(top) and electrochemical potential* $\Phi(\boldsymbol{r},t)$ *(bottom) for an injected current* $I = 10^{-6}$ A. *b) Same as in panel b) but for an injected current* $I = 5 \cdot 10^{-4}$ A. *c) Same as in panels b) and c) but for* $I = 10^{-3}$ A.

of a possible critical behavior goes beyond the scope of the analysis here presented. With the aim of qualitatively characterizing the crossover, we then establish a criteria to determine the onset of a preturbulent regime, where in this context preturbulent refers to a regime prior to the onset of chaos, where periodic oscillations of the velocity field can be observed. For a given simulation, we measure at each time step the average value of $< u_y(x = L/2, y) >$. We consider the simulated flow to be in a preturbulent regime whenever the root mean square (RMS) of this quantity is larger than 1% of the velocity at the inlet. In Fig. 3.8 we show an example: the left panel shows, in a qualitative way, the onset of preturbulent features in the flow as τ_D is increased; the right panel, on the other hand, shows the behavior of the root mean square of $< u_y(x = L/2, y) >$ as a function of τ_D. For this particular example, we see that the crossover occurs in the τ_D interval $(90\text{ ps}, 95\text{ ps})$.

Although effective in characterizing the symmetry breaking, the criteria above defined is admittedly rather arbitrary. We therefore provide a second

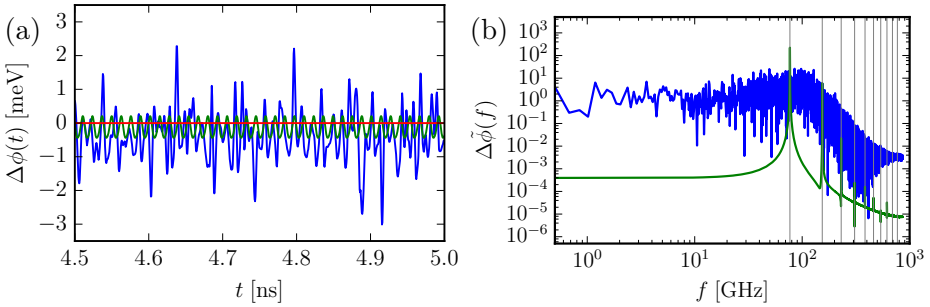

Figure 3.7: *(a) Time evolution of the electrochemical potential difference* $\Delta\Phi = \Phi(\bar{\boldsymbol{r}}, t) - \Phi(\bar{\boldsymbol{r}}', t)$*, with* $\bar{\boldsymbol{r}} = (3\ \mu\text{m}, 0.1\ \mu\text{m})$ *and* $\bar{\boldsymbol{r}}' = (3\ \mu\text{m}, 0.9\ \mu\text{m})$*. These two points have been marked in Fig 3.6a by a triangle (*$\bar{\boldsymbol{r}}$*) and a square (*$\bar{\boldsymbol{r}}'$*). Numerical results shown is this figure have been taken from simulations using* $\nu = 4 \times 10^{-4}$ m^2/s*,* $\tau_{\text{D}} = 50$ ps*,* $C_{\text{g}}/e^2 = 1.52 \cdot 10^{35}$ J^{-1}m^{-2}*, and the following values of the injected current:* $I = 10^{-6}$ A *(red),* $I = 5 \cdot 10^{-4}$ A *(green), and* $I = 10^{-3}$ A *(blue). (b) Fourier transform of the signals shown in panel (a). The gray vertical lines represent the first ten harmonics of the dominant frequency of the periodic signal obtained from the simulation at injected current* $I = 5 \cdot 10^{-4}$ A*.*

example of criteria that could be employed to identify the crossover from a laminar to a preturbulent regime which, instead, takes into account the vorticity, generally defined as the curl of the velocity (a scalar in the 2D case). In particular, we take into consideration the RMS of the average value of the vorticity. From Fig. 3.9 we can see that for $\tau_D < 90$ the average value of the vorticity is very close to zero, due to the symmetric behavior of the laminar flow; an abrupt change occurs in the interval $\tau_D \in (90\text{ ps}, 95\text{ ps})$, where the RMS of the average value of the vorticity grows of 6-7 orders of magnitudes. Observe that the interval where the crossover occurs in similar to the one established with the previous criteria.

Having defined a criteria to quantify the crossover between laminar and preturbulent flows we proceed by carrying out a large number of simulations, where, for a fixed geometry setup and magnitude of the injected current, we inspect a wide region in the ν-τ_{D} plane. Results are collected in Fig. 3.10, showing the smallest value of τ_{D} (identified by the symbol τ_D^*) as a function of ν, for which a transition to an observable preturbulent regime occurs.

To get a better understanding of the data presented in Fig. 3.10, it is instructive to refer once again to the parameters and settings of state-of-the-art experiments, reported in Tab. 3.1. Recent works [94, 95] have reported direct experimental measurements of the kinematic viscosity ν of the 2D

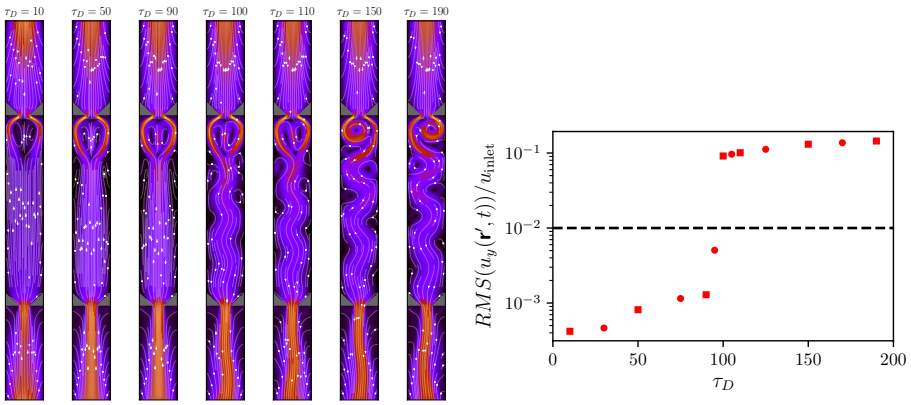

Figure 3.8: *The plot in the right panel shows the ratio between the root mean square transversal velocity along the middle section ($\boldsymbol{r'}$) of the device and the velocity at the inlet, as a function of τ_D. The black dotted line represents the (empirical) threshold used to establish the crossover between a laminar and a preturbulent regime. In this example the crossover occurs in the τ_D interval* (90 ps, 95 ps)*. All simulations use an inlet velocity consistent with $I = 5 \cdot 10^{-4}$* A *and $\nu = 0.45 \cdot 10^{-3}\text{m}^2/\text{s}$. Squares refer to simulations for which a snapshot of the velocity profile is shown in the left panel; we show the velocity streamlines while colors map the module of the velocity.*

electron system in graphene, found to be of the order of $\nu \lesssim 0.1$ m^2/s. For what concerns electron-phonon interactions, in graphene encapsulated between hexagonal Boron Nitride crystals (hBN) τ_{D} falls in the range between 1 and 2 ps in experiments conducted at temperatures of 70-300 K, where hydrodynamic behavior is strongest. Keeping this in mind, a first inspection of Fig. 3.10 may therefore convey disappointing news: for values of the parameters currently achieved in experiments, no preturbulent behavior can be detected. On the other hand, it can be appreciated the significant impact of the choice in the geometrical setup, which can help triggering preturbulent signals at low Reynolds numbers. Indeed comparing the results obtained using the two different geometries shown in Fig. 3.5 it is evident that placing a thin obstacles in from of the occlusion helps triggering preturbulence at viscosities about one order of magnitude larger that those allowed by the most basic geometrical setup. We stress here that the geometry in Fig. 3.5 is by no means optimal, and one can expect further optimizations to result from a concerted effort between future numerical and experimental investigations.

This, together with substantial, but not unconceivable, improvements of

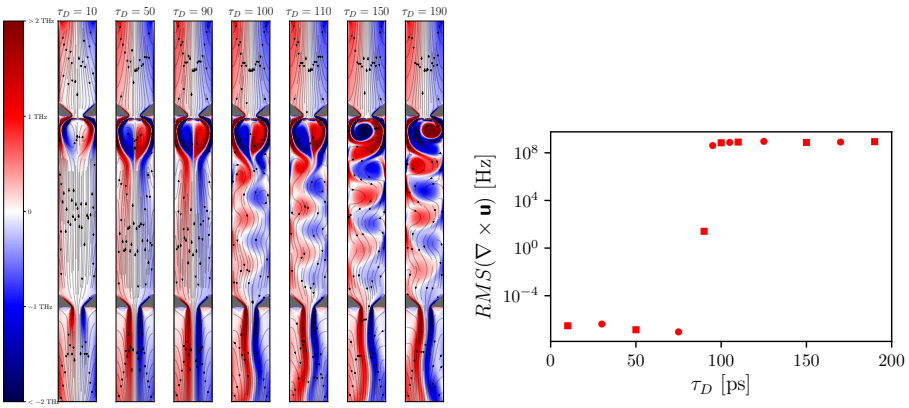

Figure 3.9: *The plot in the right panel shows the root mean square value of the average of vorticity as a function of τ_D; we once again observe an abrupt change in the τ_D interval* (90 ps, 95 ps) *similarly to Fig. 3.8. All simulations use the same physical parameters as in the previous figure. Squares refer to simulations for which a snapshot of the vorticity profile is shown in the left panel; these profiles show again the velocity streamlines but this time colors map the vorticity profile.*

the transport parameters driven by technological advance in material science may eventually lead to the observation of preturbulent electronic flows. Another positive aspect is that according to our results, the frequency distribution of the electrochemical potential falls within a measurable regime, between 10 and 100 GHz.

From a purely fluid-dynamics point of view, it is interesting to characterize the crossover lines shown in Fig. 3.10 in terms of an appropriate figure of merit. To this purpose, we develop a simplified model, whose starting point is the role played by the Reynolds number as an indicator of turbulence. In the present case, the turbulence-suppressing effect of the dissipative term in the Navier-Stokes equation is further enhanced by electron-phonon scattering. We therefore introduce a modified Reynolds number Re′, incorporating the effect of electron-phonon dissipation:

$$\mathrm{Re}' = \frac{|\boldsymbol{v}|\ \ell}{\nu + \dfrac{\ell^2}{\tau_\mathrm{D}}} \quad , \tag{3.11}$$

with $|\boldsymbol{v}|$ a typical fluid-element velocity and ℓ a typical macroscopic length scale. This very simple model proves adequate to characterize the actual behavior of the system. Lines in Fig. 3.10 are level lines for Re′, which

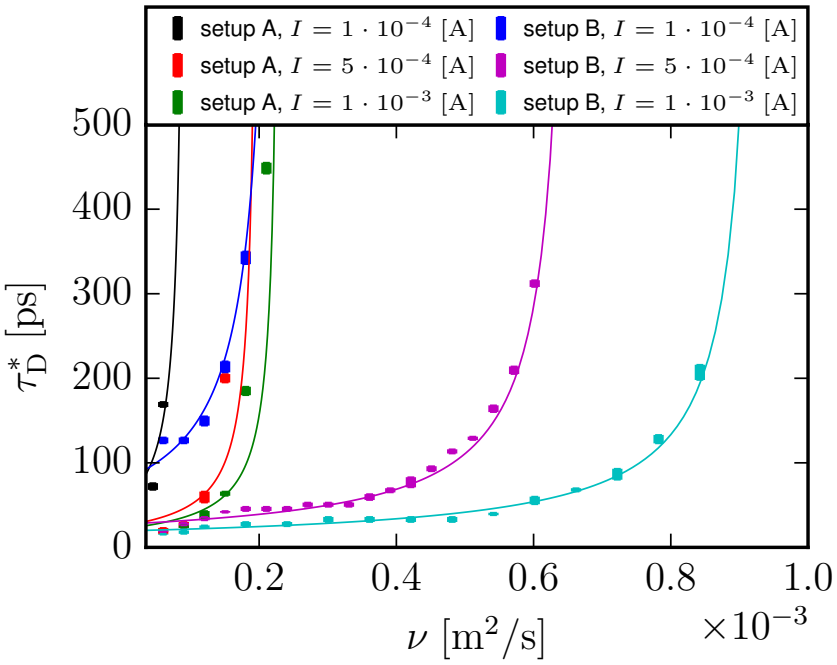

Figure 3.10: *Critical value τ_D^* of the electron-phonon scattering time as a function of the kinematic viscosity ν, for which a transition from a laminar to a preturbulent regime is observed. Thick vertical bars represent results of numerical simulations, for a given geometrical setup (see Fig. 3.5) and given value of the injected current. Lines represent iso-Reynolds curves, where Re' is modified Reynolds number (defined in Eq. (3.11) that includes extrinsic dissipation due to τ_D and ℓ is a fitting parameter. All simulations use $C_g/e^2 = 3.03 \cdot 10^{35}$ J^{-1}m^{-2}.*

capture the trend of the different datasets. In Eq. (3.11), we use the inlet velocity and obtain $\ell_A = 0.085$ μm and $\ell_B = 0.135$ μm through a linear fit, respectively for the two setups in Fig. 3.5. Note that these values are quite close to the typical geometrical features of the simulated layouts.

We obtain the following estimates for the critical modified Reynolds numbers: i) For setup A, $\mathrm{Re}' \sim 25$ with $I = 10^{-4}$ A, $\mathrm{Re}' \sim 58$ with $I = 5 \cdot 10^{-4}$ A and $\mathrm{Re}' \sim 99$ with $I = 10^{-3}$ A. ii) For setup B, $\mathrm{Re}' \sim 19$ with $I = 10^{-4}$ A, $\mathrm{Re}' \sim 33$ with $I = 5 \cdot 10^{-4}$ A and $\mathrm{Re}' \sim 47$ with $I = 10^{-3}$ A.

One further aspect to be evaluated is the effect of the self-consistent electric field (see Eq. 3.2). The geometrical capacitance, introduce in Eq. 3.3, can be defined as

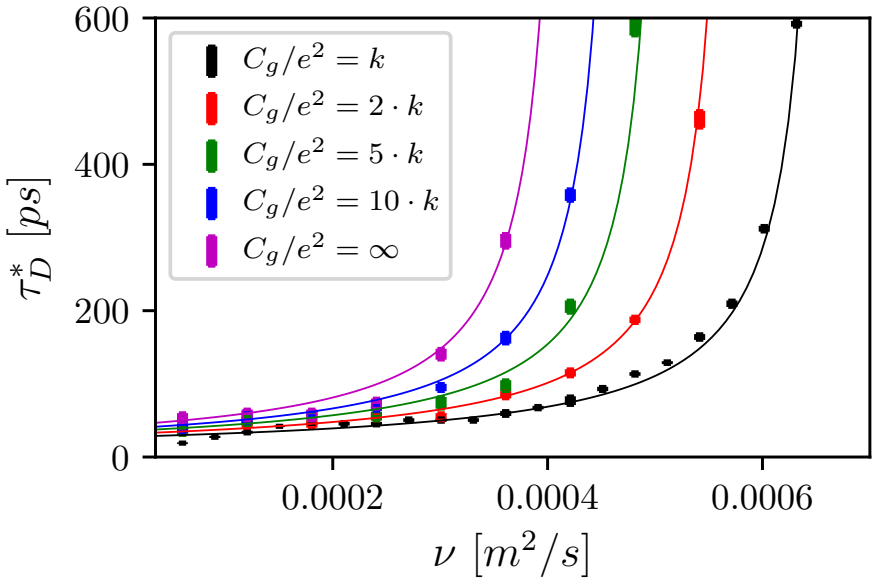

Figure 3.11: *Critical value τ_{D}^* of the electron-phonon scattering time as a function of the kinematic viscosity ν, for which a transition from a laminar to a preturbulent regime is observed. Thick vertical bars represent results of numerical simulations, using the geometry in Fig. 3.5b, a injected current of $I = 5 \cdot 10^{-4}$[A], and for various values of C_{g}/e^2 with respect to the reference value $k = 3.03 \cdot 10^{35}$ $\mathrm{J}^{-1}\mathrm{m}^{-2}$. Lines represent iso-Reynolds curves, where Re' as in Eq. (3.11) is used in the definition of a Reynolds number that includes extrinsic dissipation due to τ_{D} and ℓ is a fitting parameter. We have respectively $\mathrm{Re}' = 33$ for $C_{\mathrm{g}}/e^2 = k$, $\mathrm{Re}' = 38$ for $C_{\mathrm{g}}/e^2 = 2k$, $\mathrm{Re}' = 42$ for $C_{\mathrm{g}}/e^2 = 5k$, $\mathrm{Re}' = 46$ for $C_{\mathrm{g}}/e^2 = 10k$, and $\mathrm{Re}' = 52$ for $C_{\mathrm{g}}/e^2 = \infty$.*

$$C_g = \frac{\epsilon_r}{4\pi} \frac{d + d'}{dd'} \quad , \tag{3.12}$$

with ϵ_r the dielectric constant and d and d' the distances between the graphene layer and the top/bottom gates respectively. In Fig. 3.11 we evaluate the role of varying C_g in simulations. Recall that in the previous section we had verified that for laminar steady-state regimes the electric field did not have effect on the system, nor from a qualitative nor quantitative point of view. In this case the picture is rather different. Indeed we observe the fact that the electric field contributes in triggering instabilities, reducing the impact of the electron-phonon scattering. Observe that, as shown in Tab. 3.1, in simulations we use a value for C_g/e^2 one order of magnitude

bigger than that of typical experiments. The reason is due to numerical instabilities that arise when the magnitude of the external force exceeds a certain threshold. While further numerical analysis are desirable to allow to handle more realistic electric fields, we interpret this as a positive in the sense that the results presented in Fig. 3.10 can be thought as a conservative upper bound of where the actual crossover lines could be identified by real experiments.

4

Implementation of LBM codes on modern HPC architectures

Abstract

One key aspect in the success of LBM lies in its simple and regular algorithmic structure, offering a huge amount of exploitable parallelism, and making this class of CFD solvers an ideal target for efficient parallel implementations on modern computer architectures. In this chapter we describe the development of efficient LBM codes on large clusters of both GPUs and multi/many core processors using OpenMP and OpenACC, two programming environment that should allow a reasonable level of code portability on different architectures. We analyze several data layouts which allow to execute one single code on several different computing architectures, still extracting a significantly large fraction of the performance peak of the target architecture.

The numerical results presented in the previous chapters rely on a careful optimization of codes running on large clusters of GPUs. Since the first porting a LBM code on a GPU [117], extensive efforts have been put in place to optimize LBM codes for several diverse architectures. Not only, the amenability of LBM for parallel implementations has come to an extent where LBM codes are often used as benchmark for the performance of novel architectures [118–122], novel programming techniques [123, 124], as

well as energy efficiency of modern high-performance computing (HPC) architectures [125–127].

In the coming sections we will summarize a few of the best practice in the implementation of LBM codes for heterogeneous HPC clusters. We shall stress here that RLBM algorithms present the same computational features of standard LBM codes. Therefore, while what follows directly apply to RLBM codes as well, we will base our discussion on a classic LBM solver. We use as a test case a thermal LBM [115, 116], which has been used to conduct systematic analyses of several properties of convective turbulence [128–131].

	2D LBM	2D RLBM ($\zeta = 5$)	3D RLBM ($\zeta = 5$)
Stencil vectors	37	45	143
FLOPS/site	6420	$\sim$ 66000	$\sim$ 210000
Arithmetic intensity	11	92	92
Collide MLUPS	108	55	14
Collide TFLOPS ($\mathcal{E}_c$ %)	0.7 (15 %)	3.7 (70 %)	3.1 (60 %)

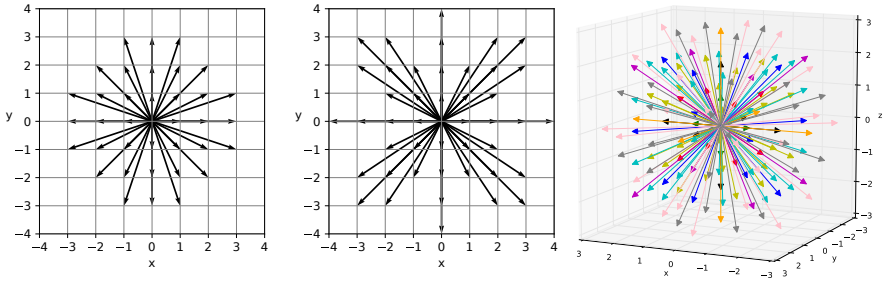

Table 4.1: *Overview of the performances achieved on a NVIDIA Pascal P100 GPU with LBM and RLBM code in 2 and 3 dimensions. The stencils used by each solver are shown in the figure. We report the number of floating point operations (FLOP) required to update a grid point, the arithmetic intensity and the performance of the collide kernel, expressed both in MLUPS (Million Lattice Updates per Second) and TFLOP per second. The metric $\mathcal{E}_c$ gives an estimate of the GPU sustained performance peak.*

In Tab 4.1 we collect a few figures of merit regarding the performances of LBM and RLBM codes in 2 and 3 dimensions on a recent NVIDIA Pascal GPU. We can appreciate that while the RLBM code is much more demanding from a computational point of view, with respect to the thermal LBM, requiring over one order of magnitude more floating point operations to update a grid point, it also has a much higher arithmetic intensity (defined as the ratio of total floating-point operations to total data movement), a

feature that helps sustaining a higher fraction of the performance peak of the target architecture.

The main aspects that will be discussed in this chapter are: i) portability across several architectures using directive based programming frameworks such as OpenMP and OpenACC; ii) memory layouts and data-structures and the role that they play in order to maximize performance portability by enhancing support for vectorization and an effective use of caches; iii) performance scaling of codes on large HPC clusters using standard MPI communication techniques.

4.1 Trends in HPC: heterogeneous architectures

HPC systems are more and more often based on accelerators. While the use of processors specialized in computing different type of workloads has been a long time active research topic [132–134], it is not since the last decade, with the breakthrough of general-purpose GPU computing, that the use of accelerators in HPC has enjoyed a widespread adoption.

More than one out of four of the systems in the most recent (November, 2018) Top500 list [135] uses accelerator/co-processor technologies. These systems deliver a compounded performance of 585 PFLOPS, which is more than 40% of the overall aggregate performance (1.41 EFLOPS) provided by all listed systems. Almost all of these systems consist of large clusters of either GPUs from NVIDIA and AMD, or many-core co-processors from Intel.

State-of-the-art GPUs consist of $\mathcal{O}(1000)$ simple cores organized in warps of threads which execute the same instruction at the same time. On the other hand, Intel accelerators, known as Xeon Phi, offer a fewer number of cores (see Tab. 4.2) compared to GPUs, still with a major increase when comparing with regular Xeon processors. The cores of the Xeon Phi are significantly simpler low-power version of their Xeon counterpart Nevertheless, they are capable of providing a much larger degree of concurrency thanks to enhanced hardware multi-threading, which allows the execution of up to four threads per core, and wider vector units, supporting up to 512-bit SIMD (Single Instruction Multi Data) instructions. With respect to GPUs, these processors rely much more on large cache memories: for example the latest Knights Landing architecture has a 32 MB Last-level-cache, to be compared with the 4 MB of a NVIDIA Pascal GPU.

One key factor in the success of accelerators is power efficiency. This aspect has played a major role in the recent evolution of processor technologies: the trend is apparent when looking, for example, at the latest (November, 2018) Green500 [136] list where the top 25 entries are dominated by accelerator-based systems. In Fig. 4.1 we summarize performance

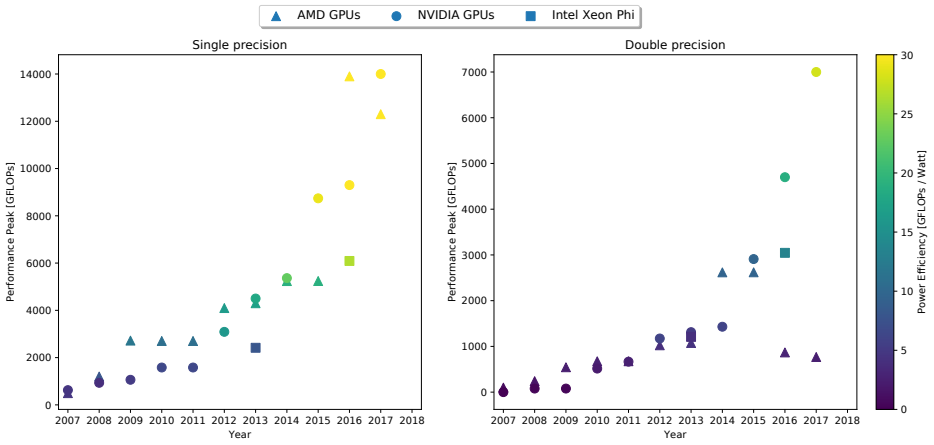

Figure 4.1: *Performance and efficiency trends for accelerators from AMD, NVIDIA, Intel. Dots give the performance peak for single and double precision operations, expressed in GFLOPs (Giga Floating point operations per second). Colors map the power efficiency of each single device, in terms of GFLOPs per Watt.*

and energy efficiency trends of accelerators in the last decade. The pictures show the performance peak for single and double precision operations, expressed in GFLOPs (Giga Floating point operations per second). Colors map the power efficiency of each single device, in terms of GFLOPs per Watt.

Another advantage offered by accelerator-based architectures is a significantly higher memory bandwidth when comparing against CPU-based processors, about one order of magnitude larger. On the other hand, the amount of memory available on the accelerator tends to be rather limited. Applications requiring large amount of memory can still execute on the accelerator via buffered memory transfers from/to the host. However, memory transfers between accelerator and host are a major bottleneck for several applications, due to the low bandwidth offered by the PCI express interface connecting the two. To overcome this problem in recent years there has been a general trend in developing architectures with a more tight integration between host and accelerator; an example is the OpenPOWER architecture which integrates IBM processors with NVIDIA Pascal GPUs.

	Intel Haswell	Intel KNC	Intel KNL	AMD Hawaii	NVIDIA K80	NVIDIA P100
#physical-cores	8	61	64	44	2 × 13 SMX	56
#logical-cores	16	244	256	2816	2 × 2496	3584
Clock (GHz)	2.4	1.238	1.3	0.930	0.560	1.328
Peak perf. (DP/SP GFLOPS)	307/614	1208/2416	2662/5324	2620/5240	2910/8740	4700/9300
SIMD unit width	256-bit	512-bit	512-bit	–	–	–
LL cache (MB)	20	30.5	32	1.00	1.68	4
#Mem. Channels	4	16	16 (6)	–	–	–
Max Memory (GB)	768	16	16 (384)	16	2 × 12	16
Mem BW (GB/s)	59	352	450 (115)	320	2 × 240	732

Table 4.2: *Selected hardware features of the systems tested in this work. We use a Xeon E5-2630 processor to test the Intel Haswell micro-architecture, a Xeon-Phi 7120P for the Knights Corner (KNC), a Xeon-Phi 7230 for the Knights Landing (KNL). The AMD Hawaii taken into consideration is a FirePro W9100 GPU, while the NVIDIA K80 is a NVIDIA GPU with two Tesla GK210 accelerators. Finally, the NVIDIA P100 is a Pascal GP100 GPU.*

A more radical approach was taken by Intel with their latest accelerator, the Knights Landing architecture, consisting of a standalone many-core processor. Although the development of future generations of Xeon Phi has been discontinued, the technological knowhow of these devices will be transferred to future multi-core architectures. In Tab. 4.2 we summarize the most relevant features of a few selected architectures that will be evaluated in the coming sections.

4.1.1 Programming accelerators: directive based models

Two important issues of accelerator-based heterogeneous computing are programmability and portability across diverse architectures. The complexities introduced by heterogeneous architectures motivate new programming models to facilitate the expression of the degree of concurrency of an application. Programming frameworks for accelerator-based systems range from low-level models such as proprietary CUDA from NVIDIA and the open standard OpenCL, to higher-level directive-based models such as OpenMP and OpenACC. Directive-based models represent an appealing solution, promising to reduce the cost of development and ensuring portability of the code. Among these, OpenACC is considered today one of the most promising approaches [137]; its structure is in many ways similar to OpenMP [138]: both frameworks are directive based but, while OpenMP is more prescriptive, OpenACC is more descriptive. OpenACC defines an abstract model for accelerated computing, designed to support offloading of both computation and data from a host to an accelerator device. In Fig 4.2 we show a diagram of the model where host and accelerator are

assumed to have two different memory spaces. The model is host-centric in the sense that the host controls the offloading of code regions and data to the accelerator. The accelerator consists of a set of processing elements (PEs) organized in a SIMD unit allowing (asynchronous) processing of tasks from one or more execution queue. The compiler will implicitly map each component of the OpenACC abstract model into the structure of the target architecture. The task of the programmer is to specify which portions of code (loops / functions) should be executed in parallel on the accelerator, while the appropriate mapping to the target architecture is left to the compiler. This approach gives more freedom to the compiler and the associated runtime support, offering, at least in principle, larger scope for performance portability.

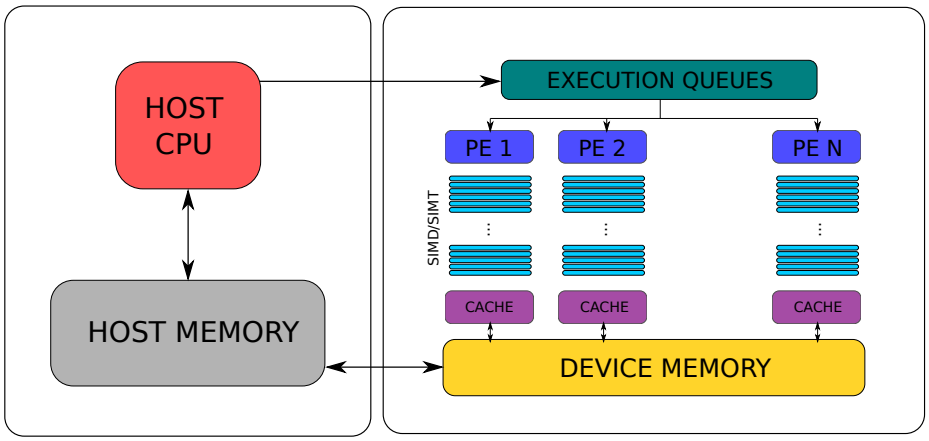

Figure 4.2: *OpenACC abstract model for heterogeneous computing. The host and the accelerator are assumed to have two different memory spaces. The accelerator consists of a set of processing elements (PEs) organized in a SIMD unit allowing (asynchronous) processing of tasks from one or more execution queue.*

Similarly to OpenACC, recent versions of OpenMP also provide support for accelerators, but this feature is still immature. For this reason in the coming sections we will use OpenMP in a rather standard approach, limiting its use for the parallelization and vectorization of codes on multi/many core architectures. OpenACC will be instead the preferred choice for GPUs.

4.2 Optimization of LBM codes

Starting from Eq. 2.12 we can conceptually decompose the evolution of the discrete lattice Boltzmann equation in two steps: the collision step,

$$\hat{f}_i(\boldsymbol{x}, \boldsymbol{e}_i, t) = f_i(\boldsymbol{x}, \boldsymbol{e}_i, t) + \frac{\Delta t}{\tau}\left(f^{eq}_{iN}(\boldsymbol{x}, \boldsymbol{e}_i, t) - f_i(\boldsymbol{x}, \boldsymbol{e}_i, t)\right) \quad , \tag{4.1}$$

and the propagate step,

$$f_i(\boldsymbol{x} + \boldsymbol{e}_i \Delta t, \boldsymbol{e}_i, t + \Delta t) = \hat{f}_i(\boldsymbol{x}, \boldsymbol{e}_i, t) \quad . \tag{4.2}$$

The collide kernel performs all the mathematical operations required to implement the collisional operator. For the specific LBM model taken into consideration, updating a single grid cell requires about 6400 floating point operations. On the other hand, the propagate kernel consists only of memory operations, which in accordance with the stencil rules move the pseudo-particles associated to each grid cell to neighboring sites. The propagate step introduces data dependencies between pairing grid sites. A standard approach to deal with this problem is to keep in memory two copies of the grid, which are used as source and destination in an alternate way at each time step. We make use of this technique, known as double-buffering or "A-B" pattern, to remove data dependencies, allowing the processing of all sites in parallel. There are also other schemes available in the literatures implementing in-place operations [139–141], which can be used to reduce memory requirements.

Another major difference between collide and propagate kernel is that while the collision step is completely local, the propagate involves sparse memory accesses: these conflicting computational requirements need to be taken into account in order to define an efficient data layout used to store the data in memory.

4.2.1 Data Layout

Data layouts for LBM, and likewise for many other stencil applications, have been traditionally based on either *array of structures* (AoS) or *structure of arrays* (SoA) schemes. Recently, slightly more complex data layouts for LBM codes have been introduced [142, 143], with a detailed performance analysis reported in [144].

We start taking into consideration the AoS and SoA schemes, of which a visual representation is given in Fig. 4.3. In the AoS layout, all the pseudo-particles (or populations) belonging to the same lattice site are

stored at consecutive memory locations. Conversely, in the SoA scheme

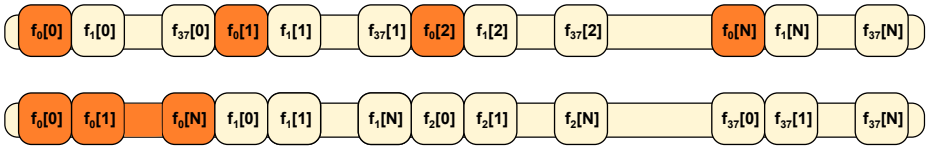

Figure 4.3: *Graphic representation of the AoS and SoA layout.*

all the populations having the same index i are stored contiguously, while populations belonging to the same lattice site are stored far from each other at non unit-stride addresses. The benefit of the AoS scheme is data locality, making it more suitable for exploiting the various cache hierarchies present in standard multi/many core processors. On the other hand, the SoA layout is more suitable for exploiting vector units as well as SIMT (Single Instruction Multi Thread) executions on GPUs architectures.

The first two rows of Tab. 4.3 compare the performance of the two layouts on a few selected architectures. Performance is measured in *MiLlion Updates per Second* (MLUPS), a common metric for this class of applications. As we can see, the SoA layout provides better performances not only on GPUs, but also on cache-based processor. The reason is that the AoS layout implies several misaligned load and store operations which prevent the compiler from vectorizing the code. However, by carefully profiling the code we observe that the AoS scheme exploits the cache of Intel processors significantly better than the SoA layout, suggesting that further improvements could be put in place. Therefore, following [143], we introduce a hybrid data structure with the aim to preserve the benefits of both the AoS and the SoA layouts. With respect to [143] we introduce a slightly modification in order to make the code more suitable for auto-vectorization. For each array of pseudo-particles, we divide each grid-column in partitions of size LY / VL; all elements sitting at the i-th position of each partition are then packed together into "clusters" of VL elements. The parameter VL is an integer multiple of the vector width of the underling architecture. Fig. 4.4 gives a visual representation of this layout that we call layout *Clustered Array of Structure of Array* (CAoSoA). This data layout allows vectorization of inner structures of size VL, and, at the same time, improves data locality w.r.t to the SoA layout. In Tab. 4.3 we compare the performances of propagate and collide employing all the data-layouts discussed so far, for a variety of different architectures. As we can see, the CAoSoA improves performances for the collide kernel on Intel processors, better suiting their larger and deeper cache hierarchies, while on GPUs

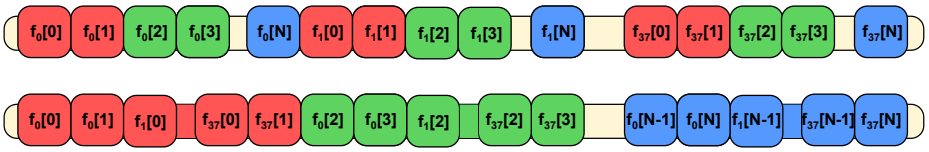

Figure 4.4: *Graphic representation of the CAoSoA layout; for illustration purposes, we take VL=2 and compare with the SoA layout.*

we observe only marginal differences in performance. This data layout has been employed to write a common code capable of executing efficiently on a broad range of parallel architectures. The code was written using OpenMP and OpenACC. A much more detailed description on the implementation of this portable code can be found in [124] and [144]; here we hide most of the technicalities and only provide a small example of code: in Fig. 4.5 we show a section of the collide kernel where for each grid point the density is computed. In the left and right panel we compare the implementation based on OpenMP and OpenACC respectively.

4.2.2 Multi-node implementation

In most heterogeneous computing systems, accelerators cannot handle data transfers, so inter node communications need to be controlled by the host-CPU. Transfers between host and accelerator introduce extra overheads that need to be taken into account when developing efficient multi-node programs, with the ultimate goal of hiding as much as possible these costs

Data Structure	Haswell	KNC	KNL	Tesla K80	AMD Hawaii	P100
			propagate			
AoS	43	91	174	54	27	141
SoA	71	226	732	552	393	753
CAoSoA	61	198	710	536	353	894
			collide			
AoS	14	28	113	23	7	54
SoA	18	39	134	107	39	108
CAoSoA	21	54	165	106	44	105

Table 4.3: *Performance in MLUPS for the propagate and collide kernels on several architectures using different data-layouts. The size of the lattice is* 2160×8192 *points. For the K80 we report the results obtained running on just one of the two GK210 GPUs.*

```
#pragma omp parallel for
for(ix = STARTX; ix < ENDX; ix++ ){
  #pragma omp simd
  for(iy = STARTY; iy < ENDY; iy++ ){
    size_t idx = IDX(ix, iy);

    data_t rho = 0.0;

    for(ip = 0; ip < NPOP; ip++)
      rho = rho + f[idx].p[ip];
  }
}
```

```
#pragma acc kernels present(f)
#pragma acc loop gang independent
for(ix = STARTX; ix < ENDX; ix++ ){
  #pragma acc loop vector independent
  for(iy = STARTY; iy < ENDY; iy++ ){
    size_t idx = IDX(ix, iy);

    data_t rho = 0.0;
    #pragma acc loop seq reduction(+:rho)
    for(ip = 0; ip < NPOP; ip++)
      rho = rho + f[idx].p[ip];
  }
}
```

Figure 4.5: *Sample code for the collide kernel showing the computation of the local density. The example is shown for the OpenMP (left) and OpenACC (right) implementation.*

by overlapping computation and communications.

In this section we will compare two different approaches, implemented using MPI. To start, we associate one MPI-process to each accelerator and consider a 1D decomposition. The MPI-processes are therefore arranged in a ring topology, in which each node i exchanges data with its neighbors $i-1$ and $i+1$.

Asymmetric workload distribution

In this first case we assume that all the computation is performed on the accelerator, with the role of the host processor restricted, for the moment, to the handling of communications. We conveniently divide the lattice in three regions: a bulk central region and two boundary regions containing the data that needs to be exchanged with the neighboring sites. The algorithm implementing this strategy is rather simple. At each time step the boundary regions are copied from the device memory to a buffer in the host memory. At this stage data can be sent to the neighboring nodes by means of MPI communications and written on a destination buffer. Finally, the data is transferred back to the device and written in the lattice halo layer. While this procedure takes place, the bulk region can be processed asynchronously on the accelerator. On the other hand, processing of the boundary regions can take place only after left and right halos have been received. A possible scheduling of these operations in sketched in the timeline in Fig. 4.6.

The drawback of this approach is that it only marginally exploits the computational resources available on the host CPUs, limiting overall

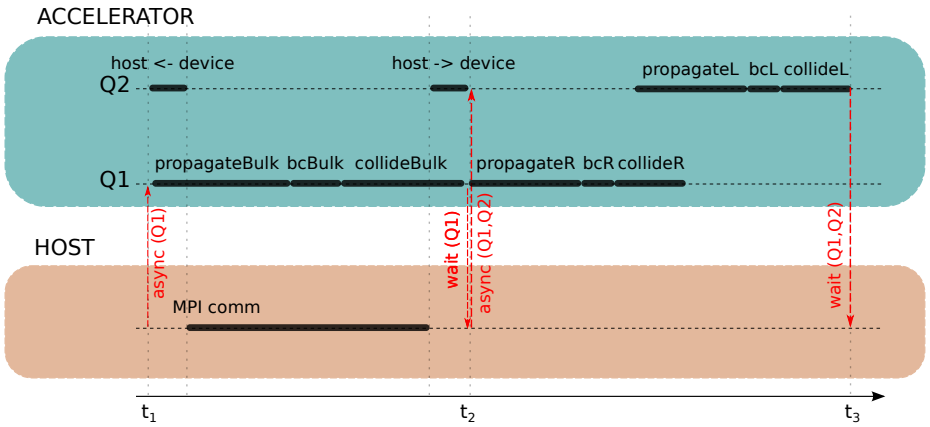

Figure 4.6: *Scheduling of operations for an asymmetric workload distribution, where all the computation is performed on the accelerator, while the host is only responsible for MPI communications.*

performances. The obvious step forward is to run compute-intensive kernels in a concurrent and balanced way on both hosts and accelerators.

Symmetric workload distribution

We again consider a 1D partitioning, where each slice of the lattice is assigned to a different MPI-process. Within each MPI-process, each partition is further divided between host and accelerator. We define again three regions, but this time the M leftmost and the M rightmost columns are assigned to the host CPUs, with the remaining $SIZEX$ - $2M$ assigned to the accelerator. Computation is performed asynchronously on both host and accelerator, with a possible scheduling of the operations executed by each MPI-process shown in Fig. 4.7. With respect to the previous implementation, data involved in MPI communications is always resident on the host, thus avoiding dependencies between MPI and device-to-host and host-to-device data transfers.

Since host and accelerator generally have different peak (and sustained) performance, a careful workload balancing between the two is required. To this aim we introduce a simple model for the total execution time T_{exe}:

$$T_{\text{exe}} = \max\{T_{\text{acc}}, T_{\text{host}} + T_{\text{mpi}}\} + T_{\text{swap}} \tag{4.3}$$

$$T_{\text{acc}} = (LX - 2M)LY \cdot \tau_d \tag{4.4}$$

$$T_{\text{host}} = (2M)LY \cdot \tau_h \tag{4.5}$$

$$T_{\text{mpi}} = \tau_c \tag{4.6}$$

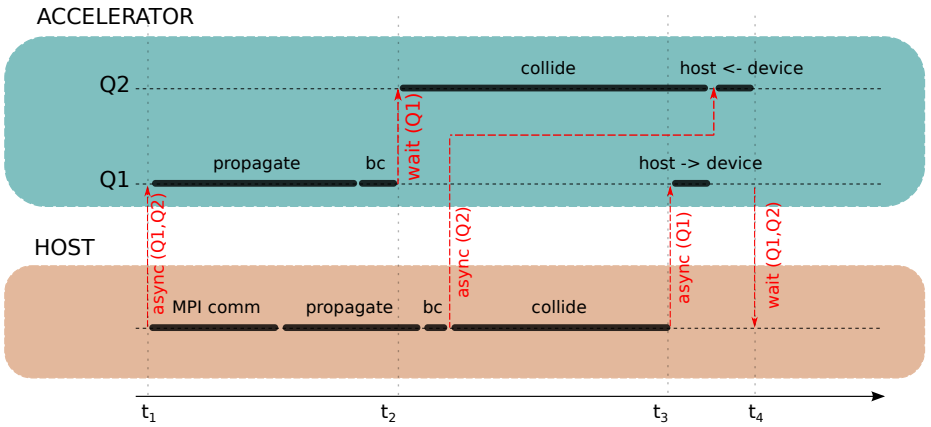

Figure 4.7: *Scheduling of operations for a symmetric workload distribution, where computation is performed in a concurrent (and balanced) way on both hosts and accelerators.*

where T_{acc} and T_{host} are the execution time of the accelerator and host respectively, T_{swap} is the time required to exchange data between host and accelerator at the end of each iteration, and T_{mpi} is the time necessary to move data between two MPI-processes. As T_{swap} does not depend on M, T_{exe} is minimal for a value M^* for which the following holds:

$$T_{\text{acc}}(M^*) = T_{\text{host}}(M^*) + T_{\text{mpi}}(M^*) \quad , \tag{4.7}$$

We add in the code an initial auto-tuning phase, in which we run a set of mini-benchmarks to estimate approximate values of τ_d, τ_h, τ_c. These are then used in Eq.4.7 to estimate M^*.

In Fig. 4.8 we show the performance of our code for three different lattice sizes as a function of $2M/LX$, i.e. the fraction of lattice sites that we map on the host CPU. For this benchmark we have considered three different systems, all using the same 8-core Intel Haswell as host device, combined with three different accelerators, respectively a Intel KNC, a NVIDIA K80 GPU, and a AMD Hawaii GPU. In Fig. 4.8 dots report measured values, while dotted lines represent the modeling provided by Eq. 4.3. Our auto-tuning strategy predicts performance with good accuracy, and estimates the optimal workload distribution between host and device for which the overall execution time is minimized. As expected, for values of $M < M^*$ and $M > M^*$ performances decrease because the workload is unbalanced either on the accelerator or on the host side. In particular it is interesting to observe that, as M becomes much larger than M^*, all lines in the plot fall on top of each other, as in this limit the host CPU handles

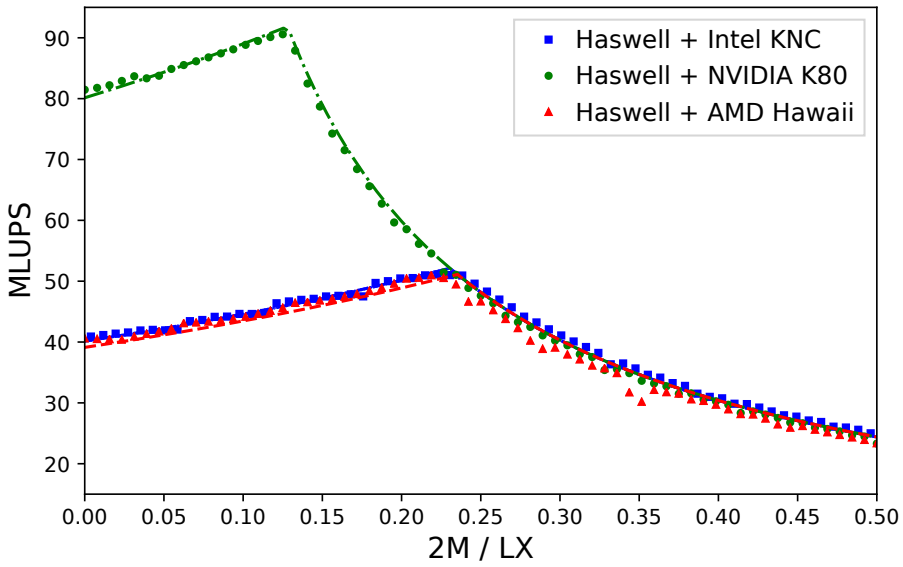

Figure 4.8: *Performance of the heterogeneous code (measured in MLUPS, see the text for definition) for all three platforms, as a function of the fraction of lattice sites mapped on the Haswell (HSW) host CPU ($2M/L_x$) . KNC is the Intel Knights Corner accelerator, K80 is the NVIDIA Tesla GPU and Hawaii is the FirePro W9100 AMD GPU (refer to Tab 4.2 for more details). Dots are measured values, dashed lines are the prediction of our model.*

the largest part of the overall computation.

In Fig. 4.9 we show a comparison of the performance and the scaling performance between two different implementations running on a cluster of Intel KNC and one based on NVIDIA K80 GPUs. The results clearly show that the heterogeneous implementation offer significant improvements both in terms of absolute performance, both in terms of scalability.

We conclude this chapter giving a summary of the performance obtained with a portable implementation of a thermal LBM code on a wide range of diverse parallel architectures, presented in Tab 4.4. We once again remark that the lessons learned in the optimization of LBM codes directly apply to the RLBM, and have allowed to perform the extensive numerical work described in previous chapters.

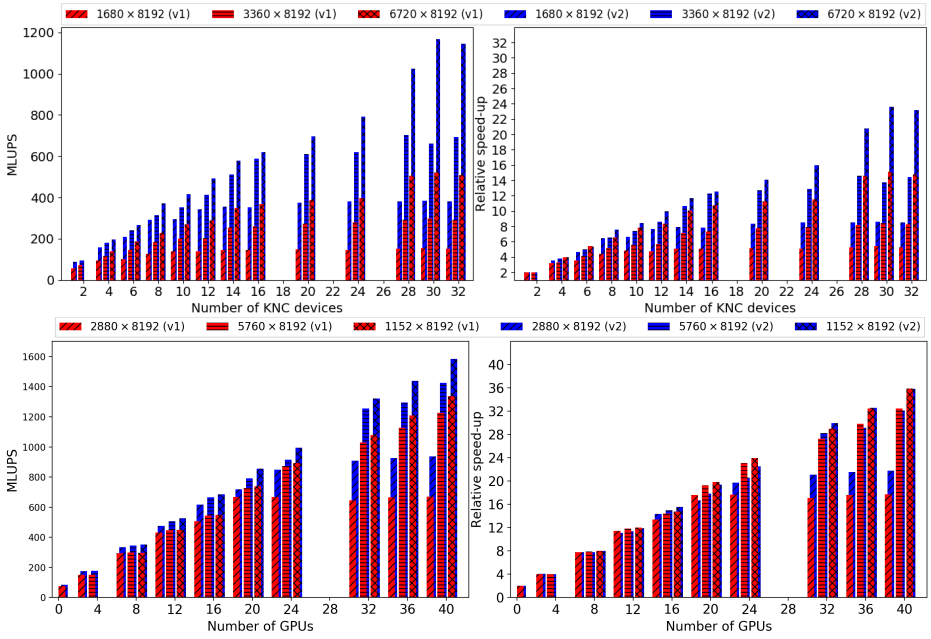

Figure 4.9: *Multi-node scalability results measured on a cluster of Intel KNC (top) and NVIDIA K80 (bottom). We compare performances – MLUPS and relative speedup – on three different lattice sizes of the heterogeneous code described in the text: we denote with (v1) the asymmetric implementation where all the computational is performed on accelerators only, while (v2) refers to the implementation of a symmetric workload distribution between host and accelerator.*

Table 4.4: *Comparison of the performance achieved on several different architectures (details in Tab 4.2). We report the performance of the propagate and collide kernels as well as those of the full code (Global), using the CAoSoA data layout.*

	Intel Haswell	Intel KNC	Intel KNL	AMD Hawaii	NVIDIA K80	NVIDIA P100
Propagate [GB/s]	32	100	398	216	310	485
$\mathcal{E}_p$	54%	28%	88%	70%	65%	66%
Collide [GF/s]	78	307	1100	351	1371	703
Collide [MLUPS]	12	46	166	54	211	108
$\mathcal{E}_c$	22%	25%	41%	14%	46%	15%
Global [MLUPS]	9.8	35	119	47	168	90

Conclusions and Outlook

In this thesis work we have described the development of a class of relativistic lattice Boltzmann methods, suitable for the description of mildly relativistic fluids. We have significantly extended the range of possible physical applications over previous works, which were bounded to the description of fluids of pseudo-particles of zero proper mass, implying ultra-relativistic equations of state. Our model offers the possibility of seamlessly bridging the gap between relativistic and low-speed non-relativistic fluid regimes, also including appropriate equations of state.

We shall here summarize the main results presented in this thesis. For the sake of clarity we have grouped them in four thematic areas:

(1) Algorithmic derivation.

- We have explicitly built a new class of RLBM based on massive pseudo-particles, able to recover the moments of the relativistic equilibrium distribution up to the fifth order, in $(3+1)$, $(2+1)$ as well as $(1+1)$ dimensions.
- The use of massive pseudo-particles translates into the possibility of working in a specific relativistic range of velocities of the simulated system, ranging from strongly relativistic to almost classical.
- The derivation is based on Gauss-type quadratures on space-filling Cartesian lattices, allowing the use of different sets of pseudo-particles, and implementing exact streaming without losing spatial resolution.
- The algorithmic structure is very similar to that of other well established LBM, and retains the same computational advantages,

offering high amenability to parallelization.

(2) Study of the relativistic transport coefficients in the relaxation time approximation.

- We have presented numerical evidence that the Chapman Enskog expansion accurately relates kinetic transport coefficients and macroscopic hydrodynamic parameters in dissipative relativistic fluid dynamics, confirming recent theoretical results.
- Since the transport coefficients in the RTA do not necessarily coincide with those of the full Boltzmann equation, these results cannot be considered conclusive. Nevertheless they provide a solid calibration procedure which is used to control the transport coefficients in our simulations; based on this we have provided simulations of the Riemann problem for a quark-gluon plasma, showing good agreement with results obtained using other solvers present in the literature. These results suggest that RLBM can be used to accurately simulate realistic physics systems.

(3) Study of the transport properties of a electronic fluid in graphene samples, in both laminar and unsteady regimes.

- As an example of application, we have presented simulations of laminar flows in ultra-clean graphene samples, taking into consideration geometrical setups used in actual experiments. We have given numerical evidence of the formation of electron back-flows (whirlpools) in the proximity of current injectors.
- We have considered electronic systems where nonlinear effects start becoming relevant. We have presented realistic simulations, accounting for electrostatic interactions and dissipative electron-phonon scattering, and proposed experimentally realizable geometries capable of sustaining electronic preturbulence in graphene samples.
- We have identified transport parameters for which preturbulent signals occur at experimentally achievable values of the Reynolds number and manifest through temporal fluctuations of the electrochemical potential.
- We have characterized the crossover from a laminar to a preturbulent regime by introducing a modified definition for the

Reynolds number, by accounting for the interaction of electrons with phonons and impurities.

(4) Computational aspects.

- We have developed and optimized LBM solvers on large clusters of both GPUs and multi/many core processors.
- We have investigated aspects related to code portability and performance portability on modern heterogeneous architectures using directive based programming languages such as OpenMP and OpenACC.
- We have developed data layouts which guarantee at the same time efficient memory accesses and vector processing, allowing performance-portability on different accelerator architectures.
- We have shown how to run compute-intensive kernels in a concurrent and balanced way on both hosts and accelerators; this in turn has allowed better exploitation of computational resources available on modern heterogeneous architectures, also helping improving the inter node scalability performances.

All these results can be used as a solid starting point for future works. Several algorithmic aspects can be improved. For example, much needed developments concern the definition of accurate boundary conditions for RLBM. Moreover, it is desirable to get better control on instabilities occurring for simulations of supersonic flows, which can be obtained introducing formulations based on entropic stabilizers.

These improvements are expected to help the development of reliable simulations for the physical analysis of hydrodynamic properties of quark-gluon plasma produced in heavy-ion collision experiments. Another ideal target of future works will be the extension of the hydrodynamic approach for the study of electronic fluids, as was here discussed for the case of graphene, to other exotic materials such as Weyl semi-metals.

Appendices

A

Special Relativity

Abstract

In this appendix chapter we provide a brief introduction to the theory of special relativity, the Lorentz transformations and the basics of relativistic mechanics. We introduce the notation used throughout this thesis work for tensor analysis in Minkowski space, and give a list of definitions of relativistic counterpart of Newtonian physical quantities such as velocity, momentum, force and energy, used in the description of relativistic fluids. Contents and structure closely follow the introductory chapter in [8]. For a more thorough introduction to special relativity the reader is refereed to e.g. [145].

The theory of special relativity was formulated by Albert Einstein in 1905 [146] in order to resolve the conflict between Newtonian mechanics and Maxwell's equations. It is based on two postulates:

- The laws of physics are invariant in all inertial (i.e. non-accelerating) frames of reference.
- The value of the speed of light in free space is the same for all observers that are in inertial frames.

The first postulate states that the physical laws are the same for all inertial frames, and therefore they are invariant with respect to space-time transformations between inertial systems. From the second postulate it follows that the velocity of a light signal propagating in vacuum is a

universal constant: c = 299792458 m/s. As a consequence time intervals are not absolute, for example the time interval between two events as measured by a moving observer is not the same as the one measured by an observer at rest.

A.1 Minkowski space

The Minkowski space-time is a parametrization of time and the three-dimensional Euclidean space, defined such that the interval between two events is independent of the reference frame used for the observation. The coordinates in the four-dimensional Minkowski space are described by the vector (x^α) with its coordinates defined by:

$$\begin{aligned} x^0 &= ct \quad , \\ x^1 &= x \quad , \\ x^2 &= y \quad , \\ x^3 &= z \quad . \end{aligned} \tag{A.1}$$

A four-vector (A^α) can be represented either through its contravariant A^α or covariant components A_α. The metric tensor, here defined as

$$(\eta_{\alpha\beta}) = \begin{pmatrix} +1 & 0 & 0 & 0 \\ 0 & -1 & 0 & 0 \\ 0 & 0 & -1 & 0 \\ 0 & 0 & 0 & -1 \end{pmatrix} \quad , \tag{A.2}$$

puts in relation these two representations through

$$A_\alpha = \eta_{\alpha\beta} A^\beta \quad \text{and} \quad \mathrm{A}^\alpha = \eta^{\alpha\beta} \mathrm{A}_\beta \quad . \tag{A.3}$$

It is straightforward to verify that the following relations hold:

$$\begin{aligned} \eta_{\alpha\beta} &= \eta^{\alpha\beta} \quad , \\ \eta_{\alpha\beta}\, \eta^{\beta\gamma} &= \delta^\gamma_\alpha \quad , \end{aligned} \tag{A.4}$$

where δ^γ_α is the Kronecker symbol defined by

$$\delta^\gamma_\alpha = \begin{cases} 0 & \text{if} \quad \alpha = \gamma \\ 1 & \text{if} \quad \alpha \neq \gamma \end{cases} \tag{A.5}$$

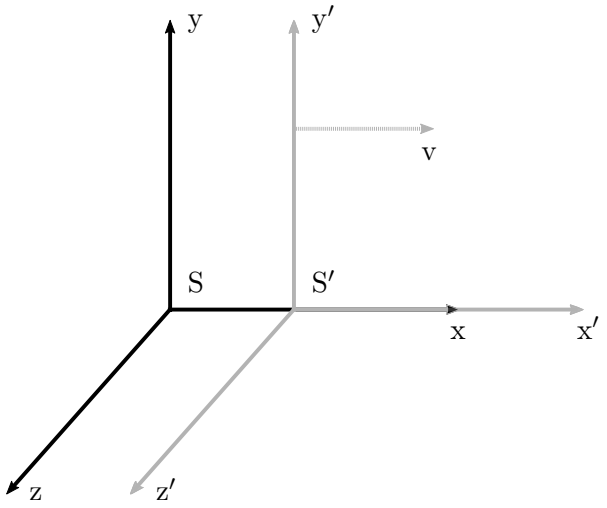

Figure A.1: *Representation of two inertial systems.*

The contravariant and covariant vectors can be also represented as

$$\begin{aligned}(A^\alpha) &= \left(A^0, \quad \boldsymbol{A}\right) \quad , \\ (A_\alpha) &= \left(A_0, -\boldsymbol{A}\right) \quad ,\end{aligned} \tag{A.6}$$

where it is clear that component-wise $A^0 = A_0$ and $A_i = -A^i$. Here and throughout this thesis work we use bold letters to denote Euclidean vectors. The scalar product of two four-vectors (A^α) and (B^α) is defined in the Minkowski space as

$$A^\alpha B_\alpha = A^0 B_0 + A^i B_i = A^0 B_0 - \boldsymbol{A} \cdot \boldsymbol{B}, \tag{A.7}$$

where $\boldsymbol{A} \cdot \boldsymbol{B}$ is the scalar product between two vectors in a three-dimensional space. The gradient $\partial/\partial x^\alpha$ with respect to the covariant coordinates, and the gradient $\partial/\partial x_\alpha$ with respect to the contravariant coordinates, are defined as

$$\begin{aligned}(\partial^\alpha) &= \left(\frac{\partial}{\partial x_\alpha}\right) = \left(\frac{\partial}{\partial x_0}, -\boldsymbol{\nabla}\right) \quad , \\ (\partial_\alpha) &= \left(\frac{\partial}{\partial x^\alpha}\right) = \left(\frac{\partial}{\partial x^0}, \quad \boldsymbol{\nabla}\right) \quad ,\end{aligned} \tag{A.8}$$

with $\boldsymbol{\nabla}$ the usual gradient in three dimensions.

A.2 Lorentz transformation

Consider two reference frames S and S', as shown in Fig. A.1, with S' moving with respect to S with uniform velocity v along the x axis. The infinitesimal interval between two events in the reference frame S is given by

$$\mathrm{d}s^2 = \eta_{\alpha\beta}\,\mathrm{d}x^\alpha\,\mathrm{d}x^\beta = c^2\,\mathrm{d}t^2 - \mathrm{d}x^2 - \mathrm{d}y^2 - \mathrm{d}z^2 \quad . \tag{A.9}$$

It is simple to show, under the assumption of homogeneity of space-time and isotropy of space, that $\mathrm{d}s^2$ is an invariant: the interval between two events is the same in all inertial frame of reference, i.e.

$$\mathrm{d}s^2 = \mathrm{d}s'^2 \quad . \tag{A.10}$$

A Lorentz transformation determines the transformation law between two inertial systems by keeping the interval between two events invariant. Denoting $(\mathcal{L}^\alpha_\beta)$ the transformation matrix between two reference frames we can write

$$x'^\alpha = \mathcal{L}^\alpha_\beta x^\beta \quad . \tag{A.11}$$

The derivation of the transformation matrix is a simple exercise. For the example in Fig. A.1 one gets:

$$\left(\mathcal{L}^\alpha_\beta\right) = \begin{pmatrix} \frac{1}{\sqrt{1-\beta^2}} & \frac{-\beta}{\sqrt{1-\beta^2}} & 0 & 0 \\ \frac{-\beta}{\sqrt{1-\beta^2}} & \frac{1}{\sqrt{1-\beta^2}} & 0 & 0 \\ 0 & 0 & 1 & 0 \\ 0 & 0 & 0 & 1 \end{pmatrix} \quad . \tag{A.12}$$

where $\beta = v/c$. By combining Eq. A.11 and Eq. A.12 one can then obtain the Lorentz transformation from the reference frame S to S':

$$\begin{aligned} ct' &= \frac{ct - \beta x}{\sqrt{1-\beta^2}}, \\ x' &= \frac{x - \beta ct}{\sqrt{1-\beta^2}}, \\ y' &= y, \\ z' &= z. \end{aligned} \tag{A.13}$$

Several important physical implications such as time dilatation, lenght contraction and relativity of simultaneity are steadily derived from Eq. A.13. Moreover, the Galilean transformations can be obtained as a particular

case of the Lorentz transformation when velocities are small relative to the speed of light ($v \ll c$):

$$\begin{aligned} t' &= t, \\ x' &= x - vt, \\ y' &= y, \\ z' &= z. \end{aligned} \tag{A.14}$$

The general transformation law, for two inertial systems in which one is moving with respect to the other with a velocity $\boldsymbol{v} = (v_1, v_2, v_3)$, is given by

$$\left(\mathcal{L}^{\alpha}_{\beta}\right) = \begin{pmatrix} \gamma & -\gamma\frac{v_1}{c} & -\gamma\frac{v_2}{c} & -\gamma\frac{v_3}{c} \\ -\gamma\frac{v_1}{c} & 1+(\gamma-1)\frac{v_1^2}{|\boldsymbol{v}|^2} & (\gamma-1)\frac{v_1 v_2}{|\boldsymbol{v}|^2} & (\gamma-1)\frac{v_1 v_3}{|\boldsymbol{v}|^2} \\ -\gamma\frac{v_2}{c} & (\gamma-1)\frac{v_1 v_2}{|\boldsymbol{v}|^2} & 1+(\gamma-1)\frac{v_2^2}{|\boldsymbol{v}|^2} & (\gamma-1)\frac{v_2 v_3}{|\boldsymbol{v}|^2} \\ -\gamma\frac{v_3}{c} & (\gamma-1)\frac{v_1 v_3}{|\boldsymbol{v}|^2} & (\gamma-1)\frac{v_2 v_3}{|\boldsymbol{v}|^2} & 1+(\gamma-1)\frac{v_3^2}{|\boldsymbol{v}|^2} \end{pmatrix} , \tag{A.15}$$

where γ is the Lorentz factor

$$\gamma = \frac{1}{\sqrt{1-\beta^2}} \quad , \tag{A.16}$$

and $\beta = |\boldsymbol{v}|/c$.

A.3 Relativistic mechanics

Consider a particle moving through space-time. The path of the particle is called *world line* and is represented by means of *world points*. In the previous section we have already discussed the advantage of using four-vectors to represent world points and the infinitesimal displacement ds between two of them. In the following we define the correspondent in special relativity of Newtonian physical quantities that automatically transform correctly under Lorentz transformations.

A.3.3 Proper time

One first convenient definition is the introduction of the concept of *proper time* τ (not to be confused with the relaxation time τ used in the models approximating the collisional operator of the Boltzmann equation). The proper time is the time indicated by a clock moving with the same speed

of the particle. From Eq. A.9 the proper time can be expressed as:

$$\begin{aligned} \mathrm{d}\tau &= \frac{1}{c}\,\mathrm{d}s \\ &= \frac{1}{c}\left(c^2\,\mathrm{d}t^2 - \mathrm{d}x^2 - \mathrm{d}y^2 - \mathrm{d}z^2\right)^{1/2} \\ &= \mathrm{d}t^2\left(1 - \frac{|\boldsymbol{u}|^2}{c^2}\right)^{1/2} \quad , \end{aligned} \tag{A.17}$$

where $\boldsymbol{u}$ is the velocity of the particle in the reference frame of the observer. From Eq. A.17 we see that the proper time is a scalar invariant and that the following useful relation holds:

$$\frac{\mathrm{d}t}{\mathrm{d}\tau} = \gamma \quad . \tag{A.18}$$

A.3.3 Four-velocity

The four-velocity is naturally defined as the rate of change of the four-displacement with respect to the proper time:

$$U^\alpha = \frac{\mathrm{d}x^\alpha}{\mathrm{d}\tau} \quad . \tag{A.19}$$

Geometrically (U^α) is a four-vector tangent to the world line. From the definition, together with Eq. A.18, one can express the components of the four-velocity vector as

$$(U^\alpha) = \left(\frac{\mathrm{d}x^\alpha}{\mathrm{d}\tau}\right) = \left(\frac{\mathrm{d}t}{\mathrm{d}\tau}\frac{\mathrm{d}x^\alpha}{\mathrm{d}t}\right) = \gamma_u\,(c, \boldsymbol{u}) \quad , \tag{A.20}$$

with $\boldsymbol{u} = \mathrm{d}\boldsymbol{x}/\,\mathrm{d}t$ the particle velocity in the reference frame. It follows that the norm of the four-velocity vector in not just Lorentz invariant but also constant, since

$$U^\alpha U_\alpha = c^2 \quad . \tag{A.21}$$

A.3.3 Momentum four-vector and energy

The *proper-mass* (or rest mass) m is, likewise the proper-time, a scalar invariant, allowing for a straightforward definition of the momentum four-vector of a particle:

$$p^\alpha = mU^\alpha \quad . \tag{A.22}$$

The contravariant components of the momentum four-vector are then

$$(p^\alpha) = \gamma_u \, (mc, m\boldsymbol{u}) = \left(\frac{E}{c}, \boldsymbol{p}\right) = \left(p^0, \boldsymbol{p}\right) \quad , \tag{A.23}$$

where the energy of the particle is defined as

$$E = cp^0 = \gamma_u mc^2 \quad . \tag{A.24}$$

The norm of (p^α) is then given by:

$$p^\alpha p_\alpha = \frac{E}{c^2} - \boldsymbol{p}^2 \quad . \tag{A.25}$$

On the other hand, combining the definition in Eq. A.22 together with Eq. A.21 we get:

$$p^\alpha p_\alpha = m^2 U^\alpha U_\alpha = m^2 c^2 \quad . \tag{A.26}$$

Comparing Eq. A.25 and A.26 we obtain the relativistic energy equation :

$$E^2 = \boldsymbol{p}^2 c^2 + m^2 c^4 \quad , \tag{A.27}$$

It is simple to observe that for a particle with zero velocity Eq. A.27 gives the famous Einstein formula $E = mc^2$. Furthermore, for small velocities ($v \ll c$) a second order expansion delivers the classical expression for the kinetic energy of a particle:

$$E_k = E - mc^2 \approx \frac{1}{2} m v^2 \quad . \tag{A.28}$$

As a final observation, note that Eq. A.27 can be used to express p^0 as a function of $\boldsymbol{p}$:

$$p^0 = \sqrt{|\boldsymbol{p}| + m^2 c^2} \quad . \tag{A.29}$$

A.3.3 Minkowski force

The definition of force in relativity is subject to a certain degree of arbitrariness due to the lack of certain general properties such as, for example, Newton's third law. One common choice is to adopt the Minkowski force, defined as

$$K^\alpha = \frac{\mathrm{d}p^\alpha}{\mathrm{d}\tau} = m \frac{\mathrm{d}U^\alpha}{\mathrm{d}\tau} \quad . \tag{A.30}$$

It can be shown that the contravariant components of the Minkowski force are then

$$(K^\alpha) = \gamma \left(\frac{\boldsymbol{F} \cdot \boldsymbol{u}}{c}, \boldsymbol{F} \right) \quad , \tag{A.31}$$

where $\boldsymbol{F} = \mathrm{d}\boldsymbol{p}/\,\mathrm{d}t$ is the non-relativistic force. A consequence of using this definition of force is that the following holds true:

$$K^\alpha U_\alpha = 0 \quad . \tag{A.32}$$

B

Useful integrals

The derivation of the relativistic lattice Boltzmann method presented in this thesis work often requires the calculation of integrals in the form

$$Z^{\alpha\dots\omega} = \int e^{\frac{p^\alpha U_\alpha}{T}} p^\alpha \dots p^\omega \frac{\mathrm{d}p^D}{p^0} \quad , \tag{B.1}$$

having assumed natural units, $c = k_B = \hbar = 1$. An elegant way to compute these integrals was provided in [8] (see section 5.6) and consists in first calculating Z as a function of U^α to then obtain all the other integrals by successive differentiation of Z with respect to U_α. Indeed, one easily finds that

$$Z^{\alpha_1\cdots\alpha_n} = (-1)^n \, T^n \, \frac{\partial^n Z}{\partial U_{\alpha_1} \cdots \partial U_{\alpha_n}} \quad . \tag{B.2}$$

For the calculation of these integrals it is useful to recall the definition and a few properties of the modified Bessel function of the second kind:

$$K_\alpha(\xi) = \int_0^\infty e^{-\xi \cosh t} \cosh \alpha t \, \mathrm{d}t \tag{B.3}$$

$$K_{\alpha+1}(\xi) = K_{\alpha-1}(\xi) + \frac{2\alpha}{\xi} K_\alpha \tag{B.4}$$

$$\frac{\partial K_\alpha(\xi)}{\partial \xi} = \frac{\alpha}{\xi} K_\alpha(\xi) - K_{\alpha+1}(\xi) \quad . \tag{B.5}$$

To give an example we consider the $(1+1)$ dimensional case and start by observing that since Z is a Lorentz-invariant quantity, it can only depend on $U_\alpha U^\alpha$, which is equal to 1; however, since we need to compute derivatives with respect to U^α, we will first derive the result for a generic $U_\alpha U^\alpha$ and only after having performed the derivatives, evaluate the result

for $U_\alpha U^\alpha = 1$. In order to simplify the calculation of the integrals we choose a reference frame where U^0 is the only non-zero component of (U^α). In order to do so, we take a generic Lorentz boost

$$\begin{aligned} U'^0 &= \gamma(U^0 - \lambda U^x) \quad , \\ U'^x &= \gamma(U^x - \lambda U^0) \quad , \end{aligned} \tag{B.6}$$

and require that U'^x is zero, implying $\lambda = U^x/U^0$ and

$$\gamma = \frac{1}{\sqrt{1-(U^x/U^0)^2}} = \frac{U^0}{\sqrt{(U^0)^2-(U^x)^2}} = \frac{U^0}{\sqrt{U_\alpha U^\alpha}} \quad . \tag{B.7}$$

As a consequence we get the following Lorentz transformation

$$\begin{aligned} U'^0 &= \sqrt{U_\alpha U^\alpha} \quad , \\ U'^x &= 0 \quad , \end{aligned} \tag{B.8}$$

which we can apply to the integral Z (recall that $\mathrm{d}p/p^0$ is also a Lorentz invariant) getting

$$Z = \int e^{-\sqrt{U_\alpha U^\alpha}\frac{p^0}{T}} \frac{\mathrm{d}p}{p^0} \quad . \tag{B.9}$$

From the above, using the substitution $p_0 = m\cosh y$ one easily gets:

$$Z = 2\int_0^\infty e^{-\sqrt{U_\alpha U^\alpha}\frac{m}{T}\cosh y}\ \mathrm{d}y = 2K_0(\sqrt{U_\alpha U^\alpha}\frac{m}{T}) \quad . \tag{B.10}$$

To calculate Z^α we take the derivative of Z with respect of U^α:

$$\frac{\partial Z}{\partial U^\alpha} = -2\frac{m}{T}K_1\left(\sqrt{U_\alpha U^\alpha}\frac{m}{T}\right)\frac{U^\alpha}{\sqrt{U_\alpha U^\alpha}} \quad . \tag{B.11}$$

Combining the above result with Eq. B.2 and using $U_\alpha U^\alpha = 1$ we get

$$Z^\alpha = -T\frac{\partial Z}{\partial U^\alpha} = 2mK_1\left(\frac{m}{T}\right)U^\alpha \quad . \tag{B.12}$$

All the other integrals can be obtained by iterating the here described procedure. The full list of results can be expressed in a compact general

form in $(D+1)$-dimensions:

$$
\begin{aligned}
Z &= BA_0 \\
Z^{\alpha} &= BTA_1U^{\alpha} \\
Z^{\alpha\beta} &= BT^2(A_2U^{\alpha}U^{\beta} - A_1\eta^{\alpha\beta}) \\
Z^{\alpha\beta\gamma} &= BT^3(A_3U^{\alpha}U^{\beta}U^{\gamma} - A_2(\eta^{\alpha\beta}U^{\gamma} + \eta^{\alpha\gamma}U^{\beta} + \eta^{\beta\gamma}U^{\alpha})) \\
Z^{\alpha\beta\gamma\delta} &= BT^4(A_4U^{\alpha}U^{\beta}U^{\gamma}U^{\delta} - A_3(\eta^{\alpha\beta}U^{\gamma}U^{\delta} + \eta^{\alpha\gamma}U^{\beta}U^{\delta} + \eta^{\beta\gamma}U^{\alpha}U^{\delta} \\
&\qquad + \eta^{\alpha\delta}U^{\gamma}U^{\beta} + \eta^{\delta\gamma}U^{\beta}U^{\alpha} + \eta^{\beta\delta}U^{\alpha}U^{\gamma}) \\
&\quad + A_2(\eta^{\alpha\beta}\eta^{\gamma\delta} + \eta^{\alpha\gamma}\eta^{\beta\delta} + \eta^{\alpha\delta}\eta^{\beta\gamma})) \\
Z^{\alpha\beta\gamma\delta\epsilon} &= BT^5(A_5U^{\alpha}U^{\beta}U^{\gamma}U^{\delta}U^{\epsilon} \\
&\quad - A_4(\eta^{\alpha\beta}U^{\gamma}U^{\delta}U^{\epsilon} + \eta^{\alpha\gamma}U^{\beta}U^{\delta}U^{\epsilon} + \eta^{\alpha\delta}U^{\gamma}U^{\beta}U^{\epsilon} + \eta^{\alpha\epsilon}U^{\gamma}U^{\delta}U^{\beta} \\
&\qquad + \eta^{\gamma\beta}U^{\alpha}U^{\delta}U^{\epsilon} + \eta^{\delta\beta}U^{\alpha}U^{\gamma}U^{\epsilon} + \eta^{\epsilon\beta}U^{\alpha}U^{\gamma}U^{\delta} + \eta^{\gamma\delta}U^{\alpha}U^{\beta}U^{\epsilon} \\
&\qquad + \eta^{\gamma\epsilon}U^{\alpha}U^{\beta}U^{\delta} + \eta^{\delta\epsilon}U^{\alpha}U^{\beta}U^{\gamma}) \\
&\quad + A_3(U^{\delta}(\eta^{\alpha\beta}\eta^{\gamma\epsilon} + \eta^{\alpha\gamma}\eta^{\beta\epsilon} + \eta^{\epsilon\beta}\eta^{\gamma\alpha}) + U^{\gamma}(\eta^{\alpha\beta}\eta^{\delta\epsilon} + \eta^{\alpha\delta}\eta^{\beta\epsilon} + \eta^{\epsilon\beta}\eta^{\delta\alpha}) \\
&\qquad + U^{\beta}(\eta^{\alpha\gamma}\eta^{\delta\epsilon} + \eta^{\alpha\delta}\eta^{\gamma\epsilon} + \eta^{\epsilon\gamma}\eta^{\delta\alpha}) + U^{\alpha}(\eta^{\beta\gamma}\eta^{\delta\epsilon} + \eta^{\beta\delta}\eta^{\gamma\epsilon} + \eta^{\epsilon\gamma}\eta^{\delta\beta}))) \\
Z^{\alpha\beta\gamma\delta\epsilon\nu} &= BT^6(A_6U^{\alpha}U^{\beta}U^{\gamma}U^{\delta}U^{\epsilon}U^{\nu} \\
&\quad - A_5(\eta^{\alpha\beta}U^{\gamma}U^{\delta}U^{\epsilon}U^{\nu} + \eta^{\alpha\gamma}U^{\beta}U^{\delta}U^{\epsilon}U^{\nu} + \eta^{\alpha\delta}U^{\beta}U^{\gamma}U^{\epsilon}U^{\nu} \\
&\qquad + \eta^{\alpha\epsilon}U^{\beta}U^{\gamma}U^{\delta}U^{\nu} + \eta^{\alpha\nu}U^{\beta}U^{\gamma}U^{\delta}U^{\epsilon} + \eta^{\beta\gamma}U^{\alpha}U^{\delta}U^{\epsilon}U^{\nu} \\
&\qquad + \eta^{\beta\delta}U^{\alpha}U^{\gamma}U^{\epsilon}U^{\nu} + \eta^{\beta\epsilon}U^{\alpha}U^{\gamma}U^{\delta}U^{\nu} + \eta^{\beta\nu}U^{\alpha}U^{\gamma}U^{\delta}U^{\epsilon} \\
&\qquad + \eta^{\gamma\delta}U^{\alpha}U^{\beta}U^{\epsilon}U^{\nu} + \eta^{\gamma\epsilon}U^{\alpha}U^{\beta}U^{\delta}U^{\nu} + \eta^{\gamma\nu}U^{\alpha}U^{\beta}U^{\delta}U^{\epsilon} \\
&\qquad + \eta^{\delta\epsilon}U^{\alpha}U^{\beta}U^{\gamma}U^{\nu} + \eta^{\delta\nu}U^{\alpha}U^{\beta}U^{\gamma}U^{\epsilon} + \eta^{\epsilon\nu}U^{\alpha}U^{\beta}U^{\gamma}U^{\delta}) \\
&\quad + A_4(U^{\alpha}U^{\beta}(\eta^{\gamma\nu}\eta^{\delta\epsilon} + \eta^{\gamma\delta}\eta^{\nu\epsilon} + \eta^{\gamma\epsilon}\eta^{\delta\nu}) + U^{\alpha}U^{\gamma}(\eta^{\beta\nu}\eta^{\delta\epsilon} + \eta^{\beta\delta}\eta^{\nu\epsilon} + \eta^{\beta\epsilon}\eta^{\delta\nu}) \\
&\qquad + U^{\alpha}U^{\nu}(\eta^{\gamma\beta}\eta^{\delta\epsilon} + \eta^{\gamma\delta}\eta^{\beta\epsilon} + \eta^{\gamma\epsilon}\eta^{\beta\delta}) + U^{\alpha}U^{\delta}(\eta^{\gamma\nu}\eta^{\beta\epsilon} + \eta^{\gamma\beta}\eta^{\nu\epsilon} + \eta^{\gamma\epsilon}\eta^{\nu\beta}) \\
&\qquad + U^{\alpha}U^{\epsilon}(\eta^{\gamma\nu}\eta^{\delta\beta} + \eta^{\gamma\delta}\eta^{\nu\beta} + \eta^{\gamma\beta}\eta^{\delta\nu}) + U^{\gamma}U^{\beta}(\eta^{\alpha\nu}\eta^{\delta\epsilon} + \eta^{\alpha\delta}\eta^{\nu\epsilon} + \eta^{\alpha\epsilon}\eta^{\delta\nu}) \\
&\qquad + U^{\nu}U^{\beta}(\eta^{\gamma\alpha}\eta^{\delta\epsilon} + \eta^{\gamma\delta}\eta^{\alpha\epsilon} + \eta^{\gamma\epsilon}\eta^{\alpha\delta}) + U^{\delta}U^{\beta}(\eta^{\gamma\nu}\eta^{\alpha\epsilon} + \eta^{\gamma\alpha}\eta^{\nu\epsilon} + \eta^{\gamma\epsilon}\eta^{\nu\alpha}) \\
&\qquad + U^{\epsilon}U^{\beta}(\eta^{\gamma\nu}\eta^{\delta\alpha} + \eta^{\gamma\delta}\eta^{\nu\alpha} + \eta^{\gamma\alpha}\eta^{\delta\nu}) + U^{\delta}U^{\gamma}(\eta^{\beta\nu}\eta^{\alpha\epsilon} + \eta^{\alpha\beta}\eta^{\nu\epsilon} + \eta^{\beta\epsilon}\eta^{\nu\alpha}) \\
&\qquad + U^{\delta}U^{\epsilon}(\eta^{\beta\nu}\eta^{\alpha\gamma} + \eta^{\alpha\beta}\eta^{\nu\gamma} + \eta^{\beta\gamma}\eta^{\nu\alpha}) + U^{\delta}U^{\nu}(\eta^{\beta\gamma}\eta^{\alpha\epsilon} + \eta^{\alpha\beta}\eta^{\gamma\epsilon} + \eta^{\beta\epsilon}\eta^{\gamma\alpha}) \\
&\qquad + U^{\gamma}U^{\epsilon}(\eta^{\beta\nu}\eta^{\alpha\delta} + \eta^{\alpha\beta}\eta^{\delta\nu} + \eta^{\beta\delta}\eta^{\nu\alpha}) + U^{\gamma}U^{\epsilon}(\eta^{\beta\epsilon}\eta^{\alpha\delta} + \eta^{\alpha\beta}\eta^{\delta\epsilon} + \eta^{\beta\delta}\eta^{\nu\alpha}) \\
&\qquad + U^{\epsilon}U^{\nu}(\eta^{\beta\gamma}\eta^{\alpha\delta} + \eta^{\alpha\beta}\eta^{\gamma\delta} + \eta^{\beta\delta}\eta^{\gamma\alpha})) \\
&\quad - A_3(\eta^{\epsilon\nu}(\eta^{\alpha\beta}\eta^{\gamma\delta} + \eta^{\alpha\gamma}\eta^{\beta\delta} + \eta^{\delta\beta}\eta^{\gamma\alpha}) + \eta^{\delta\nu}(\eta^{\alpha\beta}\eta^{\gamma\epsilon} + \eta^{\alpha\gamma}\eta^{\beta\epsilon} + \eta^{\epsilon\beta}\eta^{\gamma\alpha}) \\
&\qquad + \eta^{\gamma\nu}(\eta^{\alpha\beta}\eta^{\delta\epsilon} + \eta^{\alpha\delta}\eta^{\beta\epsilon} + \eta^{\epsilon\beta}\eta^{\delta\alpha}) + \eta^{\beta\nu}(\eta^{\alpha\gamma}\eta^{\delta\epsilon} + \eta^{\alpha\delta}\eta^{\gamma\epsilon} + \eta^{\epsilon\gamma}\eta^{\delta\alpha}) \\
&\qquad + \eta^{\alpha\nu}(\eta^{\beta\gamma}\eta^{\delta\epsilon} + \eta^{\beta\delta}\eta^{\gamma\epsilon} + \eta^{\epsilon\gamma}\eta^{\delta\beta})))
\end{aligned}
$$

where the common prefactor B and the coefficients $A_0, A_1, \ldots A_n$ are specified in the coming sections for the different dimensional cases.

B.1 Integrals in $(3+1)$ *dimensions*

$$
\begin{aligned}
B &= 4\pi m T \\
A_0 &= K_1\left(\frac{m}{T}\right) \\
A_1 &= \frac{m}{T} K_2\left(\frac{m}{T}\right) \\
A_2 &= \left(\frac{m}{T}\right)^2 K_3\left(\frac{m}{T}\right) \\
A_3 &= \left(\frac{m}{T}\right)^3 K_4\left(\frac{m}{T}\right) \\
A_4 &= \left(\frac{m}{T}\right)^4 K_5\left(\frac{m}{T}\right) \\
&\vdots \\
A_n &= \left(\frac{m}{T}\right)^n K_{n+1}\left(\frac{m}{T}\right)
\end{aligned}
$$

B.2 Integrals in $(2+1)$ *dimensions*

$$
\begin{aligned}
B &= 2\pi T e^{-\frac{m}{T}} \\
A_0 &= 1 \\
A_1 &= 1 + \frac{m}{T} \\
A_2 &= 3 + 3\frac{m}{T} + \left(\frac{m}{T}\right)^2 \\
A_3 &= 15 + 15\frac{m}{T} + 6\left(\frac{m}{T}\right)^2 + \left(\frac{m}{T}\right)^3 \\
A_4 &= 105 + 105\frac{m}{T} + 45\left(\frac{m}{T}\right)^2 + 10\left(\frac{m}{T}\right)^3 + \left(\frac{m}{T}\right)^4 \\
&\vdots \\
A_n &= \theta_n(\frac{m}{T})
\end{aligned}
$$

where θ_n are the reverse Bessel polynomial [147] defined as:

$$\theta_n(x) = x^n\, y_n(\frac{1}{x}) = \sum_{k=0}^{n} \frac{(n+k)!}{(n-k)!k!}\, \frac{x^{n-k}}{2^k}$$

B.3 Integrals in $(1+1)$ dimensions

$$\begin{aligned}
B &= 2 \\
A_0 &= K_0\left(\frac{m}{T}\right) \\
A_1 &= \frac{m}{T} K_1\left(\frac{m}{T}\right) \\
A_2 &= \left(\frac{m}{T}\right)^2 K_2\left(\frac{m}{T}\right) \\
A_3 &= \left(\frac{m}{T}\right)^3 K_3\left(\frac{m}{T}\right) \\
A_4 &= \left(\frac{m}{T}\right)^4 K_4\left(\frac{m}{T}\right) \\
&\vdots \\
A_n &= \left(\frac{m}{T}\right)^n K_n\left(\frac{m}{T}\right)
\end{aligned}$$

C

Relativistic Orthogonal Polynomials

In this appendix we provide the analytic expressions of the relativistic orthogonal polynomials, up to the second order, for both the massive and massless case in $(3+1)$, $(2+1)$ and $(1+1)$ dimensions. The polynomials have been derived following a Gram-Schmidt procedure starting from the set $\mathcal{V} = \{1, p^\alpha, p^\alpha p^\beta \dots\}$ $(\alpha, \beta \in \{0, x, y, z\})$, and using as weighting function ω the equilibrium distribution in the co-moving frame:

$$\omega(p^0) = \frac{1}{N_R} \exp\left(-p^0/T_0\right) \quad , \tag{C.1}$$

with N_R a normalization factor under the measure $\mathrm{d}^D\boldsymbol{p}/p^0$.

The notation $J^{(n)}_{m_1 \dots m_n}$, $m_i \in 0, x, y, z$ is used to label the polynomial of order n with the subscript m referring to the corresponding element of the generating basis $\mathcal{V}$.

C.1 $(3+1)$ *dimensions*

C.1.1 $\bar{m} \neq 0$

In order to write the polynomials in a more compact form, we define the shorthand

$$G_3 = \bar{m}\frac{K_2(\bar{m})}{K_1(\bar{m})} \quad . \tag{C.2}$$

$$J^{(0)} = 1$$

$$J_0^{(1)} = \frac{\bar{p}^0 - G_3}{\sqrt{\bar{m}^2 - (G_3 - 3)G_3}}$$

$$J_x^{(1)} = \frac{\bar{p}^x}{\sqrt{G_3}}$$

$$J_y^{(1)} = \frac{\bar{p}^y}{\sqrt{G_3}}$$

$$J_z^{(1)} = \frac{\bar{p}^z}{\sqrt{G_3}}$$

$$J_{00}^{(2)} = \frac{1}{((G_3-3)G_3 - \bar{m}^2)\sqrt{3G_3\left(\frac{3G_3}{(G_3-3)G_3-\bar{m}^2}+5\right)+6\bar{m}^2}}\left((\bar{p}^0)^2\left(G_3^2 - 3G_3 - \bar{m}^2\right) + 3\bar{p}^0\left(-G_3^2 + 4G_3 + \bar{m}^2\right) - G_3^2\left(\bar{m}^2+3\right) + 3G_3\bar{m}^2 + \bar{m}^4\right)$$

$$J_{xx}^{(2)} = \frac{2(\bar{p}^x)^2 - (\bar{p}^y)^2 - (\bar{p}^z)^2}{2\sqrt{3}\sqrt{4G_3 + \bar{m}^2}}$$

$$J_{yy}^{(2)} = \frac{(\bar{p}^y)^2 - (\bar{p}^z)^2}{2\sqrt{4G_3 + \bar{m}^2}}$$

$$J_{0x}^{(2)} = \frac{G_3\bar{p}^0\bar{p}^x - \bar{p}^x\left(4G_3 + \bar{m}^2\right)}{G_3\sqrt{-\frac{\bar{m}^4}{G_3} + (G_3-3)\bar{m}^2 + 4G_3}}$$

$$J_{0y}^{(2)} = \frac{G_3\bar{p}^0\bar{p}^y - \bar{p}^y\left(4G_3 + \bar{m}^2\right)}{G_3\sqrt{-\frac{\bar{m}^4}{G_3} + (G_3-3)\bar{m}^2 + 4G_3}}$$

$$J_{0z}^{(2)} = \frac{G_3\bar{p}^0\bar{p}^z - \bar{p}^z\left(4G_3 + \bar{m}^2\right)}{G_3\sqrt{-\frac{\bar{m}^4}{G_3} + (G_3-3)\bar{m}^2 + 4G_3}}$$

$$J_{xy}^{(2)} = \frac{\bar{p}^x\bar{p}^y}{\sqrt{4G_3 + \bar{m}^2}}$$

$$J_{xz}^{(2)} = \frac{\bar{p}^x\bar{p}^z}{\sqrt{4G_3 + \bar{m}^2}}$$

$$J_{yz}^{(2)} = \frac{\bar{p}^y\bar{p}^z}{\sqrt{4G_3 + \bar{m}^2}}$$

C.1.1 $\bar{m} = 0$

It is simple to verify that in the limit $\bar{m} \to 0$, $G_3 \to 2$. With this knowledge it is straightforward to calculate the polynomials in the mass-less limit.

$$J^{(0)} = 1$$

$$J_0^{(1)} = \frac{\bar{p}^0 - 2}{\sqrt{2}}$$

$$
\begin{aligned}
J_x^{(1)} &= \frac{\bar{p}^x}{\sqrt{2}} \\
J_y^{(1)} &= \frac{\bar{p}^y}{\sqrt{2}} \\
J_z^{(1)} &= \frac{\bar{p}^z}{\sqrt{2}} \\
J_{00}^{(2)} &= \frac{(\bar{p}^0-6)\bar{p}^0+6}{2\sqrt{3}} \\
J_{xx}^{(2)} &= -\frac{(\bar{p}^0)^2-3(\bar{p}^x)^2}{4\sqrt{6}} \\
J_{yy}^{(2)} &= \frac{(\bar{p}^y)^2-(\bar{p}^z)^2}{4\sqrt{2}} \\
J_{0x}^{(2)} &= \frac{(\bar{p}^0-4)\bar{p}^x}{2\sqrt{2}} \\
J_{0y}^{(2)} &= \frac{(\bar{p}^0-4)\bar{p}^y}{2\sqrt{2}} \\
J_{0z}^{(2)} &= \frac{(\bar{p}^0-4)\bar{p}^z}{2\sqrt{2}} \\
J_{xy}^{(2)} &= \frac{\bar{p}^x\bar{p}^y}{2\sqrt{2}} \\
J_{xz}^{(2)} &= \frac{\bar{p}^x\bar{p}^z}{2\sqrt{2}} \\
J_{yz}^{(2)} &= \frac{\bar{p}^y\bar{p}^z}{2\sqrt{2}}
\end{aligned}
$$

C.2 $(2+1)$ *dimensions*

C.2.2 $\bar{m} \neq 0$

$$
\begin{aligned}
J^{(0)} &= 1 \\
J_0^{(1)} &= \bar{p}^0 - 1 - \bar{m} \\
J_x^{(1)} &= \frac{1}{\sqrt{1+\bar{m}}}\bar{p}^x \\
J_y^{(1)} &= \frac{1}{\sqrt{1+\bar{m}}}\bar{p}^y \\
J_{00}^{(2)} &= \frac{1}{2}(\bar{p}^0)^2 + (-2-\bar{m})\bar{p}^0 + \frac{1}{2}(2+\bar{m}(4+\bar{m}))
\end{aligned}
$$

$$J^{(2)}_{0x} = \frac{-3-\bar{m}(3+\bar{m})}{(1+\bar{m})\sqrt{4+2\bar{m}-1/(1+\bar{m})}}\bar{p}^x + \frac{1}{\sqrt{4+2\bar{m}-1/(1+\bar{m})}}\bar{p}^0\bar{p}^x$$
$$J^{(2)}_{0y} = \frac{-3-\bar{m}(3+\bar{m})}{(1+\bar{m})\sqrt{4+2\bar{m}-1/(1+\bar{m})}}\bar{p}^y + \frac{1}{\sqrt{4+2\bar{m}-1/(1+\bar{m})}}\bar{p}^0\bar{p}^y$$
$$J^{(2)}_{xx} = \frac{\bar{m}^2}{2\sqrt{3+\bar{m}(3+\bar{m})}} - \frac{(\bar{p}^0)^2}{2\sqrt{3+\bar{m}(3+\bar{m})}} + \frac{(\bar{p}^x)^2}{\sqrt{3+\bar{m}(3+\bar{m})}}$$
$$J^{(2)}_{xy} = \frac{1}{\sqrt{3+\bar{m}(3+\bar{m})}}\bar{p}^x\bar{p}^y$$

C.2.2 $\bar{m} = 0$

$$J^{(0)} = 1$$
$$J^{(1)}_0 = \bar{p}^0 - 1$$
$$J^{(1)}_x = \bar{p}^x$$
$$J^{(1)}_y = \bar{p}^y$$
$$J^{(2)}_{00} = \frac{1}{2}(\bar{p}^0)^2 - 2\bar{p}^0 + 1$$
$$J^{(2)}_{0x} = \frac{1}{\sqrt{3}}\bar{p}^0\bar{p}^x - \sqrt{3}\bar{p}^x$$
$$J^{(2)}_{0y} = \frac{1}{\sqrt{3}}\bar{p}^0\bar{p}^y - \sqrt{3}\bar{p}^y$$
$$J^{(2)}_{xx} = \frac{1}{\sqrt{3}}(\bar{p}^x)^2 - \frac{1}{2\sqrt{3}}(\bar{p}^0)^2$$
$$J^{(2)}_{xy} = \frac{1}{\sqrt{3}}\bar{p}^x\bar{p}^y$$

C.3 $(1+1)$ *dimensions*

C.3.3 $\bar{m} \neq 0$

Like in the $(3+1)$ dimensional case we find convenient to express all the Bessel coefficients by means of the following shorthand:

$$G_1 = \bar{m}\frac{K_1(\bar{m})}{K_0(\bar{m})} \quad . \tag{C.3}$$

$J^{(0)} = 1$

$$
\begin{aligned}
J_x^{(1)} &= \frac{\bar{p}^x}{\sqrt{G_1}} \\
J_0^{(1)} &= \frac{\bar{p}^0 - G_1}{\sqrt{-G_1^2 + G_1 + \bar{m}^2}} \\
J_{00}^{(2)} &= \frac{1}{\left(G_1^2 - G_1 - \bar{m}^2\right)\sqrt{\frac{-3G_1^3 - 2G_1^2(\bar{m}^2 - 1) + 5G_1\bar{m}^2 + 2\bar{m}^4}{-G_1^2 + G_1 + \bar{m}^2}}} \left((\bar{p}^0)^2\left(G_1^2 - G_1 - \bar{m}^2\right)\right. \\
&\quad \left. + \bar{p}^0\left(-G_1^2 + 2G_1 + \bar{m}^2\right) - G_1^2\left(\bar{m}^2 + 1\right) + G_1\bar{m}^2 + \bar{m}^4\right) \\
J_{0x}^{(2)} &= \frac{G_1\bar{p}^0\bar{p}^x - \bar{p}^x\left(2G_1 + \bar{m}^2\right)}{G_1\sqrt{-\frac{\bar{m}^4}{G_1} + G_1\left(\bar{m}^2 + 2\right) - \bar{m}^2}}
\end{aligned}
$$

C.3.3 $\bar{m} = 0$

It is simple to see that since $G_1 \to 0$ for $\bar{m} \to 0$, we cannot define the mass-less limit for the polynomials in $(1 + 1)$ dimensions.

D

Relativistic Orthogonal Projections

In this appendix we provide the analytic expressions of the orthogonal projections, up to the second order, for both the massive and massless case in $(3+1)$, $(2+1)$ and $(1+1)$ dimensions. The projection coefficients are defined as

$$a^{(k)}((U^\mu),T) = \int_{\mathbb{R}^D} f^{\mathrm{eq}}((p^\mu),(U^\mu),T) J^{(k)}((p^\mu)) \frac{\mathrm{d}\boldsymbol{p}}{p^0} \quad , \tag{D.1}$$

with $J^{(k)}$ the orthogonal polynomials introduced in Appendix C. The notation used for the projection coefficients $a^{(k)}$ is the same previously introduced for the the orthogonal polynomials.

D.1 $(3+1)$ *dimensions*

D.1.1 $\bar{m} \neq 0$

$$a^{(0)} = \frac{1}{G_3}$$
$$a_0^{(1)} = \frac{U^0 - 1}{\sqrt{\bar{m}^2 - (G_3 - 3)G_3}}$$
$$a_x^{(1)} = \frac{U^x}{\sqrt{G_3}}$$

$$
\begin{aligned}
a_y^{(1)} &= \frac{U^y}{\sqrt{G_3}} \\
a_z^{(1)} &= \frac{U^z}{\sqrt{G_3}} \\
a_{00}^{(2)} &= \frac{\sqrt{3G_3\left(\frac{3G_3}{(G_3-3)G_3-\bar{m}^2}+5\right)+6\bar{m}^2}}{3G_3\left(5G_3^3+2G_3^2\left(\bar{m}^2-6\right)-11G_3\bar{m}^2-2\bar{m}^4\right)}\left(G_3^3\left(\bar{T}\left(4(U^0)^2-1\right)\right.\right. \\
&\quad \left.-3U^0\right)+G_3^2\left(\bar{m}^2\left((U^0)^2-1\right)+3\left(-4\bar{T}(U^0)^2+\bar{T}+4U^0-1\right)\right) \\
&\quad \left.+G_3\bar{m}^2\left(-(4\bar{T}+3)(U^0)^2+\bar{T}+3U^0+3\right)-\bar{m}^4\left((U^0)^2-1\right)\right. \\
a_{xx}^{(2)} &= -\frac{\left((U^0)^2-3(U^x)^2-1\right)\left(4G_3\bar{T}+\bar{m}^2\right)}{2\sqrt{3}G_3\sqrt{4G_3+\bar{m}^2}} \\
a_{yy}^{(2)} &= -\frac{\left(4G_3\bar{T}+\bar{m}^2\right)\left((U^0)^2-(U^x)^2-2(U^y)^2-1\right)}{2G_3\sqrt{4G_3+\bar{m}^2}} \\
a_{0x}^{(2)} &= \frac{U^x\left(4G_3(\bar{T}U^0-1)+\bar{m}^2(U^0-1)\right)}{G_3\sqrt{-\frac{\bar{m}^4}{G_3}+(G_3-3)\bar{m}^2+4G_3}} \\
a_{0y}^{(2)} &= \frac{U^y\left(4G_3(\bar{T}U^0-1)+\bar{m}^2(U^0-1)\right)}{G_3\sqrt{-\frac{\bar{m}^4}{G_3}+(G_3-3)\bar{m}^2+4G_3}} \\
a_{0z}^{(2)} &= \frac{U^z\left(4G_3(\bar{T}U^0-1)+\bar{m}^2(U^0-1)\right)}{G_3\sqrt{-\frac{\bar{m}^4}{G_3}+(G_3-3)\bar{m}^2+4G_3}} \\
a_{xy}^{(2)} &= \frac{U^xU^y\left(4G_3\bar{T}+\bar{m}^2\right)}{G_3\sqrt{4G_3+\bar{m}^2}} \\
a_{xz}^{(2)} &= \frac{U^xU^z\left(4G_3\bar{T}+\bar{m}^2\right)}{G_3\sqrt{4G_3+\bar{m}^2}} \\
a_{yz}^{(2)} &= \frac{U^yU^z\left(4G_3\bar{T}+\bar{m}^2\right)}{G_3\sqrt{4G_3+\bar{m}^2}}
\end{aligned}
$$

where G_3 was previously defined in Eq. C.2.

D.1.1 $\bar{m} = 0$

$$
\begin{aligned}
a^{(0)} &= \frac{1}{2} \\
a_0^{(1)} &= \frac{U^0-1}{\sqrt{2}} \\
a_x^{(1)} &= \frac{U^x}{\sqrt{2}}
\end{aligned}
$$

$$
\begin{aligned}
a_y^{(1)} &= \frac{U^y}{\sqrt{2}} \\
a_z^{(1)} &= \frac{U^z}{\sqrt{2}} \\
a_{00}^{(2)} &= \frac{(2U^0-1)(2\bar{T}U^0+\bar{T}-3)}{2\sqrt{3}} \\
a_{xx}^{(2)} &= \frac{\bar{T}\left(-(U^0)^2+3(U^x)^2+1\right)}{\sqrt{6}} \\
a_{yy}^{(2)} &= \frac{\bar{T}\left(-(U^0)^2+(U^x)^2+2(U^y)^2+1\right)}{\sqrt{2}} \\
a_{0x}^{(2)} &= \sqrt{2}U^x(\bar{T}U^0-1) \\
a_{0y}^{(2)} &= \sqrt{2}U^y(\bar{T}U^0-1) \\
a_{0z}^{(2)} &= \sqrt{2}U^z(\bar{T}U^0-1) \\
a_{xy}^{(2)} &= \sqrt{2}\bar{T}U^xU^y \\
a_{xz}^{(2)} &= \sqrt{2}\bar{T}U^xU^z \\
a_{yz}^{(2)} &= \sqrt{2}\bar{T}U^yU^z
\end{aligned}
$$

D.2 $(2+1)$ *dimensions*

D.2.2 $\bar{m} \neq 0$

$$
\begin{aligned}
a^{(0)} &= \frac{1}{\bar{m}+\bar{T}} \\
a_0^{(1)} &= U^0 - \frac{\bar{m}+1}{\bar{m}+\bar{T}} \\
a_x^{(1)} &= \frac{U^x}{\sqrt{\bar{m}+1}} \\
a_y^{(1)} &= \frac{U^y}{\sqrt{\bar{m}+1}} \\
a_{00}^{(2)} &= \frac{1}{2(\bar{m}+\bar{T})}\left(\bar{m}^2(U^0-1)^2+\bar{m}(U^0-1)(3\bar{T}U^0+\bar{T}-4)\right. \\
&\quad \left.+\bar{T}^2\left(3(U^0)^2-1\right)-4\bar{T}U^0+2\right) \\
a_{0x}^{(2)} &= \frac{U^x\left((\bar{m}+1)U^0\left(\bar{m}^2+3\bar{m}\bar{T}+3\bar{T}^2\right)-(\bar{m}(\bar{m}+3)+3)(\bar{m}+\bar{T})\right)}{(\bar{m}+1)\sqrt{2\bar{m}-\frac{1}{\bar{m}+1}+4}(\bar{m}+\bar{T})}
\end{aligned}
$$

$$a_{0y}^{(2)} = \frac{U^y\left((\bar{m}+1)U^0\left(\bar{m}^2+3\bar{m}\bar{T}+3\bar{T}^2\right)-(\bar{m}(\bar{m}+3)+3)(\bar{m}+\bar{T})\right)}{(\bar{m}+1)\sqrt{2\bar{m}-\frac{1}{\bar{m}+1}+4}(\bar{m}+\bar{T})}$$
$$a_{xx}^{(2)} = -\frac{\left(\bar{m}^2+3\bar{m}\bar{T}+3\bar{T}^2\right)\left((U^0)^2-2(U^x)^2-1\right)}{2\sqrt{\bar{m}(\bar{m}+3)+3}(\bar{m}+\bar{T})}$$
$$a_{xy}^{(2)} = \frac{U^xU^y\left(\bar{m}^2+3\bar{m}\bar{T}+3\bar{T}^2\right)}{\sqrt{\bar{m}(\bar{m}+3)+3}(\bar{m}+\bar{T})}$$

D.2.2 $\bar{m}=0$

$$a^{(0)} = \frac{1}{\bar{T}}$$
$$a_0^{(1)} = U^0 - \frac{1}{\bar{T}}$$
$$a_x^{(1)} = U^x$$
$$a_y^{(1)} = U^y$$
$$a_{00}^{(2)} = \frac{1}{2}\bar{T}\left(3(U^0)^2-1\right)+\frac{1}{\bar{T}}-2U^0$$
$$a_{0x}^{(2)} = \sqrt{3}U^x(\bar{T}U^0-1)$$
$$a_{0y}^{(2)} = \sqrt{3}U^y(\bar{T}U^0-1)$$
$$a_{xx}^{(2)} = -\frac{1}{2}\sqrt{3}\bar{T}\left((U^0)^2-2(U^x)^2-1\right)$$
$$a_{xy}^{(2)} = \sqrt{3}\bar{T}U^xU^y$$

D.3 $(1+1)$ *dimensions*

D.3.3 $\bar{m}\neq 0$

$$a^{(0)} = \frac{1}{G_1}$$
$$a_0^{(1)} = \frac{U^x}{\sqrt{G_1}}$$
$$a_x^{(1)} = \frac{U^0-1}{\sqrt{-G_1^2+G_1+\bar{m}^2}}$$

$$
\begin{aligned}
a_{00}^{(2)} &= \frac{\sqrt{G_1\left(3-\frac{G_1}{-G_1^2+G_1+\bar{m}^2}\right)+2\bar{m}^2}}{G_1\left(G_1^2(3G_1-2)+G_1(2G_1-5)\bar{m}^2-2\bar{m}^4\right)}\left(G_1^3\left(\bar{T}\left(2(U^0)^2-1\right)\right.\right.\\
&\quad \left.-U^0\right)+G_1^2\left(\bar{m}^2\left((U^0)^2-1\right)-2\bar{T}(U^0)^2+\bar{T}+2U^0-1\right)+G_1\bar{m}^2\\
&\quad \times\left(-(2\bar{T}+1)(U^0)^2+\bar{T}+U^0+1\right)-\bar{m}^4\left((U^0)^2-1\right)\Big)\\
a_{0x}^{(2)} &= \frac{U^x\left(2G_1(\bar{T}U^0-1)+\bar{m}^2(U^0-1)\right)}{G_1\sqrt{-\frac{\bar{m}^4}{G_1}+(G_1-1)\bar{m}^2+2G_1}}
\end{aligned}
$$

where G_1 was previously defined in Eq. C.2.

D.3.3 $\bar{m}=0$

Since $G_1 \to 0$ for $\bar{m} \to 0$, we cannot define the mass-less limit for the orthogonal projections in $(1+1)$ dimensions.

E

Quadratures

In this appendix we present a collection of Gauss-type quadratures that can be used to implement a RLBM on a Cartesian grid, for both the massive and massless case in $(3+1)$, $(2+1)$ and $(1+1)$ dimensions. Examples are given at several order N, where in this context the order of a quadrature coincides with the maximum order of the polynomials for which the orthonormal conditions are satisfied:

$$\int_{\mathbb{R}^D} \omega(\bar{p}^0) J_l((\bar{p}^\mu)) J_k((\bar{p}^\mu)) \frac{\mathrm{d}\bar{\boldsymbol{p}}}{\bar{p}^0} = \sum_i w_i J_l((\bar{p}_i^\mu)) J_k((\bar{p}_i^\mu)) = \delta_{lk} \quad , \tag{E.1}$$

where $J^{(k)}$ are the orthogonal polynomials introduced in Appendix C, $(\bar{p}_i^\mu)$ the discrete $(D+1)$ momentum vectors, and w_i the quadrature weights.

E.1 Mildly relativistic regime

We use the following parametrization of the momentum vectors:

$$(\bar{p}_i^\mu) = \bar{m}\gamma_i(1, v_0 n_i) \quad , \tag{E.2}$$

where $n_i \in \mathbb{Z}^D$ are the vectors forming the stencil $G = \{n_i \mid i = 1, 2, \ldots, i_{max}\}$ defined by the (on-lattice) quadrature points, v_0 is a free parameter that can be freely chosen such that $v_i = v_0 ||n_i|| < 1, \forall i$, $\bar{m}$ is the non-dimensional rest mass in terms of a reference temperature T_0, and γ_i is the Lorentz factor associated to v_i.

In the following we present a few selected stencils, alongside a graphical view of their correspondent working range in terms of the parameter $\bar{m}$, that can be used to build a numerically stable quadrature at both 2nd and 3rd order.

E.1.1 $(3+1)$ *dimensions*

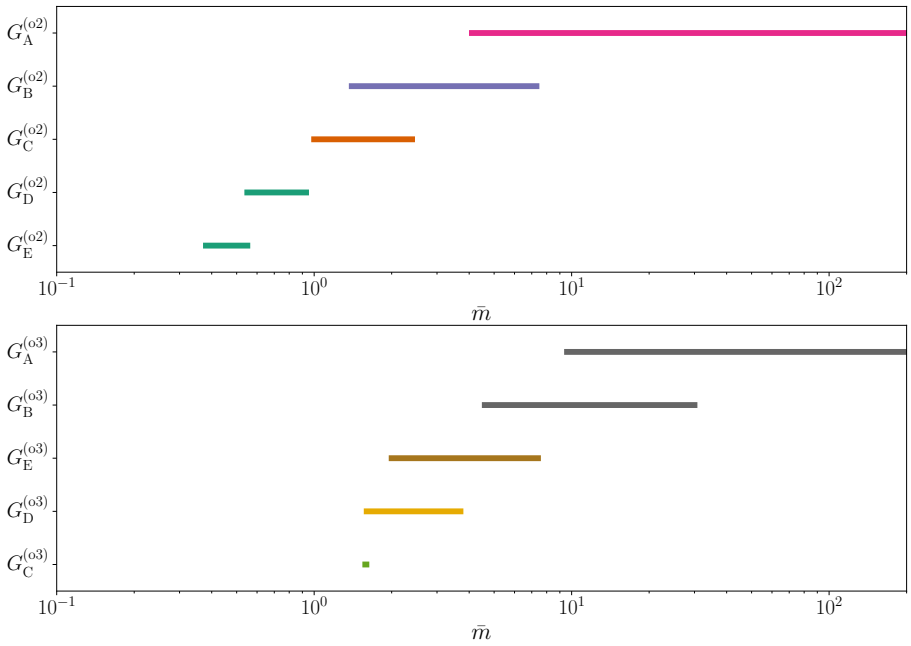

Order 2				
$G_{\mathrm{A}}^{(\mathrm{o2})} = \{\bigcup n_i\}$	$G_{\mathrm{B}}^{(\mathrm{o2})} = \{\bigcup n_i\}$	$G_{\mathrm{C}}^{(\mathrm{o2})} = \{\bigcup n_i\}$	$G_{\mathrm{D}}^{(\mathrm{o2})} = \{\bigcup n_i\}$	$G_{\mathrm{E}}^{(\mathrm{o2})} = \{\bigcup n_i\}$
$(\ 0,\ 0,\ 0)$	$(\ 0,\ 0,\ 0)$	$(\ 0,\ 0,\ 0)$	$(\ 0,\ 0,\ 0)$	$(\ 0,\ 0,\ 0)$
$(\pm1,\ 0,\ 0)_{\mathrm{FS}}$	$(\pm2, \pm1, \pm1)_{\mathrm{FS}}$	$(\pm1,\ 1,\ 0)_{\mathrm{FS}}$	$(\pm1,\ 1,\ 0)_{\mathrm{FS}}$	$(\pm2, \pm2,\ 0)_{\mathrm{FS}}$
$(\pm1,\ 1,\ 0)_{\mathrm{FS}}$	$(\pm2, \pm2, \pm1)_{\mathrm{FS}}$	$(\pm2, \pm2, \pm2)_{\mathrm{FS}}$	$(\pm4, \pm4, \pm2)_{\mathrm{FS}}$	$(\pm4, \pm4, \pm2)_{\mathrm{FS}}$
$(\pm1,\ 1,\ 1)_{\mathrm{FS}}$	$(\pm3, \pm1,\ 0)_{\mathrm{FS}}$	$(\pm3, \pm2, \pm1)_{\mathrm{FS}}$	$(\pm5, \pm4,\ 0)_{\mathrm{FS}}$	$(\pm5, \pm4,\ 0)_{\mathrm{FS}}$
$(\pm2,\ 0,\ 0)_{\mathrm{FS}}$	$(\pm3, \pm2,\ 0)_{\mathrm{FS}}$	$(\pm3, \pm3, \pm1)_{\mathrm{FS}}$	$(\pm6, \pm2,\ 0)_{\mathrm{FS}}$	$(\pm6, \pm2,\ 0)_{\mathrm{FS}}$
$(\pm2, \pm1,\ 0)_{\mathrm{FS}}$	$(\pm3, \pm1, \pm1)_{\mathrm{FS}}$	$(\pm4,\ 0,\ 0)_{\mathrm{FS}}$	$(\pm4, \pm4, \pm3)_{\mathrm{FS}}$	$(\pm6, \pm2, \pm1)_{\mathrm{FS}}$
Order 3				
$G_{\mathrm{A}}^{(\mathrm{o3})} = \{\bigcup n_i\}$	$G_{\mathrm{B}}^{(\mathrm{o3})} = \{\bigcup n_i\}$	$G_{\mathrm{C}}^{(\mathrm{o3})} = \{\bigcup n_i\}$	$G_{\mathrm{D}}^{(\mathrm{o3})} = \{\bigcup n_i\}$	$G_{\mathrm{E}}^{(\mathrm{o3})} = \{\bigcup n_i\}$
$(\ 0,\ 0,\ 0)$	$(\ 0,\ 0,\ 0)$	$(\ 0,\ 0,\ 0)$	$(\ 0,\ 0,\ 0)$	$(\ 0,\ 0,\ 0)$
$(\pm1,\ 0,\ 0)_{\mathrm{FS}}$	$(\pm1,\ 0,\ 0)_{\mathrm{FS}}$	$(\pm1,\ 0,\ 0)_{\mathrm{FS}}$	$(\pm2, \pm1, \pm1)_{\mathrm{FS}}$	$(\pm2, \pm1, \pm1)_{\mathrm{FS}}$
$(\pm1,\ 1,\ 0)_{\mathrm{FS}}$	$(\pm1,\ 1,\ 1)_{\mathrm{FS}}$	$(\pm4,\ 0,\ 0)_{\mathrm{FS}}$	$(\pm3, \pm3, \pm1)_{\mathrm{FS}}$	$(\pm3, \pm3, \pm1)_{\mathrm{FS}}$
$(\pm1,\ 1,\ 1)_{\mathrm{FS}}$	$(\pm2,\ 0,\ 0)_{\mathrm{FS}}$	$(\pm4, \pm1,\ 0)_{\mathrm{FS}}$	$(\pm4, \pm4,\ 0)_{\mathrm{FS}}$	$(\pm4, \pm1, \pm1)_{\mathrm{FS}}$
$(\pm2,\ 0,\ 0)_{\mathrm{FS}}$	$(\pm2, \pm2,\ 0)_{\mathrm{FS}}$	$(\pm4, \pm4,\ 0)_{\mathrm{FS}}$	$(\pm4, \pm1, \pm1)_{\mathrm{FS}}$	$(\pm4, \pm3, \pm1)_{\mathrm{FS}}$
$(\pm2, \pm1,\ 0)_{\mathrm{FS}}$	$(\pm2, \pm1, \pm1)_{\mathrm{FS}}$	$(\pm4, \pm3, \pm2)_{\mathrm{FS}}$	$(\pm4, \pm3, \pm1)_{\mathrm{FS}}$	$(\pm4, \pm3, \pm2)_{\mathrm{FS}}$
$(\pm2, \pm2,\ 0)_{\mathrm{FS}}$	$(\pm2, \pm2, \pm1)_{\mathrm{FS}}$	$(\pm4, \pm3, \pm3)_{\mathrm{FS}}$	$(\pm4, \pm3, \pm2)_{\mathrm{FS}}$	$(\pm4, \pm4, \pm2)_{\mathrm{FS}}$
$(\pm2, \pm1, \pm1)_{\mathrm{FS}}$	$(\pm2, \pm2, \pm2)_{\mathrm{FS}}$	$(\pm5, \pm1,\ 0)_{\mathrm{FS}}$	$(\pm4, \pm3, \pm3)_{\mathrm{FS}}$	$(\pm5, \pm2, \pm1)_{\mathrm{FS}}$
$(\pm2, \pm2, \pm1)_{\mathrm{FS}}$	$(\pm3,\ 0,\ 0)_{\mathrm{FS}}$	$(\pm5, \pm3,\ 0)_{\mathrm{FS}}$	$(\pm5, \pm3,\ 0)_{\mathrm{FS}}$	$(\pm5, \pm3, \pm1)_{\mathrm{FS}}$
$(\pm2, \pm2, \pm2)_{\mathrm{FS}}$	$(\pm3, \pm2,\ 0)_{\mathrm{FS}}$	$(\pm5, \pm2, \pm1)_{\mathrm{FS}}$	$(\pm5, \pm2, \pm1)_{\mathrm{FS}}$	$(\pm5, \pm2, \pm2)_{\mathrm{FS}}$
$(\pm3,\ 0,\ 0)_{\mathrm{FS}}$	$(\pm3, \pm1, \pm1)_{\mathrm{FS}}$	$(\pm5, \pm2, \pm2)_{\mathrm{FS}}$	$(\pm5, \pm2, \pm2)_{\mathrm{FS}}$	$(\pm6,\ 0,\ 0)_{\mathrm{FS}}$

Table E.1: *Example of stencils that can be used to construct a numerically stable quadrature, both at the second and third order, for a RLBM in* $(3+1)$ *dimensions. In the figure horizontal bars represent the working range of values* $\bar{m}$ *of each quadrature.*

E.1.1 $(2+1)$ *dimensions*

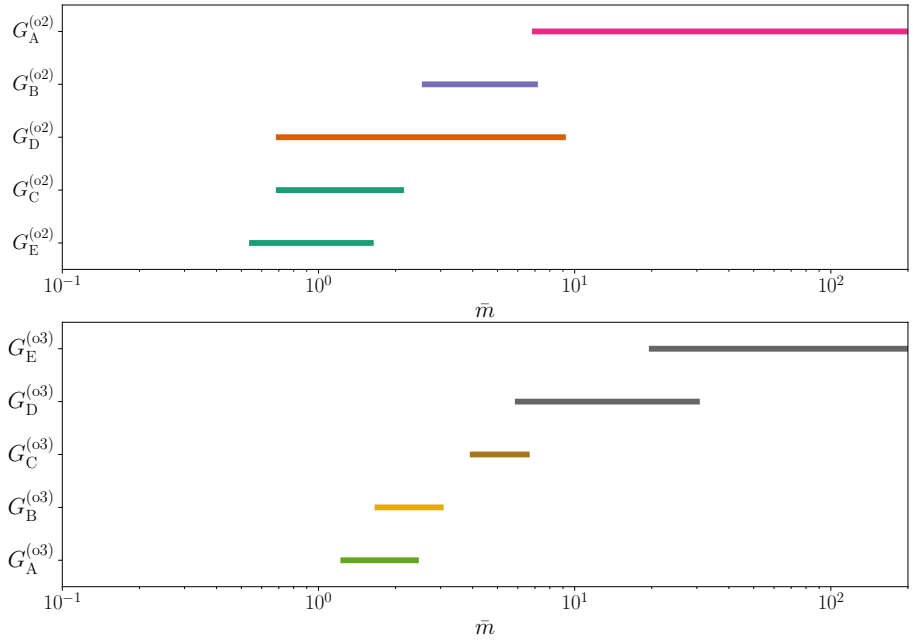

Order 2				
$G_{\mathrm{A}}^{(\mathrm{o2})} = \{\bigcup n_i\}$	$G_{\mathrm{B}}^{(\mathrm{o2})} = \{\bigcup n_i\}$	$G_{\mathrm{C}}^{(\mathrm{o2})} = \{\bigcup n_i\}$	$G_{\mathrm{D}}^{(\mathrm{o2})} = \{\bigcup n_i\}$	$G_{\mathrm{E}}^{(\mathrm{o2})} = \{\bigcup n_i\}$
$(\ 0,\ \ 0)$	$(\ 0,\ \ 0)$	$(\ 0,\ \ 0)$	$(\ 0,\ \ 0)$	$(\ 0,\ \ 0)$
$(\pm1,\ \ 0)_{\mathrm{FS}}$	$(\pm1,\ \ 0)_{\mathrm{FS}}$	$(\pm3, \pm3)_{\mathrm{FS}}$	$(\pm3, \pm1)_{\mathrm{FS}}$	$(\pm5, \pm2)_{\mathrm{FS}}$
$(\pm1, \pm1)_{\mathrm{FS}}$	$(\pm1, \pm1)_{\mathrm{FS}}$	$(\pm4, \pm2)_{\mathrm{FS}}$	$(\pm4, \pm2)_{\mathrm{FS}}$	$(\pm5, \pm3)_{\mathrm{FS}}$
$(\pm2,\ \ 0)_{\mathrm{FS}}$	$(\pm2, \pm2)_{\mathrm{FS}}$	$(\pm4, \pm3)_{\mathrm{FS}}$	$(\pm4, \pm3)_{\mathrm{FS}}$	$(\pm5, \pm4)_{\mathrm{FS}}$
$(\pm2, \pm1)_{\mathrm{FS}}$	$(\pm3, \pm2)_{\mathrm{FS}}$	$(\pm5,\ \ 0)_{\mathrm{FS}}$	$(\pm5,\ \ 0)_{\mathrm{FS}}$	$(\pm6,\ \ 0)_{\mathrm{FS}}$
$(\pm2, \pm2)_{\mathrm{FS}}$	$(\pm4,\ \ 0)_{\mathrm{FS}}$	$(\pm5, \pm1)_{\mathrm{FS}}$	$(\pm5, \pm1)_{\mathrm{FS}}$	$(\pm6, \pm2)_{\mathrm{FS}}$
Order 3				
$G_{\mathrm{A}}^{(\mathrm{o3})} = \{\bigcup n_i\}$	$G_{\mathrm{B}}^{(\mathrm{o3})} = \{\bigcup n_i\}$	$G_{\mathrm{C}}^{(\mathrm{o3})} = \{\bigcup n_i\}$	$G_{\mathrm{D}}^{(\mathrm{o3})} = \{\bigcup n_i\}$	$G_{\mathrm{E}}^{(\mathrm{o3})} = \{\bigcup n_i\}$
$(\ 0,\ \ 0)$	$(\ 0,\ \ 0)$	$(\ 0,\ \ 0)$	$(\ 0,\ \ 0)$	$(\ 0,\ \ 0)$
$(\pm1, \pm1)_{\mathrm{FS}}$	$(\pm1, \pm1)_{\mathrm{FS}}$	$(\pm1,\ \ 0)_{\mathrm{FS}}$	$(\pm1,\ \ 0)_{\mathrm{FS}}$	$(\pm1,\ \ 0)_{\mathrm{FS}}$
$(\pm4, \pm2)_{\mathrm{FS}}$	$(\pm2, \pm2)_{\mathrm{FS}}$	$(\pm2,\ \ 0)_{\mathrm{FS}}$	$(\pm1, \pm1)_{\mathrm{FS}}$	$(\pm1, \pm1)_{\mathrm{FS}}$
$(\pm5, \pm4)_{\mathrm{FS}}$	$(\pm4, \pm3)_{\mathrm{FS}}$	$(\pm2, \pm2)_{\mathrm{FS}}$	$(\pm2,\ \ 0)_{\mathrm{FS}}$	$(\pm2,\ \ 0)_{\mathrm{FS}}$
$(\pm5, \pm5)_{\mathrm{FS}}$	$(\pm5,\ \ 0)_{\mathrm{FS}}$	$(\pm3,\ \ 0)_{\mathrm{FS}}$	$(\pm2, \pm1)_{\mathrm{FS}}$	$(\pm2, \pm1)_{\mathrm{FS}}$
$(\pm6, \pm2)_{\mathrm{FS}}$	$(\pm5, \pm5)_{\mathrm{FS}}$	$(\pm3, \pm2)_{\mathrm{FS}}$	$(\pm3, \pm1)_{\mathrm{FS}}$	$(\pm2, \pm2)_{\mathrm{FS}}$
$(\pm6, \pm3)_{\mathrm{FS}}$	$(\pm6, \pm2)_{\mathrm{FS}}$	$(\pm3, \pm3)_{\mathrm{FS}}$	$(\pm3, \pm2)_{\mathrm{FS}}$	$(\pm3,\ \ 0)_{\mathrm{FS}}$
$(\pm6, \pm4)_{\mathrm{FS}}$	$(\pm6, \pm3)_{\mathrm{FS}}$	$(\pm4,\ \ 0)_{\mathrm{FS}}$	$(\pm3, \pm3)_{\mathrm{FS}}$	$(\pm3, \pm1)_{\mathrm{FS}}$
$(\pm7, \pm1)_{\mathrm{FS}}$	$(\pm6, \pm4)_{\mathrm{FS}}$	$(\pm4, \pm1)_{\mathrm{FS}}$	$(\pm4,\ \ 0)_{\mathrm{FS}}$	$(\pm3, \pm2)_{\mathrm{FS}}$
$(\pm7, \pm2)_{\mathrm{FS}}$	$(\pm7, \pm1)_{\mathrm{FS}}$	$(\pm4, \pm2)_{\mathrm{FS}}$	$(\pm4, \pm2)_{\mathrm{FS}}$	$(\pm3, \pm3)_{\mathrm{FS}}$

Table E.2: *Example of stencils that can be used to construct a numerically stable quadrature, both at the second and third order, for a RLBM in* $(2+1)$ *dimensions. In the figure horizontal bars represent the working range of values* $\bar{m}$ *of each quadrature.*

E.1.1 $(1+1)$ *dimensions*

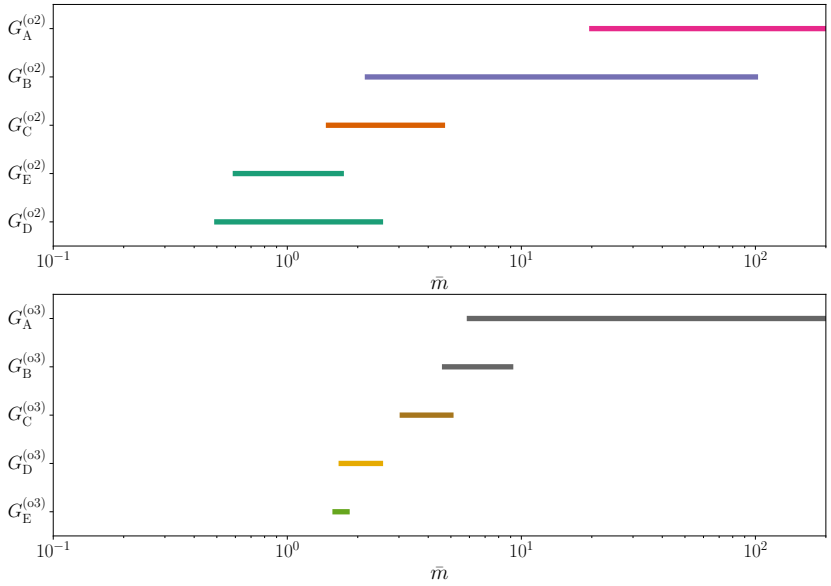

Order 2				
$G_{\mathrm{A}}^{(\mathrm{o}2)} = \{\bigcup n_i\}$	$G_{\mathrm{B}}^{(\mathrm{o}2)} = \{\bigcup n_i\}$	$G_{\mathrm{C}}^{(\mathrm{o}2)} = \{\bigcup n_i\}$	$G_{\mathrm{D}}^{(\mathrm{o}2)} = \{\bigcup n_i\}$	$G_{\mathrm{E}}^{(\mathrm{o}2)} = \{\bigcup n_i\}$
(0)	(0)	(0)	(0)	(0)
(±1)	(±1)	(±1)	(±13)	(±14)
(±2)	(±2)	(±2)	(±16)	(±15)
(±3)	(±3)	(±3)	(±17)	(±17)
(±7)	(±4)	(±5)	(±18)	(±18)
Order 3				
$G_{\mathrm{A}}^{(\mathrm{o}3)} = \{\bigcup n_i\}$	$G_{\mathrm{B}}^{(\mathrm{o}3)} = \{\bigcup n_i\}$	$G_{\mathrm{C}}^{(\mathrm{o}3)} = \{\bigcup n_i\}$	$G_{\mathrm{D}}^{(\mathrm{o}3)} = \{\bigcup n_i\}$	$G_{\mathrm{E}}^{(\mathrm{o}3)} = \{\bigcup n_i\}$
(0)	(0)	(0)	(0)	(0)
(±1)	(±1)	(±1)	(±11)	(±12)
(±2)	(±2)	(±5)	(±13)	(±13)
(±3)	(±4)	(±6)	(±15)	(±15)
(±4)	(±5)	(±8)	(±16)	(±16)
(±5)	(±6)	(±9)	(±17)	(±17)
(±6)	(±7)	(±10)	(±18)	(±18)

Table E.3: *Example of stencils that can be used to construct a numerically stable quadrature, both at the second and third order, for a RLBM in* $(1+1)$ *dimensions. In the figure horizontal bars represent the working range of values* $\bar{m}$ *of each quadrature.*

E.2 Ultra relativistic regime

For the special case of massless particles we have an extra degree of freedom given by the fact that in this case velocity does not depend on energy. We then associate several energy shells to each vector, thus adding a second index in the definition of the discrete momentum vectors:

$$(\bar{p}^{\mu}_{i,j}) = \bar{p}^{0}_{j}(1, \frac{n_i}{||n_i||}) \quad , \tag{E.3}$$

where the index j labels different energy shells, and it is clear that $||n_i||$ has to be the same for all the stencil vectors since all the particles travel at the same speed $v_i = c = 1, \forall i$.

In the following we provide the stencil vectors, the energy shells and the quadrature weights defining Gauss-type quadratures up to order 5, in both $(3+1)$, $(2+1)$ and $(1+1)$ dimensions.

E.2.2 $(3+1)$ dimensions

Order 2		
$G = \{\bigcup n_i\}$	$\bar{p}^0_j$	w_{ij}
$(\pm2, \pm1, \pm1)_{\mathtt{FS}}$	3.3054072893322786	0.0245283950433191
$(\pm3, \quad 0, \quad 0)_{\mathtt{FS}}$	0.9358222275240878	0
	7.7587704831436335	0.0163006691342629
		0
		0.0003891858228425
		0.0017936666649682
Order 3		
$G = \{\bigcup n_i\}$	$\bar{p}^0_j$	w_{ij}
$(\pm4, \pm4, \pm3)_{\mathtt{FS}}$	0.7432919279814314	0
$(\pm5, \pm4, \quad 0)_{\mathtt{FS}}$	2.5716350076462784	0
$(\pm6, \pm2, \pm1)_{\mathtt{FS}}$	5.7311787516890996	0.0093098040253911
	10.953894312683190	0.0085195569675087
		0
		0.0056909667738262
		0.0013041770173120
		0
		0.0008932820065742
		0.0000029126213348

		0.0000338363537565
		0.0000090390475856
Order 4		
$G = \{\bigcup n_i\}$	$\bar{p}_j^0$	w_{ij}
$(\pm 6, \pm 6, \pm 3)_{\mathtt{FS}}$	0.6170308532782703	0.0035940787317887
$(\pm 7, \pm 4, \pm 4)_{\mathtt{FS}}$	2.1129659585785241	0
$(\pm 8, \pm 4, \pm 1)_{\mathtt{FS}}$	4.6108331510175324	0.0054532635512587
$(\pm 9, \pm 0, \pm 0)_{\mathtt{FS}}$	8.3990669712048421	0
	14.260103065920830	0.0051872438667849
		0
		0.0078705587777011
		0
		0.0023465096932558
		0
		0.0014234434124415
		0.0027124005098564
		0.0001406124343838
		0
		0.0000921239034238
		0.0001538745394240
		0.0000004165349753
		0.0000006474891627
		0.0000008063189502
		0.0000007889057767
Order 5		
$G = \{\bigcup n_i\}$	$\bar{p}_j^0$	w_{ij}
$(\pm 9, \pm 7, \pm 4)_{\mathtt{FS}}$	0.5276681217111288	0.0021976619314893
$(\pm 9, \pm 8, \pm 1)_{\mathtt{FS}}$	1.7962998096434089	0
$(\pm 11, \pm 4, \pm 3)_{\mathtt{FS}}$	3.8766415204769122	0.0035867160274663
$(\pm 11, \pm 5, \quad 0)_{\mathtt{FS}}$	6.9188165667047218	0
$(\pm 12, \pm 1, \pm 1)_{\mathtt{FS}}$	11.234610429083115	0
	17.645963552380712	0.0030360121467997
		0.0011645316435194
		0.0060892600232298
		0
		0
		0.0018738906904627

		0.0011933134012061
		0
		0
		0.0023241041809842
		0.0001734349866413
		0.0000829805751350
		0.0002171069160008
		0
		0.0000808225598283
		0.0000073565421488
		0.0000007284387015
		0
		0.0000125232075787
		0.0000031002793646
		0.0000000245062369
		0.0000000077527228
		0.0000000187275854
		0.0000000173590551
		0.0000000104611619

Table E.4: *Definition of quadratures up to the fifth order for a ultra-relativistic RLBM in (3+1) dimensions, following the parametrization for the discrete momentum vectors introduced in Eq. 2.24.*

E.2.2 $(2+1)$ *dimensions*

Order 2		
$G = \{\bigcup n_i\}$	$\bar{p}_j^0$	w_{ij}
$(\pm 3, \pm 4)_{\mathtt{FS}}$	0.4157745567834790	0
$(\pm 5, \quad 0)_{\mathtt{FS}}$	2.2942803602790417	0.0888866262411466
	6.2899450829374791	0
		0.0348147166961551
		0.0017535654166088
		0.0004218743543938
Order 3		
$G = \{\bigcup n_i\}$	$\bar{p}_j^0$	w_{ij}
$(\pm 3, \pm 4)_{\mathtt{FS}}$	0.3225476896193923	0
$(\pm 5, \quad 0)_{\mathtt{FS}}$	1.7457611011583465	0.0753942630427042

	4.5366202969211279	0.0410206173754781
	9.3950709123011331	0.0241670278669858
		0.0044457884155769
		0.0026380943565871
		0.0000616926157132
		0.0000365655303385

Order 4

$G = \{\bigcup n_i\}$	$\vec{p}_j^{\,0}$	w_{ij}
$(\pm 15, \pm 10)_{\mathtt{FS}}$	0.2635603197181409	0.0378774109856788
$(\pm 17, \pm 6)_{\mathtt{FS}}$	1.4134030591065167	0
$(\pm 18, \pm 1)_{\mathtt{FS}}$	3.5964257710407220	0.0273420403371722
	7.0858100058588375	0.0289416469003179
	12.640800844275782	0
		0.0208917044850790
		0.0055131239981112
		0
		0.0039796822121021
		0.0002621995147262
		0
		0.0001892703202640
		0.0000007577431574
		0.0000020654153959
		0.0000000980879948

Order 5

$G = \{\bigcup n_i\}$	$\vec{p}_j^{\,0}$	w_{ij}
$(\pm 15, \pm 10)_{\mathtt{FS}}$	0.2228466041792606	0.0333190352542491
$(\pm 17, \pm 6)_{\mathtt{FS}}$	1.1889321016726230	0
$(\pm 18, \pm 1)_{\mathtt{FS}}$	2.9927363260593140	0.0240515489894963
	5.7751435691045105	0.0302726248231082
	9.8374674183825899	0
	15.982873980601701	0.0218524790234068
		0.0032794546554440
		0.0108922181038115
		0
		0.0006330401002278
		0.0002681818675293
		0.0003986777138864

		0.0000146443834593
		0.0000094697718432
		0.0000085129950491
		0.0000000530695690
		0.0000000267552665
		0.0000000324936526

Table E.5: *Definition of quadratures up to the fifth order for a ultra-relativistic RLBM in (2+1) dimensions, following the parametrization for the discrete momentum vectors introduced in Eq. 2.24.*

E.2.2 $(1+1)$ *dimensions*

Order 2		
$G = \{\bigcup n_i\}$	$\bar{p}_j^0$	w_{ij}
(± 1)	3.414213562373095048	0.042893218813452475
	0.585786437626904951	1.457106781186547524
Order 3		
$G = \{\bigcup n_i\}$	$\bar{p}_j^0$	w_{ij}
(± 1)	6.289945082937479196	0.001651724516604877
	0.415774556783479083	1.710285053107483686
	2.294280360279041719	0.121396555709244769
Order 4		
$G = \{\bigcup n_i\}$	$\bar{p}_j^0$	w_{ij}
(± 1)	1.869968763544262523	0.322547689619392311
	0.008571999852268322	4.536620296921127983
	0.000057401877068880	9.395070912301133129
	0.204735168059733606	1.745761101158346575
Order 5		
$G = \{\bigcup n_i\}$	$\bar{p}_j^0$	w_{ij}
(± 1)	0.26356031971814091020	1.97964401902679930651
	3.59642577104072208122	0.02111608983931054815
	1.41340305910651679221	0.28206165857260368669
	7.08581000585883755692	0.00050971712153383997
	12.64080084427578265940	0.00000184877308595198

Table E.6: *Definition of quadratures up to the fifth order for a ultra-relativistic RLBM in (1+1) dimensions, following the parametrization for the discrete momentum vectors introduced in Eq. 2.24.*

Bibliography

[1] F. Jüttner, "Das Maxwellsche Gesetz der Geschwindigkeitsverteilung in der Relativtheorie," *Annalen der Physik*, vol. 339, no. 5, pp. 856–882, 1911.

[2] F. Jüttner, "Die relativistische Quantentheorie des idealen Gases," *Zeitschrift für Physik*, vol. 47, no. 7, pp. 542–566, 1928.

[3] A. Lichnerowicz and R. Marrot, "Propriétés statistiques des ensembles de particules en relativité restreinte," *CRAS*, vol. 210, pp. 759–761, 1940.

[4] W. Israel, "Relativistic kinetic theory of a simple gas," *Journal of Mathematical Physics*, vol. 4, no. 9, pp. 1163–1181, 1963.

[5] D. C. Kelly, *The kinetic theory of a relativistic gas.* 1963.

[6] J. M. Stewart, *Non-equilibrium relativistic kinetic theory.* Springer-Verlag Berlin, New York, 1971.

[7] S. R. De Groot, *Relativistic Kinetic Theory. Principles and Applications.* 1980.

[8] C. Cercignani and G. M. Kremer, *The Relativistic Boltzmann Equation: Theory and Applications.* Birkhäuser Basel, 2002.

[9] L. Rezzolla and O. Zanotti, *Relativistic Hydrodynamics.* Oxford University Press, 2013.

[10] P. Romatschke and U. Romatschke, "Relativistic Fluid Dynamics In and Out of Equilibrium – Ten Years of Progress in Theory and Numerical Simulations of Nuclear Collisions," 2017.

[11] L. Horwitz, S. Shashoua, and W. Schieve, "A manifestly covariant relativistic Boltzmann equation for the evolution of a system of events," *Physica A: Statistical Mechanics and its Applications*, vol. 161, no. 2, pp. 300 – 338, 1989.

[12] W. C. Schieve, "Covariant relativistic statistical mechanics of many particles," *Foundations of Physics*, vol. 35, no. 8, pp. 1359–1381, 2005.

[13] E. Lehmann, "Covariant equilibrium statistical mechanics," *Journal of Mathematical Physics*, vol. 47, no. 2, p. 023303, 2006.

[14] J. Dunkel, P. Talkner, and P. Hänggi, "Relative entropy, Haar measures and relativistic canonical velocity distributions," *New Journal of Physics*, vol. 9, no. 5, p. 144, 2007.

[15] D. Cubero, J. Casado-Pascual, J. Dunkel, P. Talkner, and P. Hänggi, "Thermal Equilibrium and Statistical Thermometers in Special Relativity," *Phys. Rev. Lett.*, vol. 99, p. 170601, 2007.

[16] A. Montakhab, M. Ghodrat, and M. Barati, "Statistical thermodynamics of a two-dimensional relativistic gas," *Phys. Rev. E*, vol. 79, p. 031124, 2009.

[17] F. Peano, M. Marti, L. O. Silva, and G. Coppa, "Statistical kinetic treatment of relativistic binary collisions," *Phys. Rev. E*, vol. 79, p. 025701, 2009.

[18] C. Eckart, "The Thermodynamics of Irreversible Processes. III. Relativistic Theory of the Simple Fluid," *Phys. Rev.*, vol. 58, pp. 919–924, 1940.

[19] L. Landau and E. Lifshitz, *Fluid Mechanics*. Elsevier Science, 1987.

[20] I.-S. Liu, I. Müller, and T. Ruggeri, "Relativistic thermodynamics of gases," *Annals of Physics*, vol. 169, no. 1, pp. 191 – 219, 1986.

[21] W. Israel and J. Stewart, "Thermodynamics of nonstationary and transient effects in a relativistic gas," *Physics Letters A*, vol. 58, no. 4, pp. 213 – 215, 1976.

[22] W. Israel, "Nonstationary irreversible thermodynamics: A Causal relativistic theory," *Annals Phys.*, vol. 100, pp. 310–331, 1976.

[23] W. Israel and J. M. Stewart, "On Transient Relativistic Thermodynamics and Kinetic Theory. II," *Proceedings of the Royal Society of London A: Mathematical, Physical and Engineering Sciences*, vol. 365, no. 1720, pp. 43–52, 1979.

[24] G. S. Denicol, H. Niemi, E. Molnár, and D. H. Rischke, "Derivation of transient relativistic fluid dynamics from the boltzmann equation," *Phys. Rev. D*, vol. 85, p. 114047, 2012.

[25] P. Huovinen and D. Molnar, "Applicability of causal dissipative hydrodynamics to relativistic heavy ion collisions," *Phys. Rev. C*, vol. 79, p. 014906, 2009.

[26] I. Bouras, E. Molnár, H. Niemi, Z. Xu, A. El, O. Fochler, C. Greiner, and D. H. Rischke, "Investigation of shock waves in the relativistic riemann problem: A comparison of viscous fluid dynamics to kinetic theory," *Phys. Rev. C*, vol. 82, p. 024910, 2010.

[27] P. L. Bhatnagar, E. P. Gross, and M. Krook, "A model for collision processes in gases. amplitude processes in charged and neutral one-component systems," *Phys. Rev.*, vol. 94, no. 3, pp. 511–525, 1954.

[28] C. Marle, "Sur l'établissement des équations de l'hydrodynamique des fluides relativistes dissipatifs. I. — L'équation de Boltzmann relativiste," *Annales de l'I.H.P. Physique théorique*, vol. 10, no. 1, pp. 67–126, 1969.

[29] C. Marle, "Sur l'établissement des équations de l'hydrodynamique des fluides relativistes dissipatifs. II. — Méthodes de résolution approchée de l'équation de Boltzmann relativiste," *Annales de l'I.H.P. Physique théorique*, vol. 10, no. 2, pp. 127–194, 1969.

[30] M. Takamoto and S. ichiro Inutsuka, "The relativistic kinetic dispersion relation: Comparison of the relativistic Bhatnagar–Gross–Krook model and Grad's 14-moment expansion ," *Physica A: Statistical Mechanics and its Applications*, vol. 389, no. 21, pp. 4580 – 4603, 2010.

[31] J. Anderson and H. Witting, "A relativistic relaxation-time model for the Boltzmann equation," *Physica*, vol. 74, no. 3, pp. 466 – 488, 1974.

[32] J. Anderson and H. Witting, "Relativistic quantum transport coefficients," *Physica*, vol. 74, no. 3, pp. 489 – 495, 1974.

[33] H. Grad, "On the kinetic theory of rarefied gases," *Communications on Pure and Applied Mathematics*, vol. 2, no. 4, pp. 331–407, 1949.

[34] S. Chapman and T. G. Cowling, *The Mathematical Theory of Non-Uniform Gases, 3rd ed.* Cambridge University Press, 1970.

[35] R. M. Velasco, F. J. Uribe, and L. S. García-Colín, "Inconsistencies in moment methods," *Phys. Rev. E*, vol. 66, p. 032103, 2002.

[36] H. Struchtrup and M. Torrilhon, "Regularization of Grad's 13 moment equations: Derivation and linear analysis," *Physics of Fluids*, vol. 15, no. 9, pp. 2668–2680, 2003.

[37] H. C. Öttinger, "Thermodynamically Admissible 13 Moment Equations from the Boltzmann Equation," *Phys. Rev. Lett.*, vol. 104, p. 120601, 2010.

[38] M. Torrilhon, "Modeling Nonequilibrium Gas Flow Based on Moment Equations," *Annual review of fluid mechanics*, vol. 48, no. 1, pp. 429–458, 2016.

[39] K. Tsumura and T. Kunihiro, "Derivation of relativistic hydrodynamic equations consistent with relativistic Boltzmann equation by renormalization-group method," *The European Physical Journal A*, vol. 48, no. 11, p. 162, 2012.

[40] G. S. Denicol, T. Koide, and D. H. Rischke, "Dissipative relativistic fluid dynamics: A new way to derive the equations of motion from kinetic theory," *Phys. Rev. Lett.*, vol. 105, p. 162501, 2010.

[41] E. Molnár, H. Niemi, G. S. Denicol, and D. H. Rischke, "Relative importance of second-order terms in relativistic dissipative fluid dynamics," *Phys. Rev. D*, vol. 89, p. 074010, 2014.

[42] A. Jaiswal, R. S. Bhalerao, and S. Pal, "Complete relativistic second-order dissipative hydrodynamics from the entropy principle," *Phys. Rev. C*, vol. 87, p. 021901, 2013.

[43] K. Tsumura, Y. Kikuchi, and T. Kunihiro, "Relativistic causal hydrodynamics derived from Boltzmann equation: A novel reduction theoretical approach," *Phys. Rev. D*, vol. 92, p. 085048, 2015.

[44] Y. Kikuchi, K. Tsumura, and T. Kunihiro, "Derivation of second-order relativistic hydrodynamics for reactive multicomponent systems," *Phys. Rev. C*, vol. 92, p. 064909, 2015.

[45] Y. Kikuchi, K. Tsumura, and T. Kunihiro, "Mesoscopic dynamics of fermionic cold atoms — quantitative analysis of transport coefficients and relaxation times," *Physics Letters A*, vol. 380, no. 24, pp. 2075 – 2080, 2016.

[46] S. Plumari, A. Puglisi, F. Scardina, and V. Greco, "Shear viscosity of a strongly interacting system: Green-Kubo correlator versus Chapman-Enskog and relaxation-time approximations," *Phys. Rev. C*, vol. 86, p. 054902, 2012.

[47] W. Florkowski, R. Ryblewski, and M. Strickland, "Testing viscous and anisotropic hydrodynamics in an exactly solvable case," *Phys. Rev. C*, vol. 88, p. 024903, 2013.

[48] R. S. Bhalerao, A. Jaiswal, S. Pal, and V. Sreekanth, "Relativistic viscous hydrodynamics for heavy-ion collisions: A comparison between the Chapman-Enskog and Grad methods," *Phys. Rev. C*, vol. 89, p. 054903, 2014.

[49] F. Karsch and D. E. Miller, "Exact equation of state for ideal relativistic quantum gases," *Phys. Rev. A*, vol. 22, pp. 1210–1219, 1980.

[50] S. Succi, *The Lattice Boltzmann Equation: For Complex States of Flowing Matter*. OUP Oxford, 2018.

[51] M. Mendoza, B. M. Boghosian, H. J. Herrmann, and S. Succi, "Fast Lattice Boltzmann Solver for Relativistic Hydrodynamics," *Phys. Rev. Lett.*, vol. 105, p. 014502, 2010.

[52] M. Mendoza, B. M. Boghosian, H. J. Herrmann, and S. Succi, "Derivation of the lattice Boltzmann model for relativistic hydrodynamics," *Phys. Rev. D*, vol. 82, p. 105008, 2010.

[53] P. Romatschke, M. Mendoza, and S. Succi, "Fully relativistic lattice Boltzmann algorithm," *Phys. Rev. C*, vol. 84, p. 034903, 2011.

[54] Q. Li, K. H. Luo, and X. J. Li, "Lattice Boltzmann method for relativistic hydrodynamics: Issues on conservation law of particle number and discontinuities," *Phys. Rev.*, vol. D86, p. 085044, 2012.

[55] F. Mohseni, M. Mendoza, S. Succi, and H. J. Herrmann, "Lattice Boltzmann model for ultrarelativistic flows," *Phys. Rev. D*, vol. 87, p. 083003, 2013.

[56] M. Mendoza, I. Karlin, S. Succi, and H. J. Herrmann, "Relativistic lattice Boltzmann model with improved dissipation," *Phys. Rev. D*, vol. 87, p. 065027, 2013.

[57] R. Blaga and V. E. Ambruş, "Quadrature-based lattice Boltzmann model for relativistic flows," *AIP Conference Proceedings*, vol. 1796, no. 1, p. 020010, 2017.

[58] V. E. Ambrus and R. Blaga, "High-order quadrature-based lattice Boltzmann models for the flow of ultrarelativistic rarefied gases," 2016.

[59] D. Oettinger, M. Mendoza, and H. J. Herrmann, "Gaussian quadrature and lattice discretization of the Fermi-Dirac distribution for graphene," *Phys. Rev. E*, vol. 88, p. 013302, 2013.

[60] O. Furtmaier, M. Mendoza, I. Karlin, S. Succi, and H. J. Herrmann, "Rayleigh-Bénard instability in graphene," *Phys. Rev. B*, vol. 91, p. 085401, 2015.

[61] R. C. V. Coelho, M. Mendoza, M. M. Doria, and H. J. Herrmann, "Kelvin-Helmholtz instability of the Dirac fluid of charge carriers on graphene," *Phys. Rev. B*, vol. 96, p. 184307, 2017.

[62] R. C. Coelho, M. Mendoza, M. M. Doria, and H. J. Herrmann, "Fully dissipative relativistic lattice Boltzmann method in two dimensions," *Computers & Fluids*, vol. 172, pp. 318 – 331, 2018.

[63] A. Gabbana, M. Mendoza, S. Succi, and R. Tripiccione, "Numerical evidence of electron hydrodynamic whirlpools in graphene samples," *Computers & Fluids*, vol. 172, pp. 644 – 650, 2018.

[64] A. Gabbana, M. Mendoza, S. Succi, and R. Tripiccione, "Towards a unified lattice kinetic scheme for relativistic hydrodynamics," *Phys. Rev. E*, vol. 95, p. 053304, 2017.

[65] A. Gabbana, M. Mendoza, S. Succi, and R. Tripiccione, "Kinetic approach to relativistic dissipation," *Phys. Rev. E*, vol. 96, p. 023305, 2017.

[66] G. R. McNamara and G. Zanetti, "Use of the Boltzmann Equation to Simulate Lattice-Gas Automata," *Phys. Rev. Lett.*, vol. 61, pp. 2332–2335, 1988.

[67] U. Frisch, B. Hasslacher, and Y. Pomeau, "Lattice-Gas Automata for the Navier-Stokes Equation," *Phys. Rev. Lett.*, vol. 56, pp. 1505–1508, 1986.

[68] S. Wolfram, "Cellular automaton fluids 1: Basic theory," *Journal of Statistical Physics*, vol. 45, no. 3, pp. 471–526, 1986.

[69] F. J. Higuera and J. Jiménez, "Boltzmann approach to lattice gas simulations," *EPL (Europhysics Letters)*, vol. 9, p. 663, 1989.

[70] F. J. Higuera, S. Succi, and R. Benzi, "Lattice gas dynamics with enhanced collisions," *EPL (Europhysics Letters)*, vol. 9, no. 4, p. 345, 1989.

[71] H. Chen, S. Chen, and W. H. Matthaeus, "Recovery of the Navier-Stokes equations using a lattice-gas Boltzmann method," *Phys. Rev. A*, vol. 45, pp. R5339–R5342, 1992.

[72] R. Benzi, S. Succi, and M. Vergassola, "The lattice boltzmann equation: theory and applications," *Physics Reports*, vol. 222, no. 3, pp. 145 – 197, 1992.

[73] X. He and L.-S. Luo, "Theory of the lattice Boltzmann method: From the Boltzmann equation to the lattice Boltzmann equation," *Phys. Rev. E*, vol. 56, pp. 6811–6817, 1997.

[74] X. Shan and X. He, "Discretization of the Velocity Space in the Solution of the Boltzmann Equation," *Phys. Rev. Lett.*, vol. 80, pp. 65–68, 1998.

[75] N. S. Martys, X. Shan, and H. Chen, "Evaluation of the external force term in the discrete Boltzmann equation," *Phys. Rev. E*, vol. 58, pp. 6855–6857, 1998.

[76] X. Shan, "Kinetic theory representation of hydrodynamics: a way beyond the Navier–Stokes equation," *Journal of Fluid Mechanics*, vol. 550, no. -1, pp. 413–441, 2006.

[77] H. Grad, "Note on N-dimensional Hermite polynomials," *Communications on Pure and Applied Mathematics*, vol. 2, no. 4, pp. 325–330, 1949.

[78] P. C. Philippi, L. A. Hegele, L. O. E. dos Santos, and R. Surmas, "From the continuous to the lattice Boltzmann equation: The discretization problem and thermal models," *Phys. Rev. E*, vol. 73, p. 056702, 2006.

[79] X. Shan, "General solution of lattices for Cartesian lattice Bhatanagar-Gross-Krook models," *Phys. Rev. E*, vol. 81, p. 036702, 2010.

[80] X. Shan, "The mathematical structure of the lattices of the lattice Boltzmann method," *Journal of Computational Science*, vol. 17, pp. 475–481, 2016.

[81] "See supplemental material at www.fe.infn.it/u/agabbana/thesis-som."

[82] A. Jaiswal, "Relativistic dissipative hydrodynamics from kinetic theory with relaxation-time approximation," *Phys. Rev. C*, vol. 87, p. 051901, 2013.

[83] A. Jaiswal, "Relativistic third-order dissipative fluid dynamics from kinetic theory," *Phys. Rev. C*, vol. 88, p. 021903, 2013.

[84] G. I. Taylor and A. E. Green, "Mechanism of the Production of Small Eddies from Large Ones," *Proceedings of the Royal Society of London A: Mathematical, Physical and Engineering Sciences*, vol. 158, no. 895, pp. 499–521, 1937.

[85] C. Chattopadhyay, A. Jaiswal, S. Pal, and R. Ryblewski, "Relativistic third-order viscous corrections to the entropy four-current from kinetic theory," *Phys. Rev. C*, vol. 91, p. 024917, 2015.

[86] M. Tuval and A. Yahalom, "Newton's third law in the framework of special relativity," *The European Physical Journal Plus*, vol. 129, no. 11, p. 240, 2014.

[87] F. Lora-Clavijo, J. Cruz-Pérez, F. Siddhartha Guzmán, and J. González, "Exact solution of the 1D Riemann problem in Newtonian and relativistic hydrodynamics," *Revista mexicana de física E*, vol. 59, no. 1, pp. 28–50, 2013.

[88] Z. Xu and C. Greiner, "Transport rates and momentum isotropization of gluon matter in ultrarelativistic heavy-ion collisions," *Phys. Rev. C*, vol. 76, p. 024911, 2007.

[89] I. Bouras, E. Molnár, H. Niemi, Z. Xu, A. El, O. Fochler, C. Greiner, and D. H. Rischke, "Relativistic shock waves in viscous gluon matter," *Phys. Rev. Lett.*, vol. 103, p. 032301, 2009.

[90] A. El, A. Muronga, Z. Xu, and C. Greiner, "Shear viscosity and out of equilibrium dynamics," *Phys. Rev. C*, vol. 79, p. 044914, 2009.

[91] J. Crossno, J. K. Shi, K. Wang, X. Liu, A. Harzheim, A. Lucas, S. Sachdev, P. Kim, T. Taniguchi, K. Watanabe, T. A. Ohki, and K. C. Fong, "Observation of the dirac fluid and the breakdown of the wiedemann-franz law in graphene," *Science*, vol. 351, no. 6277, pp. 1058–1061, 2016.

[92] M. Müller, L. Fritz, and S. Sachdev, "Quantum-critical relativistic magnetotransport in graphene," *Phys. Rev. B*, vol. 78, p. 115406, 2008.

[93] M. Müller, J. Schmalian, and L. Fritz, "Graphene: A nearly perfect fluid," *Phys. Rev. Lett.*, vol. 103, p. 025301, 2009.

[94] D. A. Bandurin, I. Torre, R. K. Kumar, M. Ben Shalom, A. Tomadin, A. Principi, G. H. Auton, E. Khestanova, K. S. Novoselov, I. V. Grigorieva, L. A. Ponomarenko, A. K. Geim, and M. Polini, "Negative local resistance caused by viscous electron backflow in graphene," *Science*, vol. 351, no. 6277, pp. 1055–1058, 2016.

[95] R. Krishna Kumar, D. A. Bandurin, F. M. Pellegrino, Y. Cao, A. Principi, H. Guo, G. H. Auton, M. Ben Shalom, L. A. Ponomarenko, G. Falkovich, K. Watanabe, T. Taniguchi, I. V. Grigorieva, L. S. Levitov, M. Polini, and A. K. Geim, "Superballistic flow of viscous electron fluid through graphene constrictions," *Nature Physics*, vol. 13, no. 12, pp. 1182–1185, 2017.

[96] R. N. Gurzhi, "Minimum of resistance in impurity-free conductors," *Journal of Experimental and Theoretical Physics*, vol. 17, no. 512, p. 053001, 1963.

[97] B. A. Braem, F. M. Pellegrino, A. Principi, M. Röösli, S. Hennel, J. V. Koski, M. Berl, W. Dietsche, W. Wegscheider, M. Polini, T. Ihn, and K. Ensslin, "Scanning Gate Microscopy in a Viscous Electron Fluid," *ArXiv e-prints*, 2018.

[98] D. A. Bandurin, A. V. Shytov, L. S. Levitov, R. K. Kumar, A. I. Berdyugin, M. Ben Shalom, I. V. Grigorieva, A. K. Geim, and

G. Falkovich, "Fluidity onset in graphene," *Nature Communications*, vol. 9, p. 4533, 2018.

[99] A. I. Berdyugin, S. G. Xu, F. M. D. Pellegrino, R. Krishna Kumar, A. Principi, I. Torre, M. Ben Shalom, T. Taniguchi, K. Watanabe, I. V. Grigorieva, M. Polini, A. K. Geim, and D. A. Bandurin, "Measuring Hall Viscosity of Graphene's Electron Fluid," *ArXiv e-prints*, 2018.

[100] P. J. W. Moll, P. Kushwaha, N. Nandi, B. Schmidt, and A. P. Mackenzie, "Evidence for hydrodynamic electron flow in PdCoO2," *Science*, vol. 351, no. 6277, pp. 1061–1064, 2016.

[101] J. Gooth, F. Menges, C. Shekhar, V. Süß, N. Kumar, Y. Sun, U. Drechsler, R. Zierold, C. Felser, and B. Gotsmann, "Electrical and Thermal Transport at the Planckian Bound of Dissipation in the Hydrodynamic Electron Fluid of WP2," 2017.

[102] P. R. Wallace, "The band theory of graphite," *Phys. Rev.*, vol. 71, no. 9, pp. 622–634, 1947.

[103] G. Policastro, D. T. Son, and A. O. Starinets, "Shear viscosity of strongly coupled $n = 4$ supersymmetric yang-mills plasma," *Phys. Rev. Lett.*, vol. 87, p. 081601, 2001.

[104] P. K. Kovtun, D. T. Son, and A. O. Starinets, "Viscosity in strongly interacting quantum field theories from black hole physics," *Phys. Rev. Lett.*, vol. 94, p. 111601, 2005.

[105] M. Mendoza, H. J. Herrmann, and S. Succi, "Preturbulent Regimes in Graphene Flow," *Phys. Rev. Lett.*, vol. 106, no. 15, p. 156601, 2011.

[106] A. Lucas and K. C. Fong, "Hydrodynamics of electrons in graphene," *Journal of Physics: Condensed Matter*, vol. 30, no. 5, p. 053001, 2018.

[107] S. V. Morozov, K. S. Novoselov, M. I. Katsnelson, F. Schedin, D. C. Elias, J. A. Jaszczak, and A. K. Geim, "Giant intrinsic carrier mobilities in graphene and its bilayer," *Phys. Rev. Lett.*, vol. 100, p. 016602, 2008.

[108] L. Wang, I. Meric, P. Y. Huang, Q. Gao, Y. Gao, H. Tran, T. Taniguchi, K. Watanabe, L. M. Campos, D. A. Muller, J. Guo, P. Kim, J. Hone, K. L. Shepard, and C. R. Dean, "One-dimensional electrical contact to a two-dimensional material," *Science*, vol. 342, no. 6158, pp. 614–617, 2013.

[109] I. Torre, A. Tomadin, A. K. Geim, and M. Polini, "Nonlocal transport and the hydrodynamic shear viscosity in graphene," *Phys. Rev. B*, vol. 92, p. 165433, 2015.

[110] F. M. D. Pellegrino, I. Torre, A. K. Geim, and M. Polini, "Electron hydrodynamics dilemma: Whirlpools or no whirlpools," *Phys. Rev. B*, vol. 94, p. 155414, 2016.

[111] A. Gabbana, M. Polini, S. Succi, R. Tripiccione, and F. M. D. Pellegrino, "Prospects for the detection of electronic preturbulence in graphene," *Phys. Rev. Lett.*, vol. 121, p. 236602, 2018.

[112] A. Tomadin and M. Polini, "Theory of the plasma-wave photoresponse of a gated graphene sheet," *Phys. Rev. B*, vol. 88, p. 205426, 2013.

[113] G. Giuliani and G. Vignale, "Quantum theory of the electron liquid," *Contemporary Physics*, vol. 51, no. 3, pp. 284–285, 2010.

[114] A. Lucas, J. Crossno, K. C. Fong, P. Kim, and S. Sachdev, "Transport in inhomogeneous quantum critical fluids and in the Dirac fluid in graphene," *Phys. Rev. B*, vol. 93, p. 075426, 2016.

[115] M. Sbragaglia, R. Benzi, L. Biferale, H. Chen, X. Shan, and S. Succi, "Lattice Boltzmann method with self-consistent thermo-hydrodynamic equilibria," *Journal of Fluid Mechanics*, vol. 628, p. 299, jun 2009.

[116] A. Scagliarini, L. Biferale, M. Sbragaglia, K. Sugiyama, and F. Toschi, "Lattice Boltzmann methods for thermal flows: Continuum limit and applications to compressible Rayleigh-Taylor systems," *Physics of Fluids*, vol. 22, no. 5, pp. 1–21, 2010.

[117] J. Tölke and M. Krafczyk, "TeraFLOP computing on a desktop PC with GPUs for 3D CFD," *International Journal of Computational Fluid Dynamics*, vol. 22, no. 7, pp. 443–456, 2008.

[118] F. Belletti, L. Biferale, F. Mantovani, S. F. Schifano, F. Toschi, and R. Tripiccione, "Multiphase lattice Boltzmann on the Cell Broadband Engine," *Nuovo Cimento C Geophysics Space Physics C*, vol. 32, no. 2, pp. 53–56, 2009.

[119] "Lattice Boltzmann fluid-dynamics on the QPACE supercomputer," *Procedia Computer Science*, vol. 1, no. 1, pp. 1075 – 1082, 2010.

[120] G. Crimi, F. Mantovani, M. Pivanti, S. Schifano, and R. Tripiccione, "Early Experience on Porting and Running a Lattice Boltzmann Code on the Xeon-phi Co-Processor," *Procedia Computer Science*, vol. 18, pp. 551 – 560, 2013.

[121] "Massively parallel lattice-Boltzmann codes on large GPU clusters," *Parallel Computing*, vol. 58, pp. 1–24, 2016.

[122] E. Calore, A. Gabbana, S. F. Schifano, and R. Tripiccione, *Early experience on using knights landing processors for lattice Boltzmann applications*, vol. Lecture Notes in Computer Science, 10777. 2018.

[123] E. Calore, S. F. Schifano, and R. Tripiccione, "A Portable OpenCL Lattice Boltzmann Code for Multi- and Many-core Processor Architectures," *Procedia Computer Science*, vol. 29, pp. 40 – 49, 2014.

[124] E. Calore, A. Gabbana, J. Kraus, S. F. Schifano, and R. Tripiccione, "Performance and portability of accelerated lattice Boltzmann applications with OpenACC," *Concurrency and Computation: Practice and Experience*, vol. 28, pp. 3485–3502, aug 2016.

[125] E. Calore, A. Gabbana, S. F. Schifano, and R. Tripiccione, "Evaluation of DVFS techniques on modern HPC processors and accelerators for energy-aware applications," *Concurrency and Computation: Practice and Experience*, no. November 2016, p. e4143, 2017.

[126] E. Calore, A. Gabbana, S. Schifano, and R. Tripiccione, "Software and DVFS Tuning for Performance and Energy-Efficiency on Intel KNL Processors," *Journal of Low Power Electronics and Applications*, vol. 8, no. 2, p. 18, 2018.

[127] E. Calore, A. Gabbana, S. F. Schifano, and R. Tripiccione, "Energy-Efficiency Evaluation of Intel KNL for HPC Workloads," *Advances in Parallel Computing*, vol. 32, pp. 733–742, 2018.

[128] L. Biferale, F. Mantovani, M. Sbragaglia, A. Scagliarini, F. Toschi, and R. Tripiccione, "High resolution numerical study of Rayleigh–Taylor turbulence using a thermal lattice Boltzmann scheme," *Physics of Fluids*, vol. 22, no. 11, p. 115112, 2010.

[129] L. Biferale, F. Mantovani, M. Sbragaglia, A. Scagliarini, F. Toschi, and R. Tripiccione, "Second-order closure in stratified turbulence: Simulations and modeling of bulk and entrainment regions," *Phys. Rev. E*, vol. 84, p. 016305, Jul 2011.

[130] L. Biferale, F. Mantovani, M. Sbragaglia, A. Scagliarini, F. Toschi, and R. Tripiccione, "Reactive Rayleigh-Taylor systems: Front propagation and non-stationarity," *EPL (Europhysics Letters)*, vol. 94, no. 5, p. 54004, 2011.

[131] A. Scagliarini, L. Biferale, F. Mantovani, M. Pivanti, F. Pozzati, M. Sbragaglia, S. F. Schifano, F. Toschi, and R. Tripiccione, "Front propagation in Rayleigh-Taylor systems with reaction," *Journal of Physics: Conference Series*, vol. 318, no. 9, p. 092024, 2011.

[132] V. D. Poor, "The concept of attached processing and attached resource computer systems," *SIGMINI Newsl.*, vol. 4, no. 2, pp. 7–7, 1978.

[133] R. W. Hockney and C. R. Jesshope, *Parallel Computers Two: Architecture, Programming and Algorithms*. Bristol, UK, UK: IOP Publishing Ltd., 2nd ed., 1988.

[134] R. N. Ibbett and N. P. Topham, *Architecture of High Performance Computers Volume II, Array processors and multiprocessor systems*. New York, NY: Springer., 1st ed., 1989.

[135] "The Top 500 List ," Nov 2018. www.top500.org.

[136] "The Green 500 List ," Nov 2018. www.green500.org.

[137] C. Bonati, E. Calore, S. Coscetti, M. D'Elia, M. Mesiti, F. Negro, S. F. Schifano, and R. Tripiccione, "Development of scientific software for HPC architectures using OpenACC: the case of LQCD," in *The 2015 International Workshop on Software Engineering for High Performance Computing in Science (SE4HPCS)*, ICSE Companion Proceedings, pp. 9–15, 2015.

[138] S. Wienke, C. Terboven, J. C. Beyer, and M. S. Müller, "A Pattern-Based Comparison of OpenACC and OpenMP for Accelerator Computing," in *Euro-Par 2014 Parallel Processing: 20th International Conference, Porto, Portugal, August 25-29, 2014. Proceedings* (F. Silva, I. Dutra, and V. Santos Costa, eds.), Lecture Notes in Computer Science, pp. 812–823, Springer, 2014.

[139] K. Mattila, J. Hyväluoma, T. Rossi, M. Aspnäs, and J. Westerholm, "An efficient swap algorithm for the lattice Boltzmann method," *Computer Physics Communications*, vol. 176, no. 3, pp. 200 – 210, 2007.

[140] P. Bailey, J. Myre, S. D. C. Walsh, D. J. Lilja, and M. O. Saar, "Accelerating Lattice Boltzmann Fluid Flow Simulations Using Graphics Processors," *2009 International Conference on Parallel Processing*, pp. 550–557, 2009.

[141] M. Schönherr, M. Geier, and M. Krafczyk, "3D GPGPU LBM implementation on non-uniform grids," in *International Conference on Parallel Computational Fluid Dynamics*, 2011.

[142] M. Wittmann, T. Zeiser, G. Hager, and G. Wellein, "Comparison of different propagation steps for the Lattice Boltzmann Method," *CoRR*, vol. abs/1111.0922, 2011.

[143] A. G. Shet, S. H. Sorathiya, S. Krithivasan, A. M. Deshpande, B. Kaul, S. D. Sherlekar, and S. Ansumali, "Data structure and movement for lattice-based simulations," *Phys. Rev. E*, vol. 88, p. 013314, Jul 2013.

[144] E. Calore, A. Gabbana, S. Schifano, and R. Tripiccione, "Optimization of lattice Boltzmann simulations on heterogeneous computers," *The International Journal of High Performance Computing Applications*, p. 109434201770377, 2017.

[145] E. F. Taylor, J. A. Wheeler, and J. M. Bowen, "Spacetime physics: Introduction to special relativity, 2nd ed.," *American Journal of Physics*, vol. 61, no. 3, pp. 284–284, 1993.

[146] A. Einstein, "Zur Elektrodynamik bewegter Körper," *Annalen der Physik*, vol. 17, no. 10, pp. 891–921, 1905.

[147] E. Grosswald, *Bessel Polynomials (Lecture Notes in Mathematics)*. Springer, 1979.